8-2022

Quantum Transport and Electric-Field Effects in Layered Topological Semimetals and Magnetic Materials

Arash Fereidouni Ghaleh Minab
University of Arkansas, Fayetteville

Quantum Transport and Electric-Field Effects in Layered Topological Semimetals and Magnetic Materials

A dissertation submitted in partial fulfillment
of the requirements for the degree of
Doctor of Philosophy in Physics

by

Arash Fereidouni Ghaleh Minab
Shiraz University
Bachelor of Science in Physics, 2014
University of Minnesota
Master of Science in Physics, 2016

August 2022
University of Arkansas

This dissertation is approved for recommendation to the Graduate Council.

Hugh O. H. Churchill, Ph.D.
Dissertation Director

Jin Hu, Ph.D.
Committee Member

Salvador Barraza-Lopez, Ph.D.
Committee Member

Abstract

This dissertation describes transport experiments on quantum devices in layered Dirac nodal line topological semimetals and antiferromagnetic materials down to a few layers. We used gate-induced effects to alter the transport properties of these materials.

First, we introduced current annealing in topological semimetals to achieve high-quality devices. We demonstrate current annealing to substantially improve the electronic transport properties of 2D topological semimetal flakes. Contact resistance and resistivity were improved by factors up to 2×10^6 and 2×10^4, respectively, in devices based on exfoliated flakes of two topological semimetals, ZrSiSe and $BaMnSb_2$. Using this method, carrier mobility in ZrSiSe improved by a factor of 3800, resulting in the observation of record-high mobility for exfoliated ZrSiSe. Quantum oscillations in annealed ZrSiSe appeared at magnetic fields as low as 5 T, and magnetoresistance increased by 10^4. We argue that a thermal process underlies this improvement. Finally, Raman spectroscopy and analysis of quantum oscillations in ZrSiSe indicate that the phonon modes and Fermi surface area are unchanged by current annealing.

Through current annealing, we had access to suitable device quality, hence could investigate topological semimetals extensively. We studied Shubnikov de Haas oscillations focused on the unexpected frequency of 140 T that is unrelated to any known surface (450 T) or bulk (220 T) Fermi surface. We show that this frequency has a 2D nature by providing angle dependence and thickness dependence of quantum oscillations. Angle dependence of 140 T follows $\cos^{-1}(\theta)$, in contrast to bulk frequency, 220 T, which shows no change with angle. In addition, thickness dependence shows that the relative amplitude of 140 T to 220 T exponentially increases by decreasing the thickness. In addition, we provide a comparison of phase analysis of 140 T with 220 T that shows the different origins of these frequencies. We speculate this 140 T frequency can be of Weyl orbit oscillations and extracted a Fermi arc with a length of 0.08 $\mathring{A}^{-1}$ within this picture.

Third, we studied the gate-induced electrostatic field effect on ZrSiSe using ZrSiSe/hBN/-graphene heterostructure. We observed that the electrostatic field increases the resistivity away from charge neutrality point $V_g = 0.8\ V$ at magnetic fields below 2 T. In contrast, the electrostatic field reduces resistivity at fields above 2 T. In addition, we observed that gate voltage reduces the curvature of magnetoresistance. In addition, the amplitude of quantum oscillations reduces with an increase in gate voltage. The bulk frequency of quantum oscillations, 220 T, does not change with gate voltage, but the Weyl orbit frequency, 140 T, shows a quadratic red shift with the gate voltage.

In addition to topological semimetals in few-layer limits that excited many physicists in the last decade, the interplay of magnetism and superconductivity as well as electrostatic field control of magnetic phase in 2D limit enchanted many physicists, including us. The interplay between magnetic materials and superconductors provides an exciting playground due to opposing requirements for electron spin alignment between superconductivity and magnetic order.

In the fourth chapter, we studied $NiPS_3$, an antiferromagnetic layered material with in-plane antiferromagnetic order, and FeSe, a layered superconductor, by fabricating superconductor/antiferromagnet/superconductor (FeSe/$NiPS_3$/FeSe) Josephson Junction. In addition, we fabricated a controlled Josephson Junction using graphite and a similar thickness of $NiPS_3$, graphite/$NiPS_3$/graphite, to have a fair comparison with the superconductor Josephson Junction. We showed that our devices were in a direct tunneling regime at temperatures lower than 20 K and 10 K for graphite-JJ and FeSe-JJ, respectively. It has been shown that $NiPS_3$ undergoes a spin-flop transition in magnetic fields parallel to the ab plane and larger than 6 T. Although we failed to observe this spin-flop transition for fields parallel to the ab plane, we observed signatures of possible transition in magnetic fields parallel to the c axis for the similar magnetic field in our controlled graphite device. However, this observation is ambiguous because such a spin-flop transition was not observed in bulk measurements.

Further, we observed steps in the temperature dependence of resistivity for FeSe-JJ; these steps do not exist in a graphite-JJ control device; hence we attribute them to FeSe-JJ. The steps in the temperature dependence of resistivity happen at 50 K and 10 K; this coincides with the transition temperature of FeSe to a superconductor. In addition, we observed anisotropic and unconventional magnetoresistance in temperatures between 50 K and 10 K. This anisotropic magnetoresistance dies at temperatures lower than 10 K when FeSe becomes superconducting.

Finally, in the fifth chapter, we attempted to induce a magnetic phase transition in $MnPSe_3$, $FePS_3$, and VPS_3 by adjusting the carrier density in these materials using an electrostatic field. Due to the spin filtering effect, such magnetic phase transition should accompany higher conductivity or even semimetallic behavior, but our devices failed to show such behavior. We fabricated devices using various contact metals, geometry, and gating techniques but achieving the long-sought after magnetic phase transition remained elusive in these materials. However, we successfully doped these materials using electrostatic field-induced effects.

Acknowledgements

I acknowledge the support and help of my colleagues at Churchill's quantum devices lab and Hu's quantum materials lab. Special thanks to Dr. Mahmudul Hasan Doha, Dr. Joshua Thompson, and Jeb stacy. We acknowledge our collaborators Dr. Jin Hu for material growth and technical consultation, Dr. Salvador Barraza-Lopez for theoretical analysis of our work and technical conversations, Dr. Kenneth Burch at Boston College for exciting collaboration opportunity on $\alpha-RuCl_3$, Dr. Mao at Pennsylvania State University for collaboration on type-II Weyl semiemtals. Dr. Luu at University of Arkansas for the opportunity to design quantum neural network, Dr. Wang for collaboration on nano-grids for biological applications, and Dr. Phatak for collaboration on Fe_3GeTe_2. We acknowledge support from National High Magnetic Field Laboratory at Tallahassee specially Dr. David Graf. In addition, we acknowledge support from U.S. Department of Energy, Office of Science, Basic Energy Sciences program. We acknowledge the MonArk NSF Quantum Foundry supported by the National Science Foundation.

Dedication

This work is dedicated to my beloved madar and pedar.

Table of Contents

List of Figures

Chapter 1

Introduction

1.1 Layered Topological Semimetals

Topology has played an increasingly important role in the study of quantum materials. The discovery of the Quantum Hall effect in 1981 [1] in Si and GaAs heterostructures was the first realization of topology in material science. The Quantum Hall effect is the coexistence of the robust quantized Hall conductivity with the absence of longitudinal conductivity at specific carrier densities set by the magnetic field. Numerous advancement has been followed, such as the discovery of quantum spin Hall effect [2, 3] in 2D systems, but shortly after, it was realized that topology play roles in other dimensions such as topological insulators [4, 5] in 3D systems, topological superconductors [6] in 1D, and Chern insulators [7] which is similar to Integer Quantum Hall effect in the absence of external magnetic field. In all the aforementioned cases, the largest spatial dimension of the system, such as bulk states, is insulating due to non-trivial topology, but the reduced dimensions, such as surface or edge states, are gap-less. Further studies demonstrated that topology is essential in gap-less bulk systems, such as semimetals [8–10].

To study the role of topology in semimetals, one needs to combine energy bands obtained from solving Schrödinger equation for the Bloch potential, $\hat{H}_0(K)|\psi_{0,n}(K)\rangle = E_{0,n}(K)|\psi_{0,n}(K)\rangle$ where subscript 0 denotes absence of electric and magnetic fields, with symmetry arguments in the presence of electric and magnetic fields.

When E,B$\neq$0, the average carrier velocity is given by the dispersion of energy bands.

$$\dot{X} = \frac{1}{\hbar}\frac{\partial E_{0,n}(K)}{\partial K} \longrightarrow \dot{X} = -\tilde{E}(K) \tag{1.1}$$

here $\tilde{E}(K) = -\frac{\partial E_{0,n}(K)}{\partial K}$ is the analogous of spatial electric field, but in the momentum space, and in natural units where $\hbar = e = 1$. Comparing equation 1.1 with Lorentz force, 1.2 in

similar units,

$$\dot{K} = -E(X) - \dot{X} \times B(X) \tag{1.2}$$

and considering that momentum for an observer in real space is equivalent to position for an observer in momentum space, X and K are interchangeable; one would expect equation 1.1 to have an additional term, $-\dot{K} \times \tilde{B}(K)$, similar to equation 1.2,

$$\dot{X} = -\tilde{E}(K) - \dot{K} \times \tilde{B}(K) \tag{1.3}$$

Here $\tilde{B}(K)$ is Berry flux, the magnetic field in momentum space, and is related to Berry Phase. In the following, the Berry phase is explained in more detail to illuminate the topological aspect of energy band dispersion.

1.1.1 Berry phase

Berry phase accounts for the change in the eigenstate of a system due to the adiabatic evolution of Hamiltonian in its parameter over time. Since the evolution is adiabatic the system must remain in the initial eigenstate over the course of evolution, but generally this is not true, $|\psi_n(t)\rangle \neq |\psi_n(t+\delta t)\rangle$. Hence, the Berry phase must be considered to account for the change in the eigenstate due to adiabatic evolution. In band theory, the adiabatic evolution of Hamiltonian in K over time t results in

$$|\psi_n(K(0))\rangle \longrightarrow e^{i(\gamma_n(t) - \int_0^t E_n(t')dt')} |\psi_n(K(0))\rangle \tag{1.4}$$

where $\int_0^t E_n(t')dt'$ is the dynamical phase and $\gamma_n(t)$ is the Berry phase. As mentioned $\gamma_n(t)$ accounts for the change in eigenstate of a system due to adiabatic evolution, $\langle\psi_n(K)\nabla_K|\psi_n(K)\rangle = \langle\psi_n(K(t+\delta t))|\psi_n(K(t))\rangle - \langle\psi_n(K(t))|\psi_n(K(t))\rangle$, hence Berry phase is

$$\gamma_n(t) = i \int_{K(0)}^{K(t)} dK \langle\psi_n(K)\nabla_K|\psi_n(K)\rangle \tag{1.5}$$

Usually, the overall phase of an eigenstate is not important due to gauge invariance, but in cases where the evolution is periodic, which is always the case in solids ($K = K + 2\pi$), the choice of gauge does not remove the overall phase [11], hence Berry phase is important. One can define the Berry curvature, $A_n(K) \equiv i\langle\psi_n(K)\Delta_K|\psi_n(K)\rangle$ and Berry flux, $\tilde{B} \equiv \nabla \times A$. Integrating over close loop C with corresponding area S and using Stoke's theorem,

$$\gamma_n(t) = \int_C A_n(K)dK = \int_S \tilde{B}.dS \tag{1.6}$$

which means the Berry phase for adiabatic evolution around a loop is equal to the integral of Berry flux through the loop. For non-zero Berry flux equation 1.3 might consist of a non zero $\dot{K} \times \hat{B}(K)$, this term is known as anomalous velocity, hence giving rise to various topological aspects of the band diagram.

1.1.2 Dirac and Weyl semimetals

Charge carriers might imitate the relativistic dynamics of high-energy particle physics due to the charge and crystal lattice interaction. Such imitation has been observed in various materials, including topological semimetals [12, 13], a family of materials that host topologically nontrivial and locally linear band crossing near Fermi energy (Fig. 1.1) and topologically protected surface states. Such band crossing gives rise to various exciting and technologically useful phenomenons, such as giant magnetoresistance and chiral anomaly [9, 10, 14, 15].

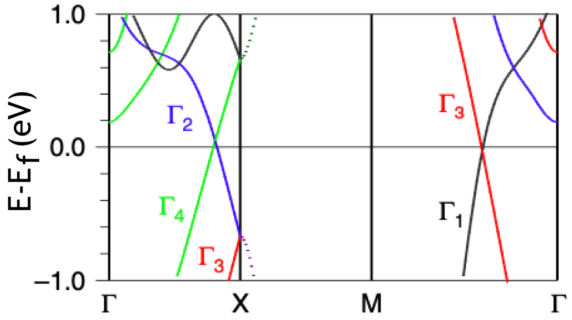

Figure 1.1: Close-up image of bulk band structure of ZrSiS without spin orbit coupling from Schoop et al. [16], colors of the lines represent a different irreducible representation of labeled bands. Band crossings of Γ_1-Γ_3, Γ_2-Γ_4, and Γ_2-Γ_3 are locally linear and are approximated with Dirac equation.

The Bloch Hamiltonian, $H(k)$, for a band crossing that is linear near the node, in general, is approximated by Dirac Hamiltonian, $H_D(k)$,

$$H_D(k) = \sum_{j=1}^{d} k_j \gamma_j \tag{1.7}$$

where γ_j are $4X4$ matrices obeying the anti-commutation relation $\{\gamma_i, \gamma_j\} = 2\delta_{ij}$ and d is the spatial dimension. Solving Schrödinger equation for $H_D(k)$ and finding the energy eigenvalues results in $E = \pm\sqrt{\sum_{j=1}^{d} k_j^2}$ which is a linear band crossing at $K = 0$, Dirac node. In 3D, if inversion symmetry and time reversal symmetry are preserved, then each band is two-fold degenerate; hence a Dirac node is four-fold degenerate [13]. Breaking time reversal or inversion symmetry lifts the degeneracy of bands and creates two band crossings known as Weyl nodes Fig. 1.2.

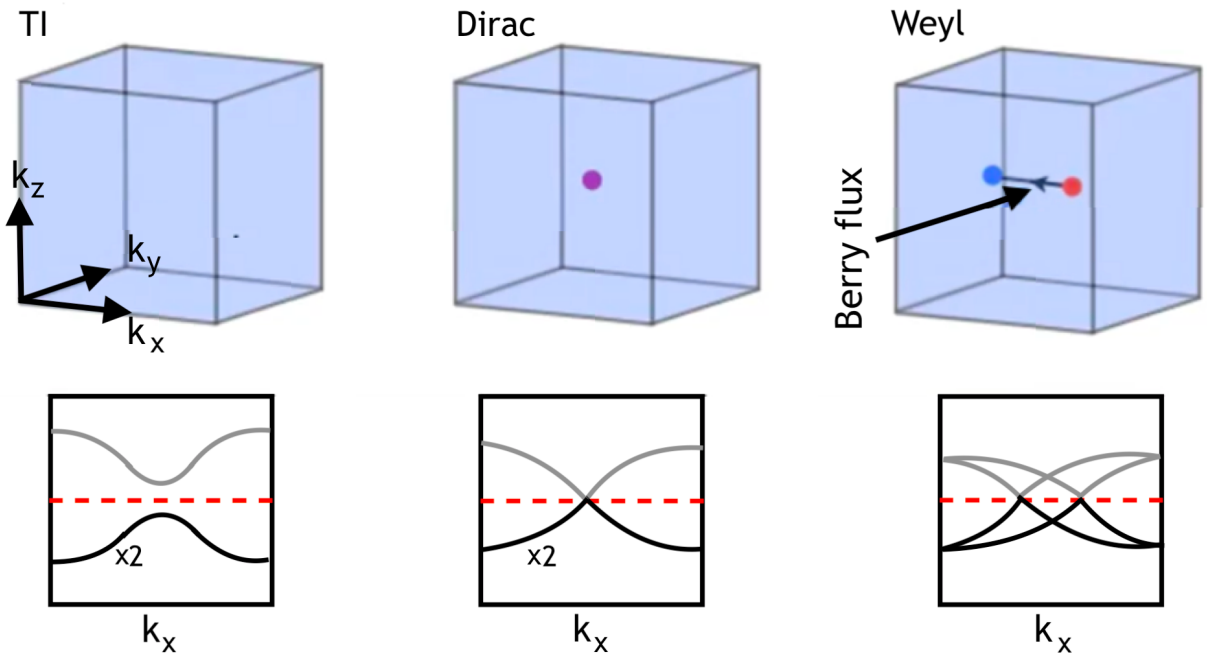

Figure 1.2: Comparison of topological insulator, Dirac semimetal, and Weyl semimetal. The bands in the topological insulator and Dirac semimetal are doubly degenerate. Breaking time-reversal symmetry and inversion symmetry in Dirac semimetal results in lifting of degeneracy and obtaining Weyl semimetal.

Weyl nodes are the band crossing of Weyl Hamiltonian , $H_W(k)$.

$$H_D(k) = \sum_{j=1}^{d} \hbar v_f k_j \sigma_j \tag{1.8}$$

Which is analogous to Dirac Hamiltonian, but γ_j are $2X2$ Pauli matrices, σ_j, where $\hbar$ is the Planck constant and v_f is the Fermi velocity. Pauli matrices are energetically locked parallel, positive chirality, or anti-parallel, negative chirality, to the momentum. Positive(negative) Weyl node is source(sink) of Berry flux, Berry monopole, Fig. 1.2. Since the momentum space of a crystal is a torus, $K = K + 2\pi$, Berry monopoles always come in pairs with opposite chirality. The net Berry flux through an arbitrary surface in momentum space is non-zero if the surface encloses an odd number of Berry monopoles. In contrast, the net Berry flux through the surface is zero for an even number of Berry monopoles. For a 2D slice of momentum space with non-zero Berry flux, a finite slab of material confined in the Z direction has surface states on top and bottom of material at the Fermi energy [8]. These surface states form Fermi arcs that connect the projection of Weyl nodes to the surface. The Fermi arc on the top surface is complementary to the Fermi arc on the bottom, forming a legitimate 2D Fermi surface. A Fermi arc connects the projection of Weyl nodes on the surface and cannot extinguish without the annihilation of bulk Weyl nodes, known as the bulk-surface correspondence, which is fundamentally different from other surface states that are completely decoupled from bulk.

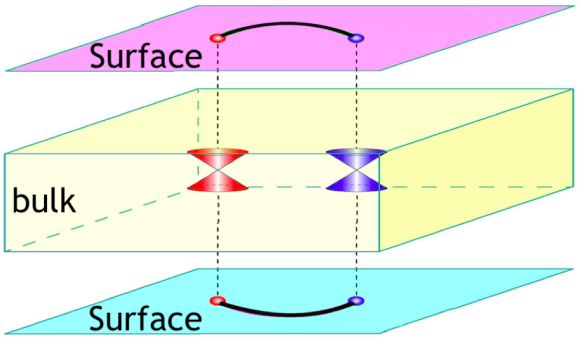

Figure 1.3: Schematic of a Weyl semimetal with Fermi arcs connecting the projection of Weyl nodes with opposite chirality on top and bottom surfaces.

Experimental observation of Fermi arc is possible through surface sensitive experiments such as ARPES [17, 18] and transport quantum oscillations[19, 20].

Weyl semimetals are predicted to occur in strongly spin-orbit coupled systems, [21, 22]. Cd_3As_2 and Na_3Bi are 3D Dirac semimetals, equivalent to two superimposed Weyl semimetals with opposite chirality. In the absence of symmetry, the overlapped Weyl nodes with opposite chirality in momentum space can gap out the band crossing, but in Dirac, semimetals intermixing is forbidden due to crystal symmetries, such as discrete screw symmetries in Cd_3As_2 and Na_3Bi[23, 24]. Further discussion of symmetries is provided in Sec. 1.1.4.

1.1.3 Nodal line semimetals

The concept of Dirac nodes is easily extended to higher dimensions, such as the Dirac nodal line, where a cone of an electron-like band intercepts a cone of the hole-like band. ZrSiS is a nodal line Dirac semimetal [16], with the nodal line tracing a diamond with four corners on high symmetry lines of band diagram, Fig. 1.4(a), starting from the Dirac node on the high symmetry line ΓX toward MΓ, AZ, ZR, and back to ΓX respectively, Fig. 1.4(b).

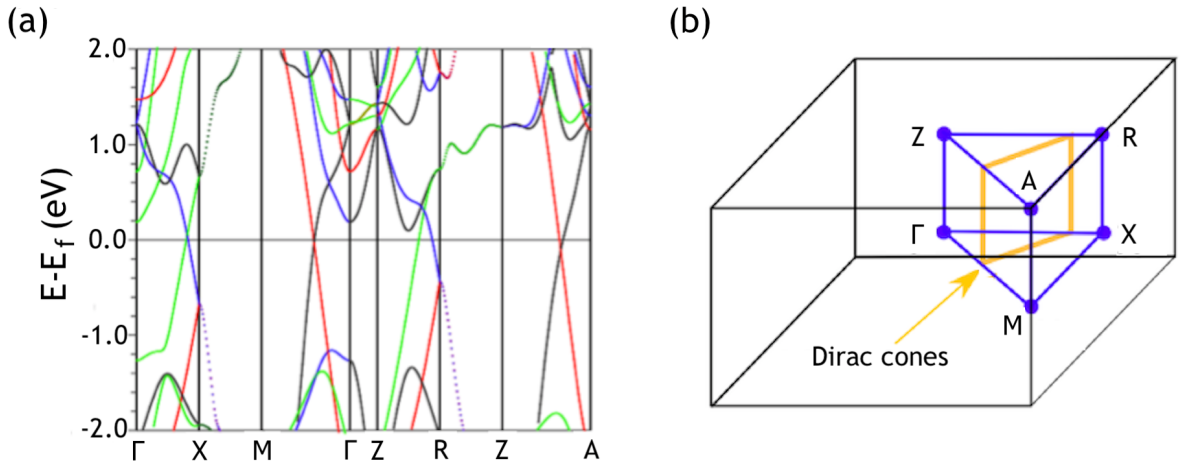

Figure 1.4: (a) Bulk band structure of ZrSiS without spin-orbit coupling from Schoop et al. [16]. Color coding is similar to Fig. 1.1. (b) Nodal lines are shown in orange in a primitive tetragonal lattice of ZrSiS, and high symmetry lines are in blue.

Although most of the Dirac nodes in the energy band diagram of ZrSiS form the Dirac nodal line, the Dirac nodes on R and X, Fig. 1.4, are distinguished and have different natures due to the underlying symmetry.

1.1.4 Symmetry protection

There are two categories of band crossing, accidental and symmetry-enforced [25]. Accidental band crossing results from the overlap between hole-like and electron-like bands where opposite symmetry or non-trivial topology protects the crossing. Symmetries that leave at least one point of the actual space of the crystal invariant, symmorphic symmetries, and symmetries that acts locally in the real space, non-spatial symmetries, protect accidental band crossings [25]. Although small symmetry-preserving perturbations move the accidental band crossing with no gap opening, sufficiently large symmetry-preserving deformation might open up a gap. In contrast, in the symmetry-enforced band crossing, a large symmetry-preserving deformation does not open a gap but might still move the band crossing [26]. Symmetry-enforced band crossings in bulk are protected by nonsymmorphic crystal symmetries, which realize Fermi surface of reduced dimensions [27]. In Fig. 1.1 the band crossings of Γ_1-Γ_3 and Γ_2-Γ_4 are accidental but Γ_2-Γ_3 is protected with nonsymmorphic symmetry [16], hence is symmetry-enforced.

1.2 Shubnikov-de Haas oscillations

Shubnikov-de Haas oscillations are the oscillation of longitudinal resistivity periodic in the inverse of the magnetic field. We will study these oscillations in Dirac/Weyl semimetals by studying Landau energies, which is the solution to the Schrödinger equation in the presence of a magnetic field utilizing the Landau gauge.

Choose a coordinate system in momentum space such that Weyl nodes are at $k_z = \pm k_0$ and the Hamiltonian governs the nodes in Eq. 1.8. If a magnetic field in the Z direction is applied, $\vec{B} = B\hat{z}$, then the Landau vector potential, $\vec{A} = (-By, 0, 0)$, changes the Hamiltonian

according to minimal coupling, $\vec{K} \longrightarrow \vec{K} + e\vec{A}$. The Hamiltonian Eq. 1.8 in natural units becomes

$$H(K) = \begin{pmatrix} v_f k_z & v_f(k_x - eBy) - iv_f k_y \\ v_f(k_x - eBy) + iv_f k_y & -v_f k_z \end{pmatrix} \tag{1.9}$$

This Hamiltonian is similar to a harmonic oscillator Hamiltonian with lowering and raising operators, a and $a^\dagger$, such that $[a, a^\dagger] = 1$ where

$$a = \frac{1}{\sqrt{2}l_B}(y - k_x l_B^2) + i\frac{l_B}{\sqrt{2}}k_y$$

where $l_B^2 = \frac{1}{eB}$ is the magnetic length in natural units. Rewriting the Hamiltonian Eq. 1.9 in terms of lowering and raising operators and solving similar to Harmonic oscillator [11] results in eigenvalues

$$E_n = \sqrt{2nv_f^2/l_B^2 + v_f^2 k_z^2} \tag{1.10}$$

centered at $y = k_x l_B^2$. These energies are degenerate due to the freedom in the center of oscillation, y; considering the quantization in $K_x = n\frac{2\pi}{L_x}$ the degeneracy will be $\frac{L_y L_x}{2\pi l_B^2}$, which is the total magnetic flux through the sample divided by magnetic flux quanta, $\Phi_0 = \frac{h}{e}$. Filling factor ν is number of electrons divided by degeneracy $\nu = \frac{n_e \Phi_0}{B}$. For the ground state, n=0, one needs to be more careful since the lowering operator can not lower the ground state anymore; hence it is required to apply the Hamiltonian to the ground state directly. For positive chirality, $\vec{K}$ is in the direction of $\vec{\sigma}$, $E_0^+ = -v_f K_z$ and for negative chirality, $\vec{K}$ is opposite to direction of $\vec{\sigma}$, $E_0^- = +v_f K_z$. In contrast to chiral bands, for $n > 0$, E_n can be both positive and negative, corresponding to electron and hole states, respectively.

The chiral dependence of the ground state gives rise to phenomena such as chiral anomaly, where the application of electric field in the same direction as magnetic field causes an imbalance between positive and negative chiral bands, Fig. 1.6(a).

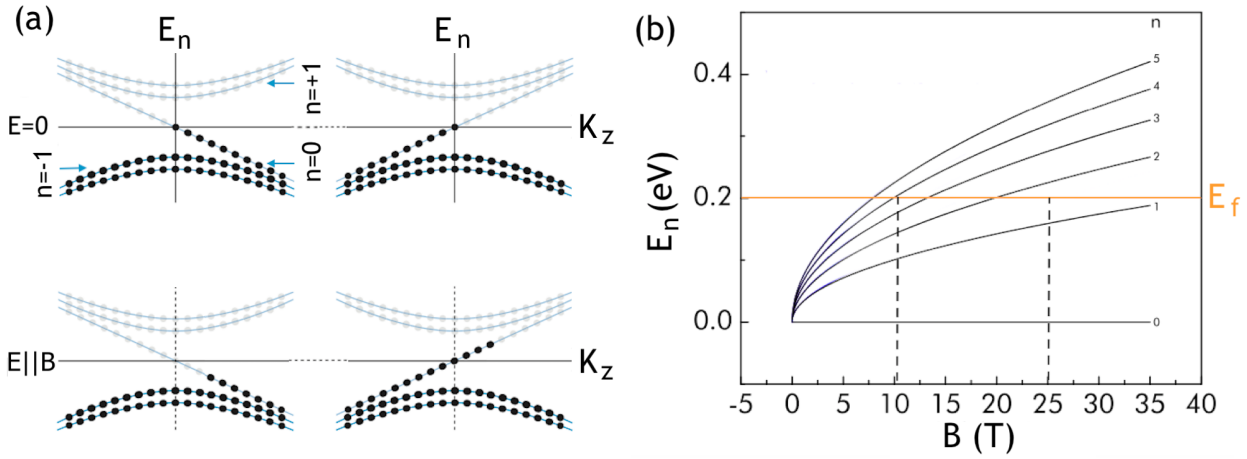

Figure 1.5: (a) Landau level spectrum of Weyl semimetal in the presence of external magnetic field along z direction from Burkov et al. [28]. Top set is the energy spectrum of positive and negative chiral ground state when the electric field in the z-direction is off. The bottom set is in the presence of an electric field E along B. (b) Landau energy spectrum of Cd_3As_2 for various levels as a function of the applied magnetic field in the z-direction from Moll et al. [20].

The average carrier velocity for the positive(negative) chiral band at n=0, Eq. 1.1, is negative(positive) in the z direction; hence one can think of chiral bands as a one-way conveyor which transfers Weyl charges from the top(bottom) surface to the bottom(top) surface of the material. Chiral bands also play an essential role in Fermi-arc mediated oscillations that is further discussed in next chapter.

Landau energy spectrum of Cd_3As_2, a Dirac semimetal with $E_f \approx 0.2$ eV, is shown in Fig. 1.5(b). The increasing magnetic field increases the Landau energy according to Eq. 1.10. This means the number of filled Landau levels decreases as the magnetic field increase as they are pushed above Fermi energy; for example, in Cd_3As_2 at 10 T only 5 energy levels are below Fermi energy but at 25 T this decreases to 2. This results in modulation of density-of-states at Fermi energy, introducing Shubnikov-de Haas oscillations as non-localized carriers in Landau levels that were below Fermi energy in the valence band become accessible for transport as soon as their energy hits the Fermi energy. However, as the magnetic field increases, they go above Fermi energy; hence they will fade away and no longer participate in transport [29].

The cyclotron frequency of carriers is evident from the comparison of lowering or raising operators with a harmonic oscillator, $\sqrt{\frac{1}{2l_B^2}} = \sqrt{\frac{m^*\omega_c}{2}}$, $\omega_c = \frac{eB}{m^*}$. The effective mass m^* is experimentally accessible from the temperature dependence of quantum oscillations, damped by the thermal broadening of Landau levels. This thermal damping is described by the thermal component of the Lifshitz-Kosevich formula [30],

$$\frac{\Delta\rho}{\rho_0} = \frac{5}{2}\sqrt{\frac{B}{2F}}\frac{\frac{2\pi^2 K_B T}{\hbar\omega_c}}{sinh(\frac{2\pi^2 K_B T}{\hbar\omega_c})}e^{-\frac{2\pi^2 K_B T_D}{\hbar\omega_c}}cos(2\pi(\frac{F}{B}+\Gamma-\delta)) \tag{1.11}$$

Here $\Delta\rho$ is the change in resistivity due to oscillation, ρ_0 is the longitudinal resistivity at zero magnetic field, K_B is the Boltzmann constant, F is oscillation frequency, $\Gamma = \frac{1}{2} - \frac{\gamma}{2\pi}$ where γ is Berry phase, and δ is the phase shift determined by dimensionality of Fermi surface, 0 for 2D and $\pm\frac{1}{8}$ for 3D. Effective mass is obtained from fitting Eq. 1.11 to the $\Delta\rho$ at a constant magnetic field.

Onsager's relation suggests that quantum oscillation frequency, F, is proportional to the maximum cross-section of the Fermi surface, $S(K_f)$, divided by flux quanta. $F = \frac{S(K_f)\Phi_0}{4\pi^2}$. For most materials, the 3D Fermi surface can be approximated as a sphere; hence $S(K_f) = \pi K_f^2$, where K_f is the Fermi wave vector. This suggests we can find the Fermi wave vector of a Fermi surface from quantum oscillation frequency,

$$k_f = \sqrt{\frac{4\pi eF}{h}} \tag{1.12}$$

The Fermi velocity, v_f, and Fermi energy, E_f, is

$$v_f = \frac{\hbar k_f}{m^*} \qquad E_f = \hbar v_f k_f \tag{1.13}$$

Assuming a 3D Fermi surface is spherical implies that $S(K_f)$ is constant for all directions of magnetic field piercing the sample. Hence the quantum oscillation frequency is constant for all field directions. On the other hand, for a 2D Fermi surface, the effective cross-section is inversely proportional to $cos(\theta)$, where θ is the angle between the magnetic field and the

normal vector to the Fermi surface if the magnetic field is perpendicular to the Fermi surface maximum flux quanta pierce it while for magnetic fields in the plane with the Fermi surface has Zero flux quanta passing through, hence the frequency of 2D Fermi surface is inversely proportional to $cos(\theta)$. To experimentally distinguish a 3D Fermi surface from a 2D one, one can sweep the magnetic field over various angles between the current through the sample and the field. In the case of a 2D Fermi surface, the oscillation frequency will blue shift as $1/cos(\theta)$. Fig. 1.6 shows the angular dependence of Shubnikov-de Haas oscillation frequency, obtained from Fast Fourier Transform, as a function of the magnetic field. The bulk frequency, $F_B = 215$ T, is constant over various angles while the surface frequency, $F_S = 450$ T, is inversely proportional to $cos(\theta)$, Fig. 1.6(c).

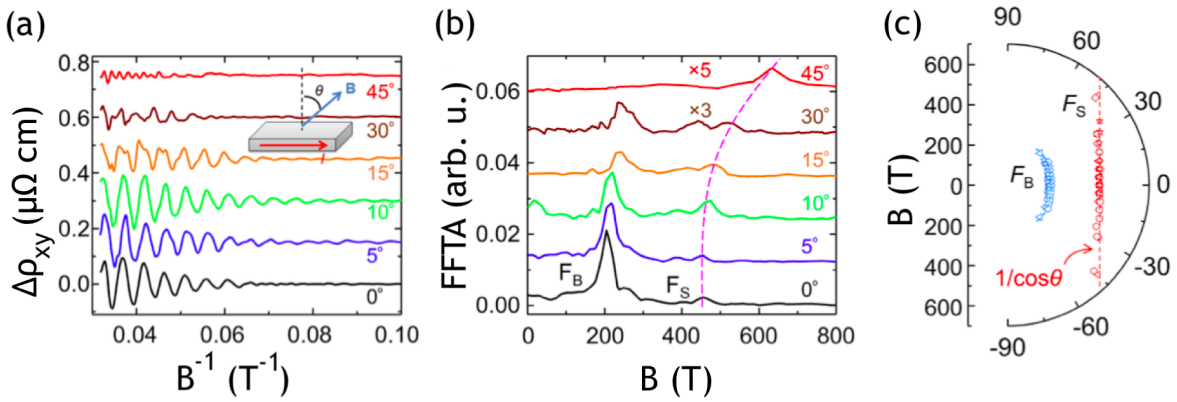

Figure 1.6: (a) Angular dependence of quantum oscillation in ρ_{xy} for a ZrSiSe device from Liu et al. [31]. The inset is their experiment's schematic and definition of angle θ. (b) The fast Fourier transform of quantum oscillations shows an oscillation frequency of 215 T and 450 T. The smaller frequency has a slight to no change in frequency over various angles; hence the corresponding oscillations are from a 3D Fermi surface, while the larger frequency change with angle; hence it is of a 2D Fermi surface. (c) shows that the oscillation frequency is shifted as $1/cos(\theta)$

Oscillation amplitude and frequency of quantum oscillations are discussed in detail up to this point. The phase is the last piece to obtain a minimal picture of any oscillatory system. The phase in quantum oscillation is the intercept of Landau index, n, as a function of B^{-1}, $n(B^{-1})$ at $B^{-1} = 0$ ($B = \infty$ T). Usually, this function is linear because the oscillations are periodic in B^{-1}, but other physical phenomena, such as spin-orbit coupling, can cause

deviation from linearity. This makes the analysis of the quantum oscillation phase ambiguous unless a sufficiently low Landau index is observable in the measurement. In cases where sufficiently low Landau levels are not accessible, it might be possible to fit a line to the linear part of $n(B^{-1})$ by assuming an arbitrary initial Landau index and adjusting n accordingly such that the fit intercept n axis between n=0 and n=1. This approach is less ambiguous for linear B^{-1} dependence and is not as accurate when other quantum phenomena are involved.

Although this section covered the basics of quantum oscillations of closed Fermi surfaces, the surface of Weyl semimetals consists of open Fermi surfaces known as Fermi arcs, as described in Sec. 1.1.2. The signature of the Fermi arc is observable in quantum oscillation and illuminates the topological character of bulk Weyl semimetals. The next chapter reports fundamentals and advances in studying Fermi arc-mediated quantum oscillations.

1.3 Weyl orbit quantum oscillation

As mentioned in Sec. 1.2, quantum oscillations are a powerful method to map a closed Fermi surface; similarly, these oscillations can probe open Fermi surface, Fermi arcs, in a slab of Weyl semimetals or their symmetry-protected analogues, Dirac semimetals, of finite thickness [19]. Fermi arcs on surfaces of material participate in a closed orbit of charge carriers under a magnetic field by traversing the bulk of material from top to bottom surface and vice versa, connecting the Fermi arc on the top surface to its counter part on the bottom surface, forming a closed magnetic orbit. This closed orbit is derived by transferring chirality from one end of the Fermi arc to the other, in contrast to conventional cyclotron orbits derived by Lorentz force. This oscillation is possible only up to a critical magnetic field that depends on the slab thickness.

Consider a coordinate system such that the Weyl nodes with opposite chirality are separated in the X direction, $K = \pm\frac{K_0}{2}\,\hat{x}$, and the magnetic field is applied in the Z direction. As mentioned in Sec. 1.2 the magnetic field produces Landau levels along the direction of the

magnetic field, Eq. 1.10. For a slab of Weyl semimetal that is finite in the Z direction with thickness L, such that the slab is sufficiently thick to neglect direct tunneling between the top and bottom surface, an electron on the top surface near the + chirality Weyl node with momentum K_x slides along the Fermi arc toward − chirality Weyl node in the momentum space according to Lorentz force, Eq. 1.2 $\partial_t K = ev_f B\hat{t}_k$, where $\hat{t}_k$ is the unit vector tangential to Fermi arc and v is the velocity. Near the − chirality Weyl node, the energy gap of the bulk vanishes, resulting in transferring electrons from the surface to the bulk, where the chiral Landau levels are the only available bulk states. As mentioned in Sec. 1.1.2, the velocity of these chiral states are $+v_f$ and $-v_f$ for positive and negative chirality, respectively; hence they act like a conveyor belt and transfer electrons from the top surface to the bottom surface and vice versa 1.7.

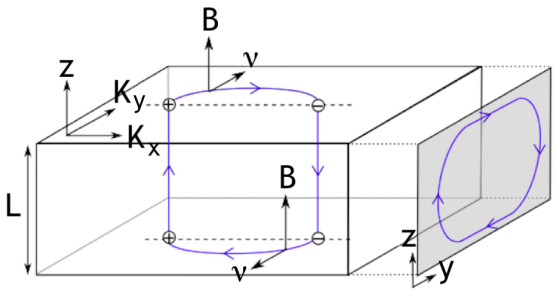

Figure 1.7: Semi-classical Fermi arc mediated orbit in a magnetic field along Z direction with Fermi arc surface states giving rise to quantum oscillations in a finite slab in the y-z spatial surface.

In this semiclassical orbit, the energy levels have to satisfy $E_n t = 2\pi(n+\gamma)$ [19], where t is the time of orbit, n is the quantization energy and γ is a constant of order unity accounting for low n quantum effects. Considering carriers traverse the Fermi arc approximately in $t_{arc} \approx \frac{\hbar K_0}{ev_f B}$ and the bulk in $t \approx \frac{L}{v_f}$, the E_n is

$$E_n = \frac{\pi v_f (n+\gamma)}{L + K_0 l_B^2} \tag{1.14}$$

Similar to Landau levels Sec. 1.2, at energies that $E_n = E_f$ where the energy levels pass the Fermi energy, a peak happens in the density of states, sweeping over magnetic field push the energy levels above Fermi energy according to Eq. 1.14, which in turn cause quantum

oscillation in B^{-1}. Re-writing Eq. 1.14 in term of B^{-1} and E_f,

$$B_n^{-1} = \frac{e\pi v_f}{K_0 E_f}(n+\gamma) - \frac{eL}{K_0} \tag{1.15}$$

hence the oscillation frequency, F_{arc} is

$$F_{arc} = (B_{n+1}^{-1} - B_n^{-1})^{-1} = \frac{E_f K_0}{e\pi v_f} = \frac{\hbar k_f K_0}{e\pi} \tag{1.16}$$

A practical condition on Weyl orbit is that scattering should not disrupt a full orbit, that is $\omega_c\tau >> 1$ where $\omega_c \equiv \frac{ev_f B}{2\hbar K_0}$ and τ is the elastic scattering time and related to mean free path, l, as $\tau = \frac{l}{v_f}$. In addition, the magnetic field must be smaller than the saturation field $B_{sat} = \frac{\hbar K_0}{eL}$ because for $B > B_{sat}$ the majority of orbits happen in bulk. Although, in this orbit, the assumption is that electrons will traverse all the length of the Fermi arc, a careful analysis shows that electrons jump off the arc into the bulk when the momentum is within l_B^{-1} of the bulk Weyl node [19], $K_0 \longrightarrow K_0 - \alpha l_B^-1$ where α is a constant of order unity. At low fields, this effect is small, but at high fields results in B_{sat}. These two conditions imply that $L << l$ to observe such an orbit for Dirac semimetals where the mean free path is usually several hundred nm.

Although the oscillation frequency does not depend on the thickness of the material Eq. 1.16, the angle and chemical potential independent piece in Eq. 1.15, $\frac{eL}{K_0}$, is thickness dependent. This piece is the intercept of B_n^{-1} versus n, similar to the phase in Landau level analysis. Thickness dependence of phase in this oscillation is a good indicator of Fermi-arc mediation.

Such oscillations also happen in Dirac semimetal but with additional complications. Since Dirac semimetals are two copies of Weyl semimetals and are protected by symmetry, their surface exhibit two sets of Fermi-arc that curve in opposite directions and join at a sharp corner at the Weyl nodes, similar to a 2D Fermi surface, such a sharp kink is not allowed in a 2D Fermi surface and is a unique feature of Weyl semimetals.

One of the complications can be the symmetry reduction at the surface of Dirac semimetals; for example, the bulk Dirac nodes in Cd_3As_2 and Na_3Bi are protected by a discrete rotation symmetry which is broken at the surface. Naively, this broken symmetry can gap out the sharp kink of Fermi arcs resulting in conventional surface states, but this does not happen since Fermi arcs wave function spread into the bulk where the protection symmetry is still intact [19]. Other complications are symmetry reduction in a magnetic field and the effect of bulk topology on the surface states when the axial crystal symmetry is weakly broken, which has been responded to in Potter et al. [19].

1.4 Transition-metal thiophosphates

Magnetism in mono-layer limit has been predicted and observed in various van der Waals materials, such as CrX_3 [32–34], $CrSiTe_3$ and $CrGeTe_3$ [35–37], MPX_3 [38, 39]. Many efforts have been focused on magnetic phase transition induced by strain or electrostatic gate in mono-layer limit [40, 41].

Transition-metal chalcogenophosphates, MPX_3 (M=Mn,Fe,Ni,V. and X=S,Se,Te), are layered materials that mostly have antiferromagnetic order in mono-layer limit[42, 43], for example mono-layer $MnP(S,Se)_3$ exhibit Neel antiferromagnetism. These materials were initially interesting because of their suitable inter-layer space for Li intercalation to serve as battery materials. Although strong electronic correlations specially on the metal atoms can make them suitable for various applications, it makes basic ab initio density functional calculation less reliable, unless those correlations are considered, even though those basic calculations can provide considerable insight into the potential for engineering magnetic properties. Chittari et al. ab initio calculations [42] indicate that most of these materials in 2D limit are antiferromagnet semiconductors and larger atomic numbers of chalcogen reduces the energy gap. These materials are Mott insulators [44, 45] with medium to relatively large band gap, such as 250 meV in VPS_3 to 1.5 eV in $FePS_3$.

Experimental studies found that bulk Mn, Fe, Co, and Ni thiophosphate have antiferromagnetic ground states with Neel temperatures of almost 100 K [46, 47], some of which extend down to the monolayer limit. Theoretical ab initio calculations using GGA+D2 approximation show that the ground state of most MPX_3 materials, in the 2D limit, are of antiferromagnet (AFM); especially important compounds are VPS_3, $NiPS_3$, and $MnPSe_3$ that are AFM, and $FePS_3$ which is zAFM.

Chittari et al. [42] predicted an electrostatic field modification of magnetic properties in these materials similar to ferromagnetic semiconductors that variation of carrier density in thin films causes modification of magnetic exchange interaction. Fig. 1.8 shows their prediction for some of the compounds we studied. In addition to electrostatic modulation, one can use strain for a similar purpose. They studied the influence of in-plain strain on magnetic phase transition and found that less than 10 % of strain can cause a phase transition in most of these materials. Although these results are promising because correlation is relatively strong in these materials, primary forms of ab initio calculations are not quantitatively reliable for all properties of these materials [42]. Even some of these calculations are found to be in contrast with experimental results; for example, the calculation of band structure by ab initio based on generalized gradient approximation suggests semiconductive [48, 49] and semimetallic behavior [50], in contrast to experiments that show Mott insulation [51–53].

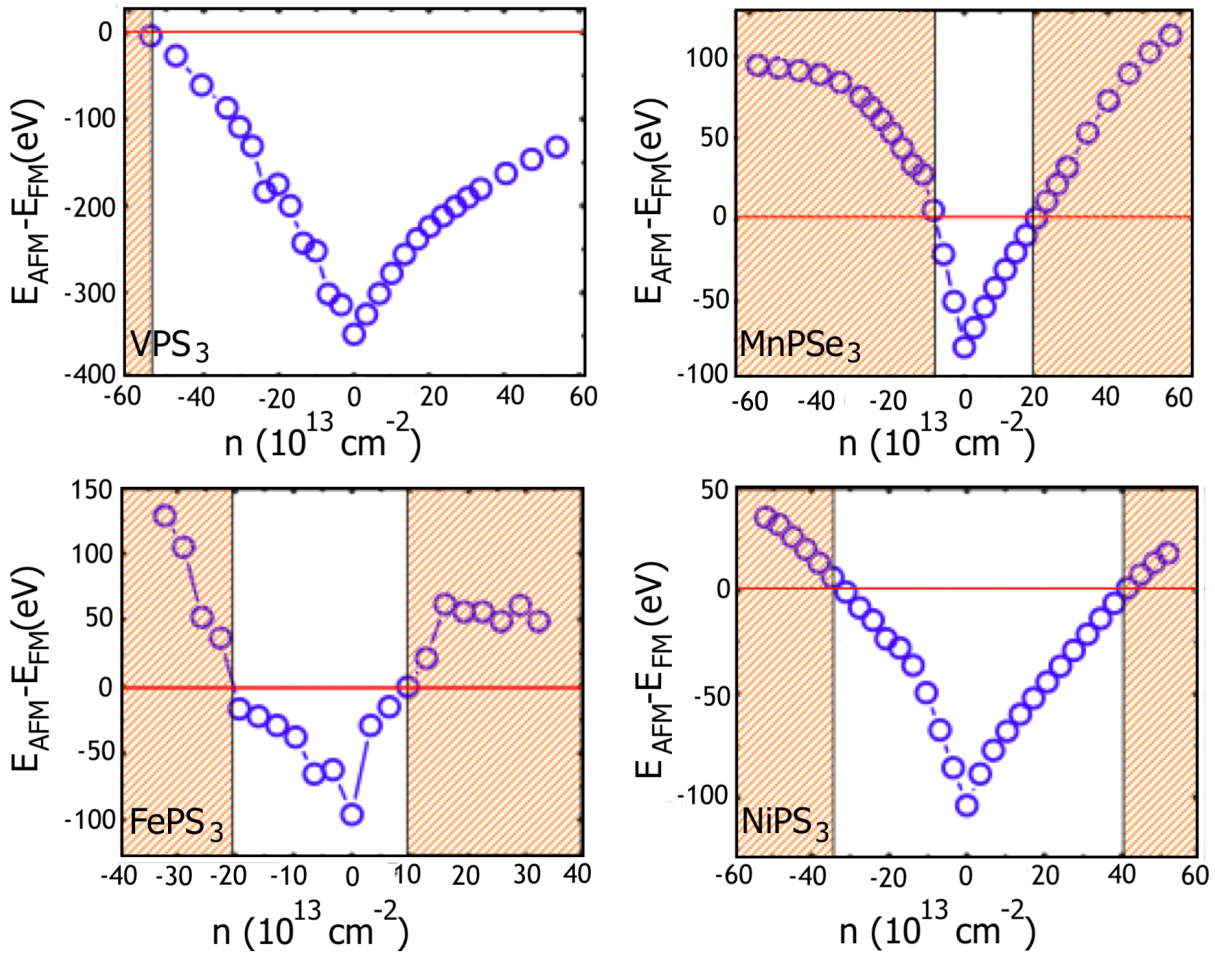

Figure 1.8: The difference between ground state energy of VPS_3, $NiPS_3$, $MnPSe_3$, and $FePS_3$ in AFM phase and FM phase as a function of carrier density from Chittari et al. [42]. Near charge neutrality, all of these materials are in the AFM phase because the ground state energy in the AFM phase is less than in the FM phase. At sufficiently high carrier densities highlighted by orange color, the ground state of the FM phase is more favorable than the AFM phase.

In contrast to basic forms of ab initio calculations, which are not reliable for this family of material, experiments can reveal reliable results. An exciting result of experiments is the pressure-induced Mott-insulator metal transition, which is observed using high pressure x-ray diffraction for $FePS_3$ at 140 Kbar [45], $MnPS_3(Se_3)$ at 300(240) Kbar [52], and VPS_3 at 112 Kbar [44]. Raman study shows that this transition is due to the stiffness of interplanar

vibration modes, which can be interpreted as a cross-over from 2D conduction channels to 3D conduction channels [53].

It has been speculated that the magnetic properties of these materials are correlated with transport properties, such as the upturn in the temperature dependence of resistivity in $FePS_3$ and VPS_3 that has been suggested to root in the Kondo effect or similar magnetic-related phenomenons [44, 45]. The magnetic data of Coak et al. [44] shows a transition from the antiferromagnetic phase to the paramagnetic phase when VPS_3 changes from Mott-insulator to metal.

The magnetism of such materials is probed by various techniques such as Kerr microscopy [54–56], spin-induced linear polarization of photoluminescence [57], and neutron diffraction techniques [58]. In addition, the correlation between magnetism and transport can be used to probe magnetism. Tunneling measurements are a well-established transport approach to study magnetism, even in insulators that are antiferromagnetic within each layer, such as $MnPS_3$ [43]. In the following section, we will review the details of such experiments on MPX_3.

1.5 Probing magnetism via tunneling

Temperature dependence of magnetoresistance in antiferromagnetic tunneling devices can detect a phase transition in the magnetic state of the material, hence providing information about the magnetic phase diagram of these materials. Carriers that tunnel through layered magnetic insulators show higher current if the magnetization of layers is in the same direction compared to opposite directions [59, 60], hence measuring tunneling resistance can be used as a probe of magnetism in nano-materials. The reason is that when carriers tunnel through a ferromagnetic material, the carriers with spin up and spin down see different potential barriers, which results in different transmission probability, even up to orders of magnitude Fig. 1.9. This effect is known as the spin-filtering effect and is the basis of various spintronic devices

[61]. The smaller barrier for spin-up results in a larger tunneling current compared to opposite spins; hence the tunneling current can be used as a direct measure of magnetism. In addition to ferromagnetism, spin filtering is similarly effective for probing the antiferromagnetic phase. Assume two layers of materials with opposite magnetic moments on top of each other; the tunneling current through the first layer is spin filtered and encounters the second layer with opposite magnetization; hence it drops more. This is the basis of spin-tunnel field effect transistors [62, 63].

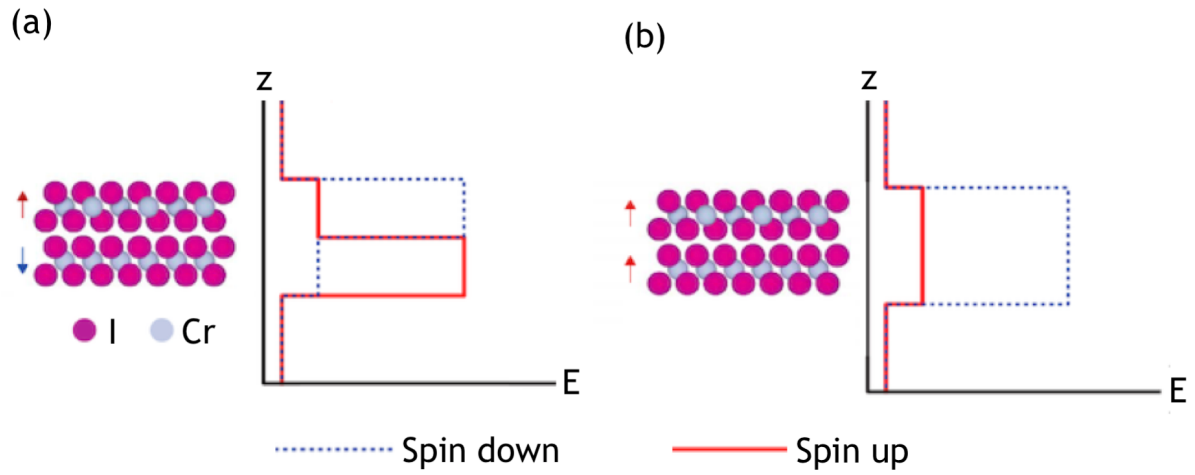

Figure 1.9: Schematic of potential barrier of bilayer CrI_3 in spatial direction for spin up and spin down electron.

A study of tunneling resistance can lighten the magnetic properties of ferromagnetic materials within each layer, such as CrI_3. In addition, it can illuminate magnetic properties of antiferromagnetic materials within each layer, such as $MnPS_3$ [43]. In this material, the spin of manganese atoms is ordered antiferromagnetic within each layer in a zigzag pattern, pointing almost perpendicular to the ab plane at temperatures below T_n=78 K [64]. At sufficiently large field, perpendicular to ab plane, a spin flop transition happens such that the spin flop toward the b axis [65]. This is because the exchange energy gets larger than the anisotropy energy. Experimental evidence of such spin flop transition is reported in few-layer [66] and monolayer [43] of $MnPS_3$.

The temperature dependence of the resistance can be used to distinguish tunneling transport from classical transport in tunneling heterostructures. At low temperatures, the resistance has a weak temperature dependency, while thermally activated carriers can contribute at high temperatures, which means a strong temperature dependency. A linear I-V curve at low temperatures in a tunneling regime indicates direct tunneling, which can happen only in a few layers of material. For thicker material flake, the tunneling happens in the Fowler-Nordheim regime [67, 68] where the current density through the tunneling region is proportional to an exponential function of the inverse of the voltage, V, across the tunnel.

$$ln(\frac{j}{V^2}) = -\frac{4\sqrt{2m^*\Phi_B^3}}{3\hbar e}\frac{d}{V} + C \tag{1.17}$$

Where m^* is the effective mass, Φ_B is the potential barrier height, d is the thickness of the flake, and C is the proportionality constant. The slope of $ln(\frac{j}{V^2})$ versus $\frac{d}{V}$ for at least two different thickness can reveal m^* and Φ_B.

Similar to measurements of longitudinal conductivity, one can use two probes or four probes geometry measured in DC/AC configuration or perform dI/dV measurements to obtain tunneling resistance.

References

[1] Klaus Von Klitzing. The quantized hall effect. *Reviews of Modern Physics*, 58(3):519, 1986.

[2] Charles L Kane and Eugene J Mele. Quantum spin hall effect in graphene. *Physical review letters*, 95(22):226801, 2005.

[3] B Andrei Bernevig and Shou-Cheng Zhang. Quantum spin hall effect. *Physical review letters*, 96(10):106802, 2006.

[4] M Zahid Hasan and Charles L Kane. Colloquium: topological insulators. *Reviews of modern physics*, 82(4):3045, 2010.

[5] Joel E Moore. The birth of topological insulators. *Nature*, 464(7286):194–198, 2010.

[6] Anindya Das, Yuval Ronen, Yonatan Most, Yuval Oreg, Moty Heiblum, and Hadas Shtrikman. Zero-bias peaks and splitting in an al–inas nanowire topological superconductor as a signature of majorana fermions. *Nature Physics*, 8(12):887–895, 2012.

[7] Emil J Bergholtz and Zhao Liu. Topological flat band models and fractional chern insulators. *International Journal of Modern Physics B*, 27(24):1330017, 2013.

[8] Xiangang Wan, Ari M Turner, Ashvin Vishwanath, and Sergey Y Savrasov. Topological semimetal and fermi-arc surface states in the electronic structure of pyrochlore iridates. *Physical Review B*, 83(20):205101, 2011.

[9] Andrei Bernevig, Hongming Weng, Zhong Fang, and Xi Dai. Recent progress in the study of topological semimetals. *Journal of the Physical Society of Japan*, 87(4):041001, 2018.

[10] Jin Hu, Su-Yang Xu, Ni Ni, and Zhiqiang Mao. Transport of topological semimetals. *Annual Review of Materials Research*, 49:207–252, 2019.

[11] Neil W Ashcroft, N David Mermin, et al. Solid state physics, 1976.

[12] M Mofazzel Hosen, Klauss Dimitri, Ilya Belopolski, Pablo Maldonado, Raman Sankar, Nagendra Dhakal, Gyanendra Dhakal, Taiason Cole, Peter M Oppeneer, Dariusz Kaczorowski, et al. Tunability of the topological nodal-line semimetal phase in zrsi x-type materials (x= s, se, te). *Physical Review B*, 95(16):161101, 2017.

[13] NP Armitage, EJ Mele, and Ashvin Vishwanath. Weyl and dirac semimetals in three-dimensional solids. *Reviews of Modern Physics*, 90(1):015001, 2018.

[14] Junchao Ma, Ke Deng, Lu Zheng, Sanfeng Wu, Zheng Liu, Shuyun Zhou, and Dong Sun. Experimental progress on layered topological semimetals. *2D Materials*, 6(3):032001, 2019.

[15] Md Rafique Un Nabi, Aaron Wegner, Fei Wang, Yanglin Zhu, Yingdong Guan, Arash Fereidouni, Krishna Pandey, Rabindra Basnet, Gokul Acharya, Hugh OH Churchill, et al. Giant topological hall effect in centrosymmetric tetragonal mn 2- x zn x sb. *Physical Review B*, 104(17):174419, 2021.

[16] Leslie M Schoop, Mazhar N Ali, Carola Straßer, Andreas Topp, Andrei Varykhalov, Dmitry Marchenko, Viola Duppel, Stuart SP Parkin, Bettina V Lotsch, and Christian R Ast. Dirac cone protected by non-symmorphic symmetry and three-dimensional dirac line node in zrsis. *Nature communications*, 7(1):1–7, 2016.

[17] Su-Yang Xu, Ilya Belopolski, Nasser Alidoust, Madhab Neupane, Guang Bian, Chenglong Zhang, Raman Sankar, Guoqing Chang, Zhujun Yuan, Chi-Cheng Lee, et al. Discovery of a weyl fermion semimetal and topological fermi arcs. *Science*, 349(6248):613–617, 2015.

[18] LX Yang, ZK Liu, Yan Sun, Han Peng, HF Yang, Teng Zhang, Bo Zhou, Yi Zhang, YF Guo, Marein Rahn, et al. Weyl semimetal phase in the non-centrosymmetric compound taas. *Nature physics*, 11(9):728–732, 2015.

[19] Andrew C Potter, Itamar Kimchi, and Ashvin Vishwanath. Quantum oscillations from surface fermi arcs in weyl and dirac semimetals. *Nature communications*, 5(1):1–6, 2014.

[20] Philip JW Moll, Nityan L Nair, Toni Helm, Andrew C Potter, Itamar Kimchi, Ashvin Vishwanath, and James G Analytis. Transport evidence for fermi-arc-mediated chirality transfer in the dirac semimetal cd3as2. *Nature*, 535(7611):266–270, 2016.

[21] Gang Chen and Michael Hermele. Magnetic orders and topological phases from f-d exchange in pyrochlore iridates. *Physical Review B*, 86(23):235129, 2012.

[22] William Witczak-Krempa and Yong Baek Kim. Topological and magnetic phases of interacting electrons in the pyrochlore iridates. *Physical Review B*, 85(4):045124, 2012.

[23] Zhijun Wang, Hongming Weng, Quansheng Wu, Xi Dai, and Zhong Fang. Three-dimensional dirac semimetal and quantum transport in cd 3 as 2. *Physical Review B*, 88(12):125427, 2013.

[24] ZK Liu, Bo Zhou, Yong Zhang, ZJ Wang, HM Weng, Dharmalingam Prabhakaran, S-K Mo, ZX Shen, Zhong Fang, Xi Dai, et al. Discovery of a three-dimensional topological dirac semimetal, na3bi. *Science*, 343(6173):864–867, 2014.

[25] Ching-Kai Chiu, Jeffrey CY Teo, Andreas P Schnyder, and Shinsei Ryu. Classification of topological quantum matter with symmetries. *Reviews of Modern Physics*, 88(3):035005, 2016.

[26] Seng Huat Lee, David Graf, Lujin Min, Yanglin Zhu, Hemian Yi, Samuel Ciocys, Yuanxi Wang, Eun Sang Choi, Rabindra Basnet, Arash Fereidouni, et al. Evidence for a magnetic-field-induced ideal type-ii weyl state in antiferromagnetic topological insulator mn (bi 1- x sb x) 2 te 4. *Physical Review X*, 11(3):031032, 2021.

[27] YX Zhao and Andreas P Schnyder. Nonsymmorphic symmetry-required band crossings in topological semimetals. *Physical Review B*, 94(19):195109, 2016.

[28] AA Burkov. Topological semimetals. *Nature materials*, 15(11):1145–1148, 2016.

[29] David Shoenberg. *Magnetic oscillations in metals*. Cambridge university press, 2009.

[30] Jin Hu, JY Liu, David Graf, SMA Radmanesh, DJ Adams, Alyssa Chuang, Yu Wang, Irinel Chiorescu, Jiang Wei, Leonard Spinu, et al. π berry phase and zeeman splitting of weyl semimetal tap. *Scientific reports*, 6(1):1–8, 2016.

[31] Xue Liu, Chunlei Yue, Sergey V Erohin, Yanglin Zhu, Abin Joshy, Jinyu Liu, Ana M Sanchez, David Graf, Pavel B Sorokin, Zhiqiang Mao, et al. Quantum transport of the 2d surface state in a nonsymmorphic semimetal. *Nano letters*, 21(11):4887–4893, 2021.

[32] Wei-Bing Zhang, Qian Qu, Peng Zhu, and Chi-Hang Lam. Robust intrinsic ferromagnetism and half semiconductivity in stable two-dimensional single-layer chromium trihalides. *Journal of Materials Chemistry C*, 3(48):12457–12468, 2015.

[33] Michael A McGuire, Hemant Dixit, Valentino R Cooper, and Brian C Sales. Coupling of crystal structure and magnetism in the layered, ferromagnetic insulator cri3. *Chemistry of Materials*, 27(2):612–620, 2015.

[34] Bevin Huang, Genevieve Clark, Efrén Navarro-Moratalla, Dahlia R Klein, Ran Cheng, Kyle L Seyler, Ding Zhong, Emma Schmidgall, Michael A McGuire, David H Cobden, et al. Layer-dependent ferromagnetism in a van der waals crystal down to the monolayer limit. *Nature*, 546(7657):270–273, 2017.

[35] B Siberchicot, S Jobic, V Carteaux, P Gressier, and G Ouvrard. Band structure calculations of ferromagnetic chromium tellurides crsite3 and crgete3. *The Journal of Physical Chemistry*, 100(14):5863–5867, 1996.

[36] Sébastien Lebègue, T Björkman, Mattias Klintenberg, Risto M Nieminen, and Olle Eriksson. Two-dimensional materials from data filtering and ab initio calculations. *Physical Review X*, 3(3):031002, 2013.

[37] Cheng Gong, Lin Li, Zhenglu Li, Huiwen Ji, Alex Stern, Yang Xia, Ting Cao, Wei Bao, Chenzhe Wang, Yuan Wang, et al. Discovery of intrinsic ferromagnetism in two-dimensional van der waals crystals. *Nature*, 546(7657):265–269, 2017.

[38] Xiao Li, Ting Cao, Qian Niu, Junren Shi, and Ji Feng. Coupling the valley degree of freedom to antiferromagnetic order. *Proceedings of the National Academy of Sciences*, 110(10):3738–3742, 2013.

[39] Xingxing Li, Xiaojun Wu, and Jinlong Yang. Half-metallicity in mnpse3 exfoliated nanosheet with carrier doping. *Journal of the American Chemical Society*, 136(31):11065–11069, 2014.

[40] Yandong Ma, Ying Dai, Meng Guo, Chengwang Niu, Yingtao Zhu, and Baibiao Huang. Evidence of the existence of magnetism in pristine vx2 monolayers (x= s, se) and their strain-induced tunable magnetic properties. *ACS nano*, 6(2):1695–1701, 2012.

[41] Shengwei Jiang, Lizhong Li, Zefang Wang, Kin Fai Mak, and Jie Shan. Controlling magnetism in 2d cri3 by electrostatic doping. *Nature nanotechnology*, 13(7):549–553, 2018.

[42] Bheema Lingam Chittari, Youngju Park, Dongkyu Lee, Moonsup Han, Allan H MacDonald, Euyheon Hwang, and Jeil Jung. Electronic and magnetic properties of single-layer m p x 3 metal phosphorous trichalcogenides. *Physical Review B*, 94(18):184428, 2016.

[43] Gen Long, Hugo Henck, Marco Gibertini, Dumitru Dumcenco, Zhe Wang, Takashi Taniguchi, Kenji Watanabe, Enrico Giannini, and Alberto F Morpurgo. Persistence of magnetism in atomically thin mnps3 crystals. *Nano letters*, 20(4):2452–2459, 2020.

[44] Matthew J Coak, Suhan Son, Dominik Daisenberger, Hayrullo Hamidov, Charles RS Haines, Patricia L Alireza, Andrew R Wildes, Cheng Liu, Siddharth S Saxena, and Je-Geun Park. Isostructural mott transition in 2d honeycomb antiferromagnet v0. 9ps3. *npj Quantum Materials*, 4(1):1–6, 2019.

[45] CRS Haines, Matthew J Coak, Andrew R Wildes, Giulio I Lampronti, Cheng Liu, Paul Nahai-Williamson, Hayrullo Hamidov, Dominik Daisenberger, and Siddharth S

Saxena. Pressure-induced electronic and structural phase evolution in the van der waals compound feps 3. *Physical Review Letters*, 121(26):266801, 2018.

[46] Raymond Brec. Review on structural and chemical properties of transition metal phosphorus trisulfides mps 3. In *Intercalation in Layered Materials*, pages 93–124. Springer, 1986.

[47] AR Wildes, B Roessli, B Lebech, and KW Godfrey. Spin waves and the critical behaviour of the magnetization in. *Journal of Physics: Condensed Matter*, 10(28):6417, 1998.

[48] MH Whangbo, R Brec, Gt Ouvrard, and J Rouxel. Reduction sites of transition-metal phosphorus trichalcogenides mpx3. *Inorganic Chemistry*, 24(15):2459–2461, 1985.

[49] Vladlen Zhukov, Santiago Alvarez, and Dmitrii Novikov. Electronic band structure of the magnetic layered semiconductors mps3 (m= mn, fe and ni). *Journal of Physics and Chemistry of Solids*, 57(5):647–652, 1996.

[50] Yusuke Sugita, Takashi Miyake, and Yukitoshi Motome. Multiple dirac cones and topological magnetism in honeycomb-monolayer transition metal trichalcogenides. *Physical Review B*, 97(3):035125, 2018.

[51] Takahiro Matsuoka, Amanda Haglund, Rui Xue, Jesse S Smith, Maik Lang, Antonio M dos Santos, and David Mandrus. Pressure-induced insulator–metal transition in two-dimensional mott insulator nips3. *Journal of the Physical Society of Japan*, 90(12):124706, 2021.

[52] Yonggang Wang, Zhengyang Zhou, Ting Wen, Yannan Zhou, Nana Li, Fei Han, Yuming Xiao, Paul Chow, Junliang Sun, Michael Pravica, et al. Pressure-driven cooperative spin-crossover, large-volume collapse, and semiconductor-to-metal transition in manganese (ii) honeycomb lattices. *Journal of the American Chemical Society*, 138(48):15751–15757, 2016.

[53] Matthew John Coak, Yong-Hyun Kim, Yoo Soo Yi, Suhan Son, Sung Keun Lee, and Je-Geun Park. Electronic and vibrational properties of the two-dimensional mott insulator v 0.9 ps 3 under pressure. *Physical Review B*, 100(3):035120, 2019.

[54] DA Allwood, Gang Xiong, MD Cooke, and RP Cowburn. Magneto-optical kerr effect analysis of magnetic nanostructures. *Journal of Physics D: Applied Physics*, 36(18):2175, 2003.

[55] CR Zhu, K Zhang, M Glazov, B Urbaszek, Thierry Amand, ZW Ji, BL Liu, and Xavier Marie. Exciton valley dynamics probed by kerr rotation in wse 2 monolayers. *Physical Review B*, 90(16):161302, 2014.

[56] Taskeya Haider. A review of magneto-optic effects and its application. *Int. J. Electromagn. Appl*, 7(1):17–24, 2017.

[57] Xingzhi Wang, Jun Cao, Zhengguang Lu, Arielle Cohen, Hikari Kitadai, Tianshu Li, Qishuo Tan, Matthew Wilson, Chun Hung Lui, Dmitry Smirnov, et al. Spin-induced linear polarization of photoluminescence in antiferromagnetic van der waals crystals. *Nature Materials*, 20(7):964–970, 2021.

[58] Andrew R Wildes, Virginie Simonet, Eric Ressouche, Garry James Mcintyre, Maxim Avdeev, Emmanuelle Suard, Simon AJ Kimber, Diane Lançon, Giulio Pepe, Boujemaa Moubaraki, et al. Magnetic structure of the quasi-two-dimensional antiferromagnet nips 3. *Physical Review B*, 92(22):224408, 2015.

[59] Tiancheng Song, Xinghan Cai, Matisse Wei-Yuan Tu, Xiaoou Zhang, Bevin Huang, Nathan P Wilson, Kyle L Seyler, Lin Zhu, Takashi Taniguchi, Kenji Watanabe, et al. Giant tunneling magnetoresistance in spin-filter van der waals heterostructures. *Science*, 360(6394):1214–1218, 2018.

[60] Hyun Ho Kim, Bowen Yang, Siwen Li, Shengwei Jiang, Chenhao Jin, Zui Tao, George Nichols, Francois Sfigakis, Shazhou Zhong, Chenghe Li, et al. Evolution of interlayer and intralayer magnetism in three atomically thin chromium trihalides. *Proceedings of the National Academy of Sciences*, 116(23):11131–11136, 2019.

[61] Dahlia R Klein, David MacNeill, Jose L Lado, David Soriano, Efrén Navarro-Moratalla, Kenji Watanabe, Takashi Taniguchi, Soham Manni, Paul Canfield, Joaquín Fernández-Rossier, et al. Probing magnetism in 2d van der waals crystalline insulators via electron tunneling. *Science*, 360(6394):1218–1222, 2018.

[62] Shengwei Jiang, Lizhong Li, Zefang Wang, Jie Shan, and Kin Fai Mak. Spin tunnel field-effect transistors based on two-dimensional van der waals heterostructures. *Nature Electronics*, 2(4):159–163, 2019.

[63] Hyun Ho Kim, Shengwei Jiang, Bowen Yang, Shazhou Zhong, Shangjie Tian, Chenghe Li, Hechang Lei, Jie Shan, Kin Fai Mak, and Adam W Tsen. Magneto-memristive switching in a 2d layer antiferromagnet. *Advanced Materials*, 32(2):1905433, 2020.

[64] Eric Ressouche, Mickael Loire, Virginie Simonet, Rafik Ballou, Anne Stunault, and Andrew Wildes. Magnetoelectric mnps 3 as a candidate for ferrotoroidicity. *Physical Review B*, 82(10):100408, 2010.

[65] Darren J Goossens, AR Wildes, C Ritter, and Trevor J Hicks. Ordering and the nature of the spin flop phase transition in mnps3. *Journal of Physics: Condensed Matter*, 12(8):1845, 2000.

[66] Dinh Hoa Luong, Thanh Luan Phan, Ganesh Ghimire, Dinh Loc Duong, and Young Hee Lee. Revealing antiferromagnetic transition of van der waals mnps3 via vertical tunneling electrical resistance measurement. *APL Materials*, 7(8):081102, 2019.

[67] John G Simmons. Generalized formula for the electric tunnel effect between similar electrodes separated by a thin insulating film. *Journal of applied physics*, 34(6):1793–1803, 1963.

[68] M Lenzlinger and EH Snow. Fowler-nordheim tunneling into thermally grown sio2. *Journal of Applied physics*, 40(1):278–283, 1969.

Chapter 2

Enhancement of Transport Properties in 2D Topological Semimetals

Observation of intrinsic quantum transport properties of 2D topological semimetals can be challenging due to the suppression of high mobility caused by extrinsic factors introduced during fabrication. We demonstrate current annealing to substantially improve the electronic transport properties of 2D topological semimetal flakes. Contact resistance and resistivity were improved by factors up to 2×10^6 and 2×10^4, respectively, in devices based on exfoliated flakes of two topological semimetals, ZrSiSe and $BaMnSb_2$. Using this method, carrier mobility in ZrSiSe improved by a factor of 3800, resulting in the observation of record-high mobility for exfoliated ZrSiSe. Quantum oscillations in annealed ZrSiSe appeared at magnetic fields as low as 5 T, and magnetoresistance increased by 10^4. We argue that a thermal process underlies this improvement. Finally, Raman spectroscopy and analysis of quantum oscillations in ZrSiSe indicate that the phonon modes and Fermi surface area are unchanged by current annealing.

2.1 Introduction

Topological semimetals (TSMs) are intensely studied due to their novel and technologically useful properties such as giant magnetoresistance and chiral anomaly [1–4]. Many TSMs, for example WHM (W=Zr/Hf/La, H=Si/Ge/Sn/Sb, M=O/S/Se/Te) [5–7] and $BaMnSb_2$ [8], have layered structures with weak interlayer bonding, making them suitable for exfoliation to produce two-dimensional (2D) flakes and fabricate electronic devices. Accessing quantum transport in thin TSMs can be challenging due to degradation of material quality following exfoliation and device fabrication. Surface oxidation and impurities introduced during fabrication often lead to higher resistivity relative to bulk and high contact resistance. Impurities in TSMs not only interrupt carrier transport as scattering sites, but also can break the symmetry-protected band structure of TSMs [9, 10].

To eliminate impurities and defects in 2D devices, thermal annealing is commonly used [11–14]. Finding proper annealing conditions by varying annealing gas, vacuum level, gas flow rate, temperature and time is essential for successful thermal annealing. These conditions vary by material, contact metal and even flake thickness. The numerous variables involved in the process make discovery of proper annealing conditions a tedious task. As a simpler alternative, current annealing was first introduced to our knowledge for 2D devices with suspended graphene [15], resulting in observation of the fractional quantum Hall effect. This annealing process was studied in detail by Wang et al. [16], who showed via *in situ* SEM imaging that the underlying mechanism is a thermal process. A similar method was used by Liu et al. [17] to current-anneal the TSM ZrSiSe. Following a voltage-biased current annealing approach, they noted an improvement in contact resistance caused by break-down of the oxidation layer between ZrSiSe and the contact metal.

Here we demonstrate that current annealing also improves the resistivity of the TSM in addition to reducing contact resistance. Using a current-biased technique to anneal the 2D flakes, we extend this method to two TSMs exfoliated as flakes, ZrSiSe and $BaMnSb_2$. Comparison of devices with and without pre-treatment by thermal annealing in vacuum suggests a thermal origin for this effect, and Raman spectroscopy before and after annealing indicates that the structure and chemical composition of the materials are unaffected by this process. In the case of ZrSiSe flakes, for example, we obtain record-high mobilities and access to quantum oscillations at relatively low magnetic fields ($\sim$5 T) following current annealing. This technique is a rapid and *in situ* method to recover the high mobility and large magnetoresistance characteristic of TSMs after exfoliation to 2D form.

2.2 Experimental Methods

We fabricated Hall bar devices on two different TSMs (ZrSiSe, $BaMnSb_2$) in top- and bottom-contacted geometries. Schematics and pictures of fabricated top- and bottom-contacted Hall bar devices are shown in Fig.2.1a and Fig.2.1b, respectively. ZrSiSe and $BaMnSb_2$

crystals were exfoliated inside a nitrogen glovebox (H_2O, $O_2 < 0.5$ ppm) on high-resistivity Si substrates (>10,000 Ω·cm) with 300 nm of thermal oxide. Flakes with proper thickness were first identified by optical microscopy using a hermetic cell with optical access [18], and then thickness was measured using atomic force microscopy, Fig. **??**. Top-contacted devices were fabricated with and without thermal treatment following exfoliation by thermal treatment in vacuum at 500 °C for 3 h immediately preceding the lithography step to define the contacts. Thermal treatment was not done for bottom-contacted devices to avoid degradation of the contact metal.

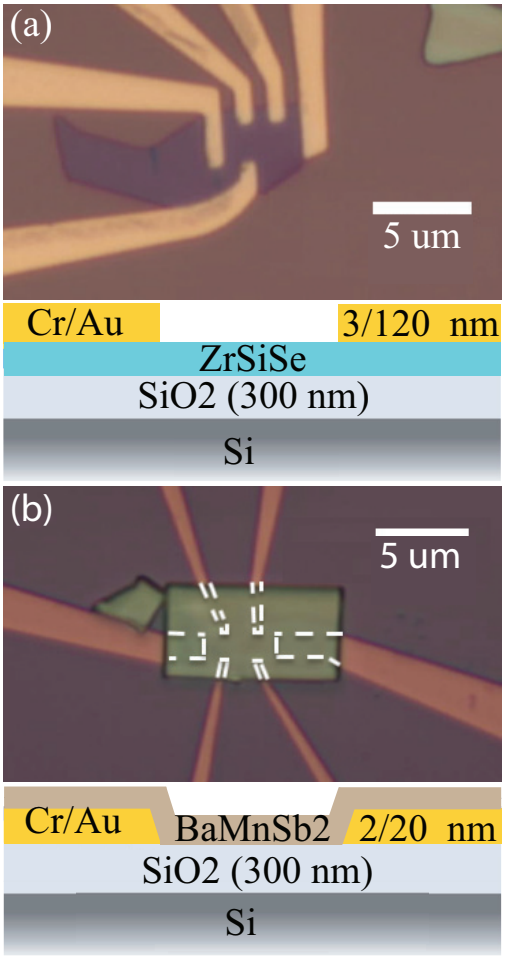

Figure 2.1: Cross section and optical micrograph of (a) top-contacted ZrSiSe device with gold contacts in a Hall bar geometry patterned on top of the flake and (b) bottom-contacted $BaMnSb_2$ device with the flake transferred onto pre-patterned Hall bar gold contacts.

To pattern Hall bar contacts on the flakes, PMMA C4 resist was spun on the chip in air and baked at 180 °C inside the glovebox, followed by electron beam lithography. PMMA dissolved in chlorobenzene was used because the more commonly used anisole-based resists were found to degrade the quality of ZrSiSe samples. For top-contacted ZrSiSe devices 3/120 nm Cr/Au contacts were thermally evaporated, Fig.2.1a. The total air exposure in this process was limited to be less than 5 minutes to minimize degradation of ZrSiSe, . Bottom-contacted $BaMnSb_2$ devices were prepared starting with electron beam lithography to pattern 2/20 nm Cr/Au Hall bar contacts. To facilitate thin flake exfoliation of BaMnSb2, we intercalated the single crystal by electrochemical lithiation to reduce interlayer bonding, and exfoliated the flakes using a method similar to You et al. [19]. Crystals were mechanically exfoliated inside the glove box and thin flakes were identified in the hermetic inspection cell. Thin flakes were transferred onto the contacts using a dry transfer method involving PDMS and PPC [20] inside the glove box, Fig.2.1b.

DC I-V curves were measured pre(post)-annealing at room temperature and pressure. Magnetoresistance, Hall resistivity, and quantum oscillations were measured at 4 K using standard lock-in techniques. During all pre-annealing measurements the current was kept below 0.1 μA to prevent unwanted annealing. Current annealing was performed at room temperature and pressure using a current source with amplitude controlled by the AC output of a lock-in amplifier, and a digital multimeter was used to monitor the voltage across the contacts during the current annealing process. In this way current (I), source-drain bias (V_b), and four-terminal longitudinal voltage (V_{xx}) were all measured simultaneously. In our annealing procedure, the source and drain contacts were annealed first. The drain was grounded while the source was connected to the output of the current source. The compliance voltage of the current source was set to 2.5 V with 100 nA/V gain, resulting in an initial minimal current of 0.4 nA forced through the flake. The current was then increased up to 4 mA by increasing the control voltage and current source gain, as needed. After source-drain annealing, other contacts were annealed by the same method. Finally, we measured I-V

curves, magnetoresistance, Hall resistivity, and quantum oscillations with a 0.1 μA current bias.

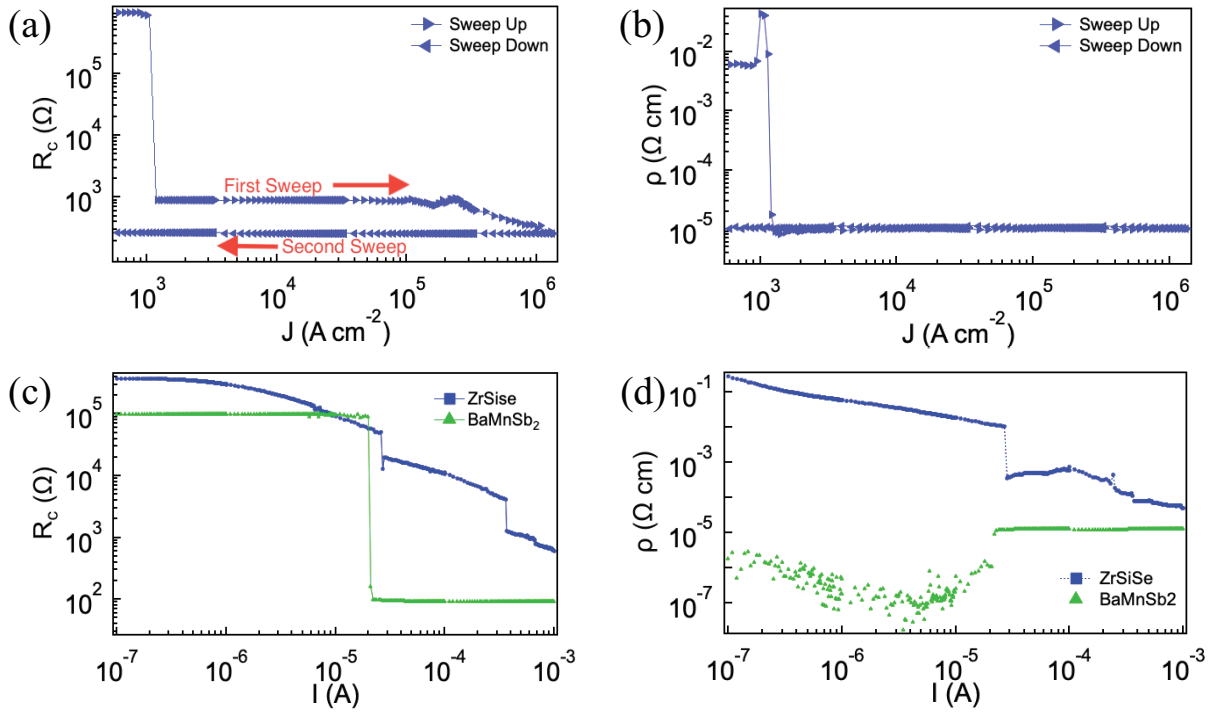

Figure 2.2: The effect of current annealing process on (a) contact resistance, R_c, and (b) intrinsic resistivity, ρ, of device ZSS-A as a function of current density. The direction of triangles shows the current sweep direction. (c) and (d) are the plots of R_c and ρ, respectively, as a function of current for ZSS-B and $BaMnSb_2$ devices.

2.3 Results

We extracted the four-point resistivity of each device as $\rho = (V_{xx}/I) \cdot (wt/l_{in})$, where w is the width of the sample, t is the thickness, and l_{in} is the length between the inner voltage probes. Contact resistance was calculated as $R_c = V_{sd}/I - \rho(l/wt)$, where l is the full length of the sample between source and drain contacts. Both contact resistance and resistivity decreased with source-drain current annealing. Figures 2.2a,b show R_c and ρ as a function of current density for a top-contacted, thermally-treated ZrSiSe device, ZSS-A. A change in both R_c and ρ occurs at a current density of 10^3 A/cm^2, reducing R_c from 960 kΩ to 280 Ω, and ρ

from 6 mΩ·cm to 10 $\mu\Omega$·cm. The resistivity shows only one jump in the annealing process of thermally-treated devices (see also Fig. S3 of the Supplementary Materials of chapter 1). Figures 2.2c,d show R_c and ρ during current annealing for a top-contacted ZrSiSe device with no thermal treatment, ZSS-B, and bottom contacted $BaMnSb_2$. Annealing decreased R_c of ZSS-B from 380 kΩ to 600 Ω, and R_c of $BaMnSb_2$ from 98 kΩ to 90 Ω. Resistivity decreased from 0.28 Ω·cm to 51 $\mu\Omega$·cm in ZSS-B. We note that in Fig.2.2d for currents below 20 μA for $BaMnSb_2$, a valid measurement of resistivity was not possible due to poor contact quality, but at 20 μA, the device annealed, enabling a measurement of resistivity for higher currents. In contrast with the thermally treated device ZSS-A with a single jump down in restivity, the resistivity of ZSS-B (not thermally treated) shows a more complicated trajectory toward lower resistivity as a function of current bias, with a gradual decrease, a sudden jump down, and another (nonmonotonic) gradual decrease.

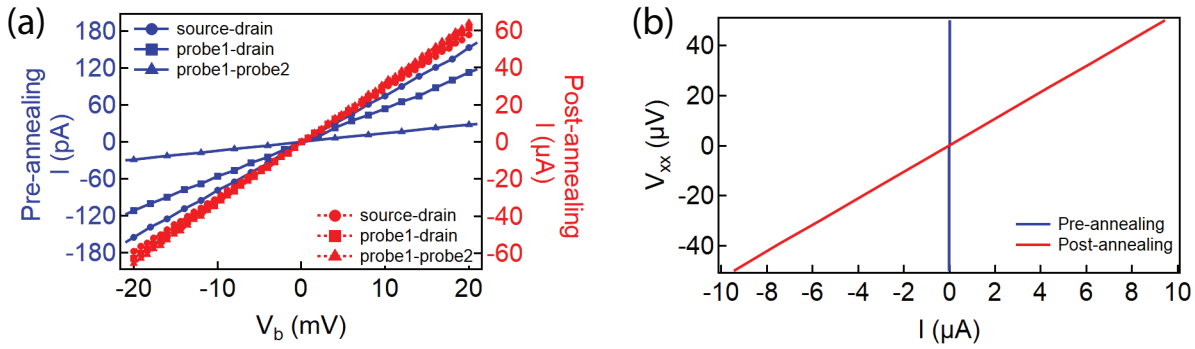

Figure 2.3: (a) DC I-V curves of device ZSS-C. Source, Probe1, Probe2, and Drain are defined from end to end in a 4-probe resistance measurement geometry, respectively. I-V curves for pairs of source-drain (circle), probe1-drain (square) and probe1-probe2 (triangle) are plotted. Pre(post)-annealing curves are shown with solid blue(dashed red) lines and the values are reflected on left(right) axis. (b) is the V_{xx}-I curves of the same device.

Turning now to DC I-V curves, Fig. 2.3 compares DC I-V curves pre- and post-annealing for a top-contacted ZrSiSe device without thermal treatment, ZSS-C,Fig. 2.9. Resistance extracted from the I-V curves changed from $R_i = 131$ MΩ to $R_f = 344$ Ω for source to drain, showing improvement by a factor 3.8×10^5. Resistance from probe to drain changed from 178 MΩ to

322 Ω and probe to probe changed from 744 MΩ to 312 Ω, showing improvement factors of 5.5×10^5 and 2.3×10^6, respectively. Figure 2.3b shows the DC four-probe V_{xx}-I measurement of device ZSS-C. Prior to annealing this device had $\rho = 0.45$ Ω·cm and annealing reduced it to $\rho = 26$ μΩ·cm, an improvment factor of 1.7×10^4.

Next we discuss the magnetotransport of device ZSS-B measured under out-of-plane magnetic field. Examining resistivity as a function of magnetic field (Fig. 2.4b) and also including the transverse resistivity (Fig. 2.4a), we see that the annealing procedure permits the observation of quantum oscillations in ZrSiSe at moderate magnetic fields. Here the magnetoresistance defined as $MR = \frac{\rho_{xx}(B)-\rho_{xx}(0)}{\rho_{xx}(0)}$ and was measured at 4 K for both pre- and post-annealing. Before annealing, the magnetoresistance is small, 0.5% at 7.5 T, with low signal to noise ratio. Annealing increased the magnetoresistance significantly, reaching 6000% at 7.5 T and corresponding to an improvement factor of 1.2×10^4. We note also that the signal to noise ratio improves significantly for the same experimental conditions. No quantum oscillations were observable pre-annealing, but post-annealing, quantum oscillations appeared above 4.5 T in both Hall resistivity (Fig. 2.4a), and magnetoresistance (Fig. 2.4b). To isolate the bulk quantum oscillations, a quadratic background [21] was subtracted from magnetoresistance and a high-pass finite impulse response filter with the cut off frequency of 150 T was applied. The result is plotted as a function of inverse of field, as shown in Fig. 2.4c. The fast Fourier transform (FFT) of the oscillations (Fig. 2.4d) shows the frequency of 215 T which matches well with the oscillation frequency of the bulk Fermi surface of ZrSiSe [7].

Because quantum oscillations are an important tool to study topological quantum materials, the observation and improvement of quantum oscillations at low field by *in situ* current annealing in the thin flake limit provides a useful approach to study 2D topological materials. The previous quantum oscillation study on very thin ZrSiSe samples has revealed an additional frequency of 445 T in high field (up to 31 T) transport measurements, which arises from the 2D floating surface state due to breaking the nonsymmorphic symmetry at the crystal

surface [17]. Such a surface state oscillation is not observed in this work, which could be attributed to the fact that the measurements were performed at relatively low magnetic field (up to 7.5 T) and the ZrSiSe flake used here is relatively thick,Fig.2.7, so that the bulk state dominates the transport at lower field.

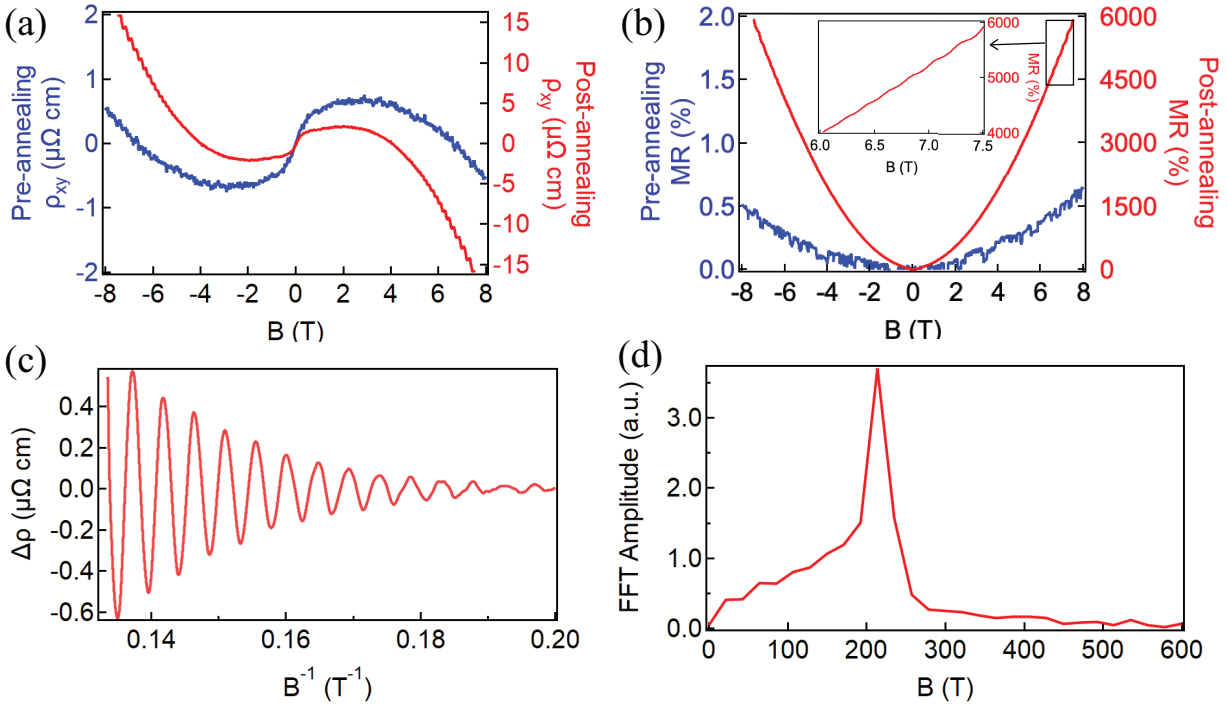

Figure 2.4: Comparison of (a) Hall resistivity and (b) magnetoresistance of device ZSS-B pre-annealing (blue curves) with post-annealing (red curves). Values of pre(post)-annealing magnetoresistance are shown on left(right) axis of (b). Quantum oscillation in the post-annealing sample can seen in both Hall resistivity (a) and magnetoresistance (inset of b). (c) Oscillatory component of magnetoresistance in (b), obtained by subtracting the smooth quadratic background. (d) FFT of the oscillations shown in (c).

Examining the same data for device ZSS-B, we obtained magnetoconductivity of device ZSS-B before and after current annealing (Fig. 4) by inverting the resistivity tensor $\sigma(B) = \frac{\rho_{xx}(B)}{\rho_{xx}^2(B)+\rho_{xy}^2(B)}$, where $\rho_{xx}(B)$ is the longitudinal resistivity and $\rho_{xy}(B)$ is the transverse resistivity. Post-annealing, the conductivity is more than three orders of magnitude higher than pre-annealing, and the dependence of conductance on magnetic field is larger by a similar factor. To obtain the carrier density and mobility of device ZSS-B, we fit the magnetocon-

ductivity to a two-band model [3, 22, 23], $\sigma(B) = \frac{1}{\rho_1 + A_1 B^2} + \frac{1}{\rho_2 + A_2 B^2}$ where $\rho_i = \frac{1}{n_i e \mu_i}$ and $A_i = \frac{\mu_i}{n_i e}$, with μ and n the mobility and carrier density, respectively. As shown in Fig. 2.5, the two-band model yields a satisfactory fit (black dashed lines) to the measured data, from which the carrier densities and mobilities are extracted and presented in Table 2.1. Current annealing increased the electron and hole mobility by factors of 3800 and 85, respectively; in contrast, the electron and hole densities remained nearly unchanged. These densities are in the expected range of $\sim 10^{19}\ cm^{-3}$ for bulk crystals of this nodal-line semimetal [7].

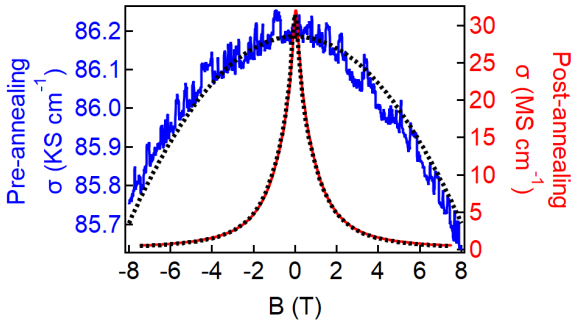

Figure 2.5: Left(right) axis: Conductance as a function of perpendicular magnetic field of device ZSS-B pre(post)-annealing displayed in blue(red). Black dashed lines are fits to the two-band model.

	Pre-annealing	Post-annealing
n_e	2.1×10^{19}	2.2×10^{19}
μ_e	11	4.2×10^4
n_h	6.8×10^{19}	9.8×10^{19}
μ_h	96	8.2×10^3

Table 2.1: carrier density ($\frac{1}{cm^3}$) and mobility ($\frac{cm^2}{V.S}$) obtained from fitting a two-band model to the magnetoconductance of ZSS-B, Fig. 2.5.

To investigate whether the current annealing process changes the structure or chemical composition of the 2D flakes, we performed Raman spectroscopy pre- and post-annealing of the same device and compared to the spectrum of a bulk crystal of ZrSiSe (Fig. 2.6a). The intensities are normalized with respect to tallest ZrSiSe peak at 238 cm^{-1}. Fits to a Lorentzian profile were used to extract the frequency and area under each peak (Fig. 2.6b), as well as the half width at half maximum of each peak (Fig. 2.6c). The half width at half maximum and frequencies of the Raman modes of the unannealed reference flake are similar to both annealed and bulk devices at all peaks. While all three spectra are largely similar, the most significant difference between the spectra is that the area under the peaks at 154 cm^{-1}

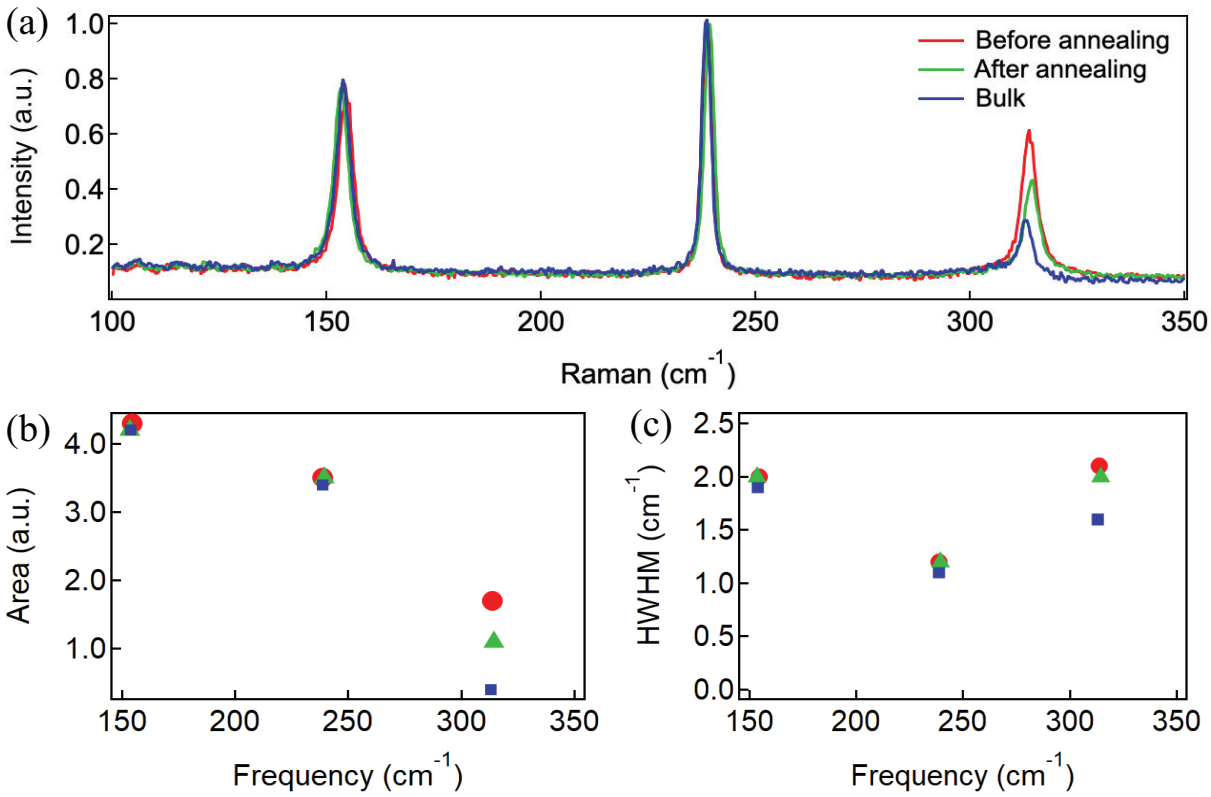

Figure 2.6: (a) Raman spectroscopy of a reference flake, red, compared to two annealed devices, green and blue. The peaks are normalized with respect to tallest peak of ZrSiSe, 238.26 cm^{-1}. (b) fitted area and (c) Half width at half maximum of ZrSiSe peaks in (a) obtained from a Lorentzian distribution

and 314 cm^{-1} is larger before annealing than after, and after annealing, the area under these peaks becomes more similar to those observed in the bulk spectrum.

2.4 Discussion

Liu *et al.* have argued that current annealing ZrSiSe devices improves contact resistance by breaking down an amorphous oxide layer between the metal contact and crystalline ZrSiSe [17]. Our observation of dramatically improved contact resistance is consistent with this interpretation. Additionally, the quantum oscillation frequency of 215 T for annealed flakes matching that of bulk crystals (Fig.2.4d) and nearly identical Raman spectra before and after annealing (Fig.2.6) indicate that the Fermi surface area, phonon modes, and polarizability of

ZrSiSe remain relatively unaffected by the current annealing process. These results are also consistent with contact resistance improvement by this mechanism.

However, we also observed a significant reduction in resistivity following current annealing (Fig. 2.2b, Fig. 2.2d and Fig. 2.3), which is unlikely be explained by breakdown of amorphous oxide in the contact region alone. Wang *et al.* showed that the underlying process of current annealing of suspended graphene is thermal [16]. We argue that a similar thermal process could be responsible for improving the mobility of TSMs based on our comparison of current-annealed devices with and without pre-treatment by vacuum annealing. First, we found that pre-treated, vacuum-annealed devices subsequently annealed at a lower current density, Fig. 2.2b, compared to devices that were not pre-treated, Fig.2.11. Second, vacuum-annealed devices were observed to current anneal in one step while devices without pre-treatment annealed in a more complex fashion as a function of current bias. Although a pre-treatment by vacuum annealing improved the quality of our devices, complete annealing in this way could not be achieved because devices degraded visually at temperatures higher than 500 °C for ZrSiSe, Fig.2.12. We speculate that current annealing can be more effective than vacuum annealing because of heating of defect sites and barriers that serve as local hot spots, and future work involving local probes would be needed to definitively establish this mechanism [24].

2.5 Conclusion

A current annealing technique can be generalized to 2D TSMs as an effective method to obtain high mobility in devices that are degraded by the exfoliation process and/or fabrication procedures. Both contact resistance and resistivity in the TSMs studied improved with current annealing, likely due to a combination of breakdown of surface oxide and local, current-induced heating. Current annealing is a simple, fast and *in situ* process that we have found to be more successful than thermal annealing alone to improve device quality. Current annealing recovers the high mobility of TSMs in the thin flake limit and enables

the observation of quantum oscillations at low magnetic field, which opens the door to investigations of their properties in two-dimensional form, the effect of external electric fields, and new topological phenomena in heterostructures with other layered materials.

2.6 Supplementary Materials

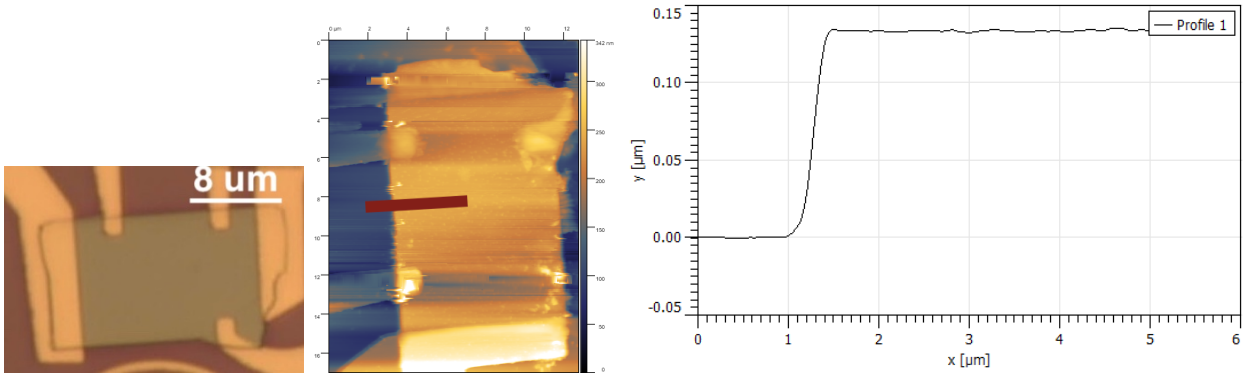

(a)

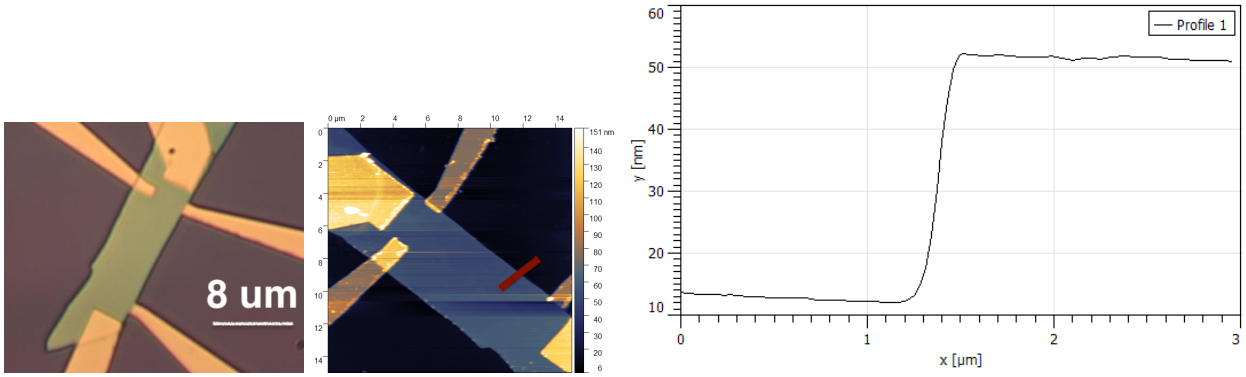

(b)

Figure 2.7: (a) Device ZSS-A and corresponding AFM data. The thickness of the flake is 130 nm, length and width are both 8 μm. (b) Device ZSS-B, the thickness is 40 nm, the width is 3 μm and the length is 9 μm.

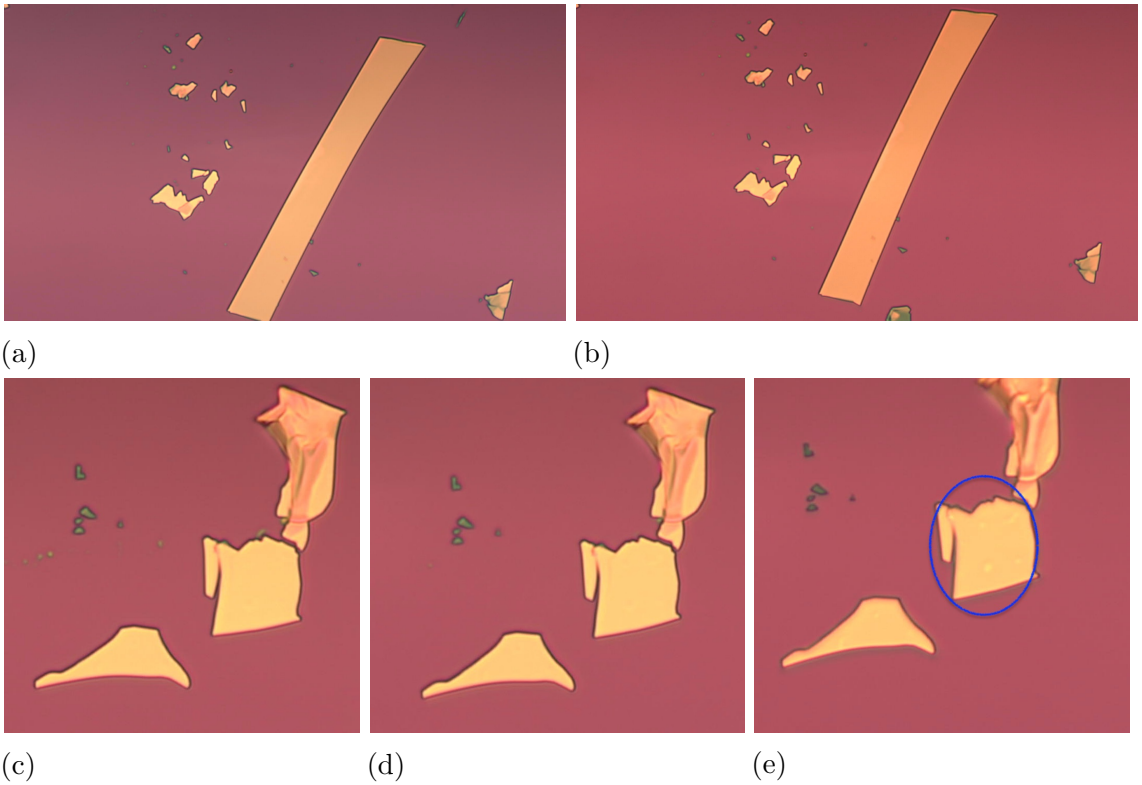

Figure 2.8: Degradation of ZrSiSe is very slow in air. A freshly exfoliated ZrSiSe flake is exposed to Air, (a) is the pre-exposure and (b) is the post exposure after 24 hours, no oxidation is observed. In an attempt to oxidize a fresh ZrSiSe flake, (c), using O_2 plasma no oxidation is observable after 1 min of process at 200 mbar and 75 W, (d), after extra 10 min of process with the same parameters the flake barely degrades inside the indicated blue circle of (e).

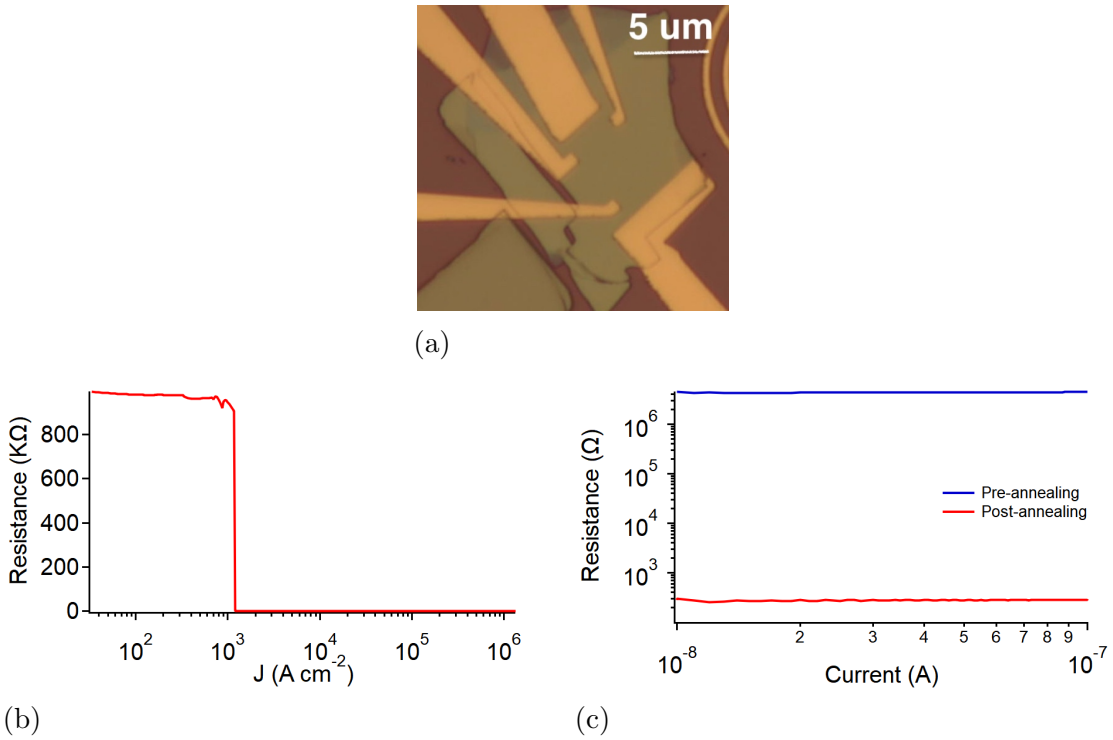

Figure 2.9: Annealing device ZSS-D, a top contacted thermally treated device. (a) is the micrograph of the device and (b) is the resistance as a function of current density. Resistance of the device is compared pre-annealing with post-annealing in (c).

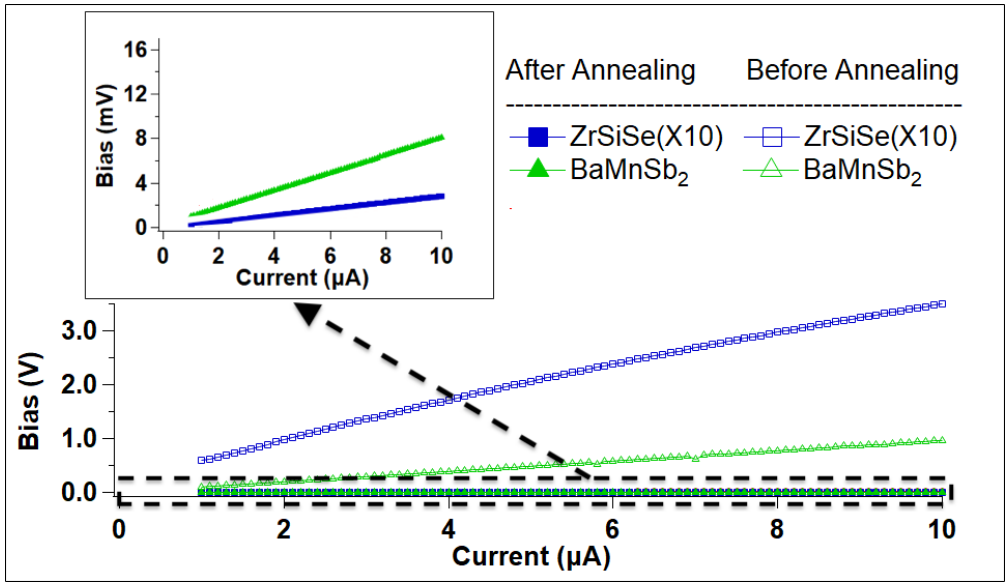

Figure 2.10: Comparison of V-I curves for ZSS-B and $BaMnSb_2$ pre-annealing with post-annealing. These measurements are AC current biased measurement. Slope of lines, two point resistance, shows significant decrease of two point resistance after current annealing.

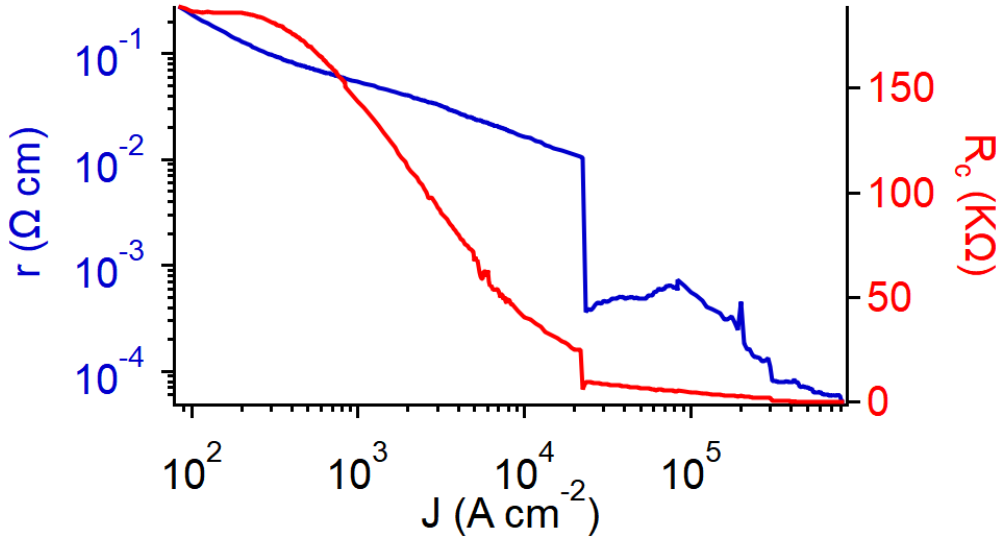

Figure 2.11: Resistivity (contact resistance) of device ZSS-B as a function of current density displayed on left (right) axis and colored blue (red).

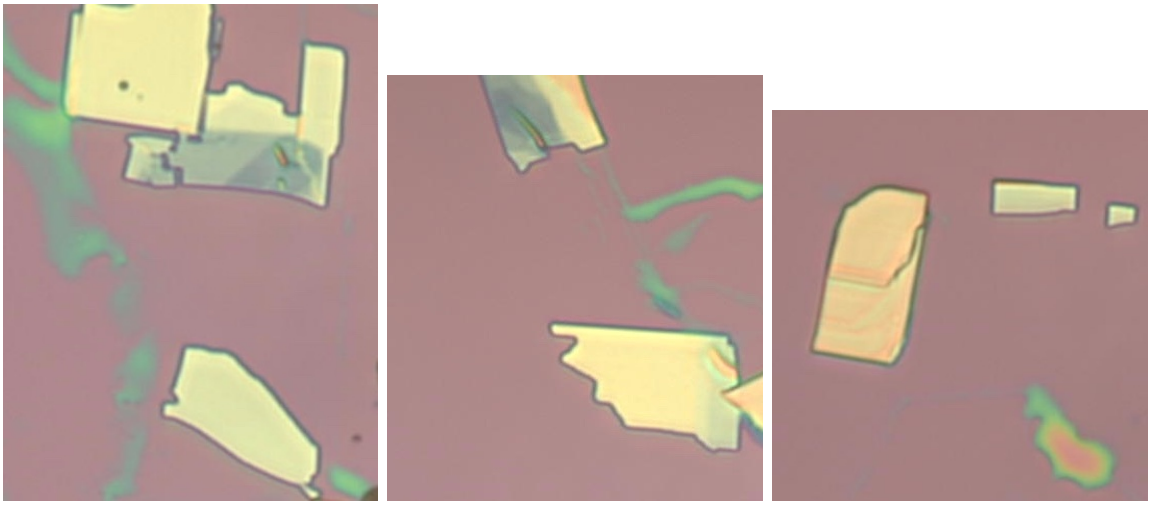

(a)

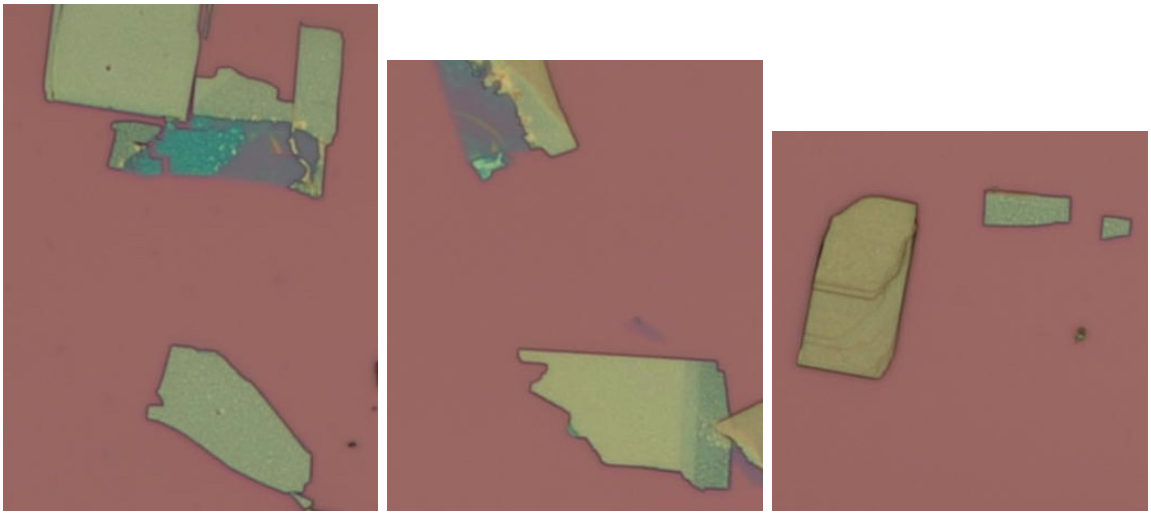

(b)

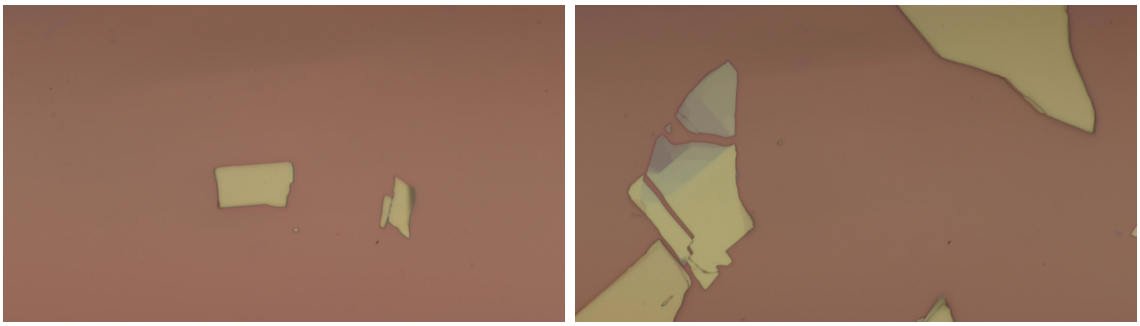

(c)

Figure 2.12: Comparison of thermally treated ZrSiSe before, (a), and after, (b), treatment for 2 hours in vacuum at 600 °C. Visual signs of degradation appear at 600 °C. In contrast flakes that are thermally treated for 2 hours in vacuum at 500 °C show no sign of degradation (c), indicating the limit of thermal treatment for 2D ZrSiSe is approximately 500 °C.

(a)

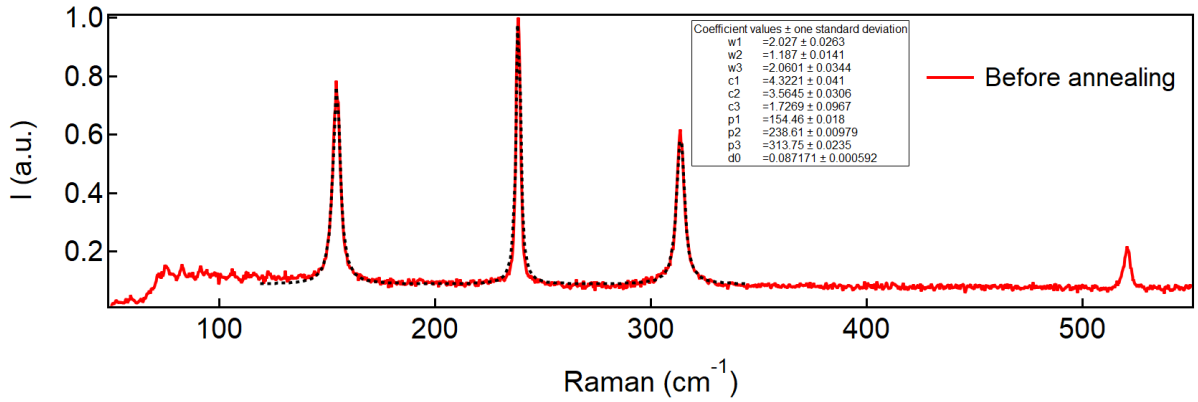

(b)

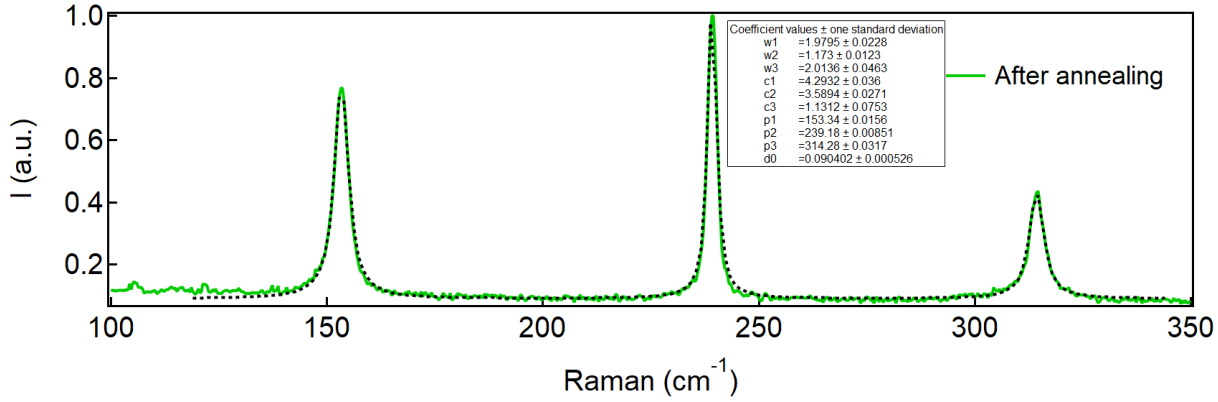

(c)

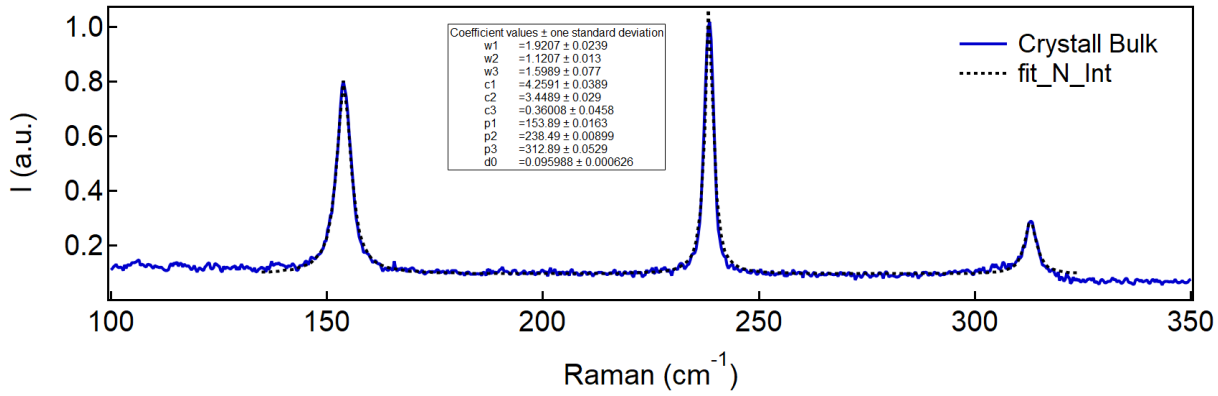

Figure 2.13: Lorentzian fits (black dashed lines) to the Raman spectrum of ZrSiSe (a) before annealing, (b) after annealing, and (c) a freshly cleaved bulk sample. Fitting parameters: W is the half width at half maximum, C is the area under the curve, P is the mode frequency, and d is the vertical offset. Indices 1 to 3 indicate the peaks from left to right, 154 cm^{-}1, 238 cm^{-}1, and 313 cm^{-}1 respectively.

References

[1] NP Armitage, EJ Mele, and Ashvin Vishwanath. Weyl and dirac semimetals in three-dimensional solids. *Reviews of Modern Physics*, 90(1):015001, 2018.

[2] Andrei Bernevig, Hongming Weng, Zhong Fang, and Xi Dai. Recent progress in the study of topological semimetals. *Journal of the Physical Society of Japan*, 87(4):041001, 2018.

[3] Jin Hu, Su-Yang Xu, Ni Ni, and Zhiqiang Mao. Transport of topological semimetals. *Annual Review of Materials Research*, 49:207–252, 2019.

[4] Junchao Ma, Ke Deng, Lu Zheng, Sanfeng Wu, Zheng Liu, Shuyun Zhou, and Dong Sun. Experimental progress on layered topological semimetals. *2D Materials*, 6(3):032001, 2019.

[5] Qiunan Xu, Zhida Song, Simin Nie, Hongming Weng, Zhong Fang, and Xi Dai. Two-dimensional oxide topological insulator with iron-pnictide superconductor lifeas structure. *Physical Review B*, 92(20):205310, 2015.

[6] Leslie M Schoop, Mazhar N Ali, Carola Straßer, Andreas Topp, Andrei Varykhalov, Dmitry Marchenko, Viola Duppel, Stuart SP Parkin, Bettina V Lotsch, and Christian R Ast. Dirac cone protected by non-symmorphic symmetry and three-dimensional dirac line node in zrsis. *Nature communications*, 7(1):1–7, 2016.

[7] Jin Hu, Zhijie Tang, Jinyu Liu, Xue Liu, Yanglin Zhu, David Graf, Kevin Myhro, Son Tran, Chun Ning Lau, Jiang Wei, et al. Evidence of topological nodal-line fermions in ZrSiSe and ZrSiTe. *Physical review letters*, 117(1):016602, 2016.

[8] Jinyu Liu, Jin Hu, Huibo Cao, Yanglin Zhu, Alyssa Chuang, D Graf, DJ Adams, SMA Radmanesh, L Spinu, I Chiorescu, et al. Nearly massless Dirac fermions hosted by Sb square net in $BaMnSb_2$. *Scientific reports*, 6(1):1–9, 2016.

[9] Anh Pham and Panchapakesan Ganesh. Quantum material topology via defect engineering. *Physical Review B*, 100(24):241110, 2019.

[10] Lukas Muechler, Wei Hu, Lin Lin, Chao Yang, and Roberto Car. Influence of point defects on the electronic and topological properties of monolayer WTe_2. *Physical Review B*, 102(4):041103, 2020.

[11] Masa Ishigami, JH Chen, WG Cullen, MS Fuhrer, and ED Williams. Atomic structure of graphene on SiO_2. *Nano letters*, 7(6):1643–1648, 2007.

[12] Sunghun Lee, Sanghyun Ji, Jinsu Kim, Sonny H Rhim, Soon Cheol Hong, Yun Chang Park, Young Haeng Lee, Dae Keun Park, Takeshi Toyama, Jiyeong Gu, et al. Ferromagnetism in β-Ag_2Se topological semimetal. *Journal of Alloys and Compounds*, page 162025, 2021.

[13] Yequan Chen, Yongda Chen, Jiai Ning, Liming Chen, Wenzhuo Zhuang, Liang He, Rong Zhang, Yongbing Xu, and Xuefeng Wang. Observation of Shubnikov-de Haas oscillations in large-scale Weyl semimetal WTe_2 films. *Chinese Physics Letters*, 37(1):017104, 2020.

[14] RK Shama, Goutam Sheet, and Yogesh Singh. 2D weak anti-localization in thin films of the topological semimetal PdBiS. *Scientific Reports*, 11, 2021.

[15] Kirill I Bolotin, Kenneth J Sikes, J Hone, HL Stormer, and Ph Kim. Temperature-dependent transport in suspended graphene. *Physical review letters*, 101(9):096802, 2008.

[16] Haidong Wang, Xing Zhang, and Hiroshi Takamatsu. Ultraclean suspended monolayer graphene achieved by in situ current annealing. *Nanotechnology*, 28(4):045706, 2016.

[17] Xue Liu, Chunlei Yue, Sergey V Erohin, Yanglin Zhu, Abin Joshy, Jinyu Liu, Ana M Sanchez, David Graf, Pavel B Sorokin, Zhiqiang Mao, et al. Quantum transport of the 2d surface state in a nonsymmorphic semimetal. *Nano letters*, 21(11):4887–4893, 2021.

[18] Josh P Thompson, M Hasan Doha, Peter Murphy, Jin Hu, and HO Churchill. Exfoliation and analysis of large-area, air-sensitive two-dimensional materials. *Journal of visualized experiments*, 143, 2019.

[19] Xueqiu You, Na Liu, Cheol Jin Lee, and James Jungho Pak. An electrochemical route to mos2 nanosheets for device applications. *Materials Letters*, 121:31–35, 2014.

[20] Lei Wang, I Meric, PY Huang, Q Gao, Y Gao, H Tran, T Taniguchi, Kenji Watanabe, LM Campos, DA Muller, et al. One-dimensional electrical contact to a two-dimensional material. *Science*, 342(6158):614–617, 2013.

[21] Yuli V Nazarov and Yaroslav M Blanter. *Quantum transport: introduction to nanoscience*. Cambridge university press, 2009.

[22] Jin Hu, JY Liu, David Graf, SMA Radmanesh, DJ Adams, Alyssa Chuang, Yu Wang, Irinel Chiorescu, Jiang Wei, Leonard Spinu, et al. π berry phase and zeeman splitting of weyl semimetal tap. *Scientific reports*, 6(1):1–8, 2016.

[23] Xiaochun Huang, Lingxiao Zhao, Yujia Long, Peipei Wang, Dong Chen, Zhanhai Yang, Hui Liang, Mianqi Xue, Hongming Weng, Zhong Fang, et al. Observation of the chiral-anomaly-induced negative magnetoresistance in 3D Weyl semimetal TaAs. *Physical Review X*, 5(3):031023, 2015.

[24] Myung-Ho Bae, Zhun-Yong Ong, David Estrada, and Eric Pop. Imaging, simulation, and electrostatic control of power dissipation in graphene devices. *Nano letters*, 10(12):4787–4793, 2010.

Chapter 3

Transport Evidence of Weyl Orbit in Dirac Semimetal ZrSiSe

The interaction of carriers with the crystal lattice might lead to imitating the relativistic dynamic of high-energy particle physics. Such interaction may create non-trivial topological surface quantum states with anomalous electromagnetic properties. Weyl semimetals and their symmetry-protected analogs, Dirac semimetals, are topological materials hosting such states. Symmetry-protected Dirac semimetals show linear dispersion described by two copies of Weyl equations; at the surface of a crystal, the broken translation symmetry creates topological surface states called Fermi arcs. These Fermi arcs result in a cyclotron motion known as Weyl orbits that connect Fermi arcs on top and bottom surfaces through the chiral bulk states. The signature of such Fermi arc orbit is apparent in Shubnikov-de Haas oscillations [1]. Fast Fourier Transform of Shubnikov-de Haas oscillations in thin flakes of ZrSiSe, a nonsymmorphic Dirac semimetal, reveals the unexpected frequency of 140 T not related to any known surface (450 T) or bulk (220 T) Fermi surface. We show that this frequency has a 2D nature by providing angle dependence and thickness dependence of quantum oscillations. Angle dependence of 140 T follows $cos^{-1}(\theta)$, in contrast to bulk frequency, 220 T, which shows no change with angle. In addition, thickness dependence shows that the relative amplitude of 140 T to 220 T exponentially increases by decreasing the thickness. In addition, we provide a comparison of phase analysis of 140 T with 220 T that shows the different origins of these frequencies. We speculate this 140 T frequency can be of Weyl orbit oscillations and extract a Fermi arc with a length of 0.08 $\mathring{A}^{-1}$ in ZrSiSe. Further theoretical studies and experiments are required to test this interpretation.

3.1 Introduction

The relativistic dispersion in energy eigenvalues for mass-less spin half particles is described by the Weyl equation 1.8. Weyl nodes with opposite chirality act as monopoles or anti-monopoles

of Berry curvature; that is, a closed surface around a node passes $\pm 2\pi$ of Berry flux 1.1.1. Projection of Weyl nodes on the surface of these materials imposes surface states, the so-called Fermi arcs; these states connect those projections in momentum space. The Fermi arc directly results from bulk-surface correspondence and cannot be removed without annihilating the bulk Weyl nodes. Transport evidence of the Fermi arc is evident in the quantum oscillations from the Weyl orbit, where carriers traverse the Fermi arc on the top surface, penetrate the slab using bulk chiral modes to the bottom surface, and follow a similar path but in the opposite direction to the top surface 1.3. In Dirac semimetals, two Fermi arcs with opposite Berry flux meet at a sharp kink at the projection of Dirac nodes on the surface; hence the Weyl orbit is extended to Dirac semimetals. Such orbit leads to quantum oscillations, periodic in B^{-1}, and a phase-dependent on slab thickness 1.3.

The Weyl orbit was predicted [2] and experimentally observed by several groups [1, 3] in Cd_3As_2. Moll et al. [1] reported oscillations in Cd_3As_2 microstructures of thickness smaller than the mean free path, at magnetic fields smaller than 14 T. These oscillations consist of two frequencies, the bulk frequency of 36.5 T and a frequency of 61.5 T that originates in the Weyl orbit. They supported their claim by demonstrating the surface-like behavior of 61.5 T frequency and comparing oscillations in triangular and rectangular microstructures. Coherent Weyl orbits in rectangular sample results in a sharp oscillation peak at 61.5 T, in contrast to triangular samples with incoherent orbits where 61.5 T is absent. Further studies revealed quantum Hall effects at high magnetic field and low carrier concentrations of microstructures of Cd_3As_2[4], these studies used various methods such as Zn doping and electrostatic gate effects [5, 6].

Although Weyl orbits have been predicted in various materials, it has been experimentally observed only in Cd_3As_2 to our knowledge. Here we provide pieces of evidence that ZrSiSe might host Weyl orbits. ZrSiX (X=S,Se,Te) are Dirac semimetals that host Dirac nodal line and multiple Dirac nodes [7, 8]. They belong to tetragonal *P4/nmm* space group [9], which

is quite similar to Cd_3As_2 space group, tetragonal $P4_2/nmc$ [10]. In ZrSiX, nonsymmorphic symmetry protects the Dirac node at special K points, such as X point [7], hence these symmetry-protected Dirac points can be interpreted as two copies of Weyl nodes on top of each other. The symmetry protection is crucial because two Weyl nodes with opposite chirality may annihilate each other if they overlap in momentum space unless the band crossing is enforced by symmetry [11] or other rare situations [12]. These special symmetry-protected K points usually appear at the Brillouin zone boundary of nonsymmorphic space groups. However, this condition can be relaxed to any doubly degenerate bands with distinct 2D representations and protected band crossing by crystal symmetry [10]. Wang et al. reported such protected Dirac nodes along high symmetry lines in Cd_3As_2 [10] and Na_3Bi [13]. In addition, Bian et al. reported that the degenerate Dirac points at X in ZrSiTe evolve into the pairs of Weyl nodes with magnetic doping [14]. This suggests that the possibility of Fermi arc existing in this family of materials is high.

The additional quantum oscillation frequency of 140 T in ZrSiSe flakes is not attributed to any known Fermi pocket, even though the band structure of ZrSiX has been intensively studied [7, 15–17]. This oscillation might relate to Weyl orbits rather than conventional Fermi pockets. Considering the latter point and similarities mentioned above between ZrSiX and Cd_3As_2, we hypothesized that 140 T oscillation might root in Weyl orbits. Angle and thickness dependence experiments examined this hypothesis in flakes thinner than the mean free path.

3.2 Experimental Methods

We fabricated Hall bar devices on ZrSiSe in top- and bottom-contacted geometries. Schematic and pictures of fabricated Hall bar devices are shown in Fig.3.1a. Top-contacted devices were fabricated by exfoliation of ZrSiSe crystals inside a nitrogen glovebox (H_2O, $O_2 < 0.5$ ppm) on high-resistivity Si substrates (>10,000 Ω·cm) with 300 nm of thermal oxide treated by O_2 plasma at 200 mbar oxygen pressure and 75 W power for 60 seconds. Flakes with

proper thickness were first identified by optical microscopy using a hermetic cell with optical access[18], and then thickness was measured using atomic force microscopy (Fig. S1 in the Supplementary Materials of chapter 2). To pattern Hall bar contacts on the flakes, PMMA C4 resist was spun on the chip in air and baked at 180 °C inside the glovebox, followed by electron beam lithography. PMMA dissolved in chlorobenzene was used because the more commonly used anisole-based resists were found to degrade the quality of ZrSiSe samples. 3/120 nm Cr/Au contacts were thermally evaporated, Fig.3.1a. The total air exposure in this process was limited to less than 5 minutes to minimize degradation of ZrSiSe (Fig. S2 of the Supplementary Material).

Bottom-contacted devices were prepared, starting with electron beam lithography to pattern 2/20 nm Cr/Au Hall bar contacts. To facilitate thin flake exfoliation of ZrSiSe, we mechanically exfoliated the crystals inside the glove box on an HF treated Si substrates with 90 nm of thermal oxide. Thin flakes were identified in the hermetic inspection cell and transferred onto the contacts using a dry transfer method involving PDMS and PPC [19] inside the glove box, Fig.3.1a. Devices were current annealed at room temperature and pressure to improve the contact resistance. Current up to 4 mA was passed through contact pairs. Magnetoresistance, Hall resistivity, and quantum oscillations were measured at 4 K using a constant current source and standard lock-in techniques.

Standard Finite Impulse Response (FIR) digital filters provided in Igor Pro were used to isolate the oscillation frequency in question. The sampling frequency matches the number of points on the wave, and the total number of filtering coefficients is at least 10 percent of the sampling frequency. Low pass FIR, high pass FIR, with a window of ± 10 T is used to separate oscillatory components.

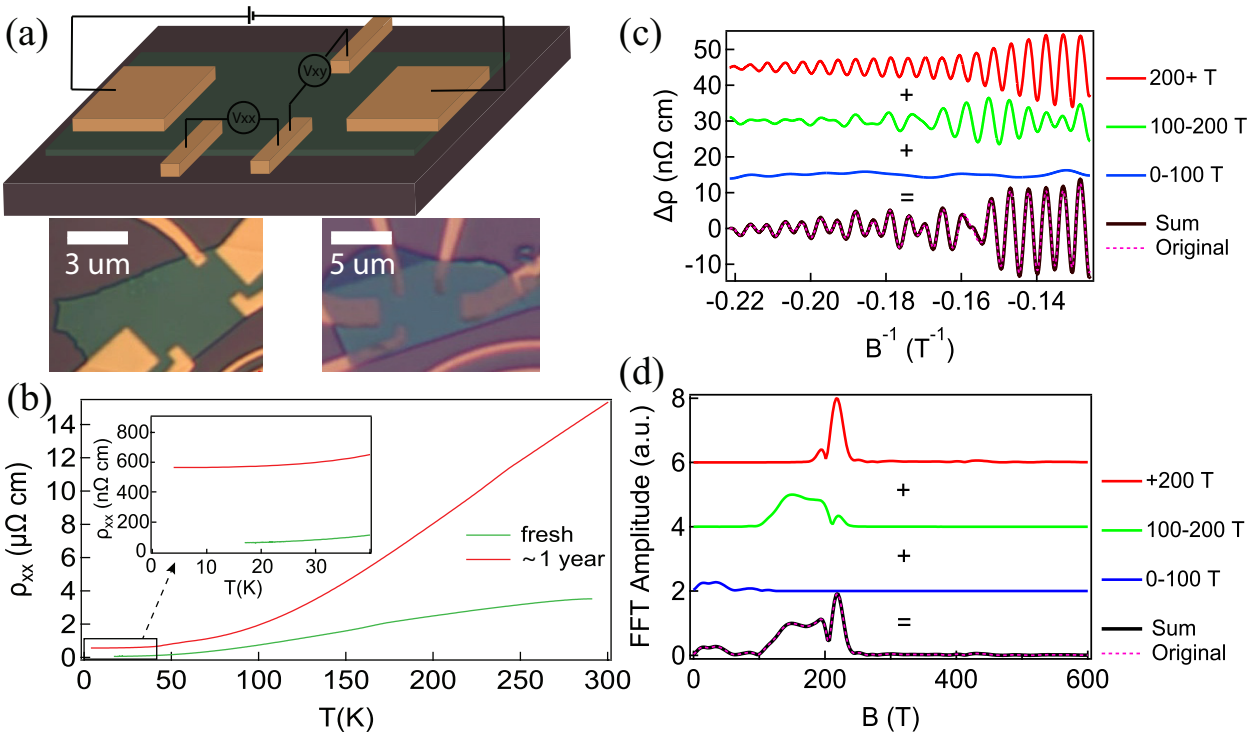

Figure 3.1: (a) Schematic and optical micrograph of thin ZrSiSe devices in top- and bottom-contact configurations. (b) Comparison of longitudinal resistivity of device B fresh after fabrication with after one year in the glovebox. The residual resistivity changes from 40 $n\Omega\ cm$ to 600 $n\Omega\ cm$. (c) Decomposition of quantum oscillation in longitudinal resistivity of device B to its oscillatory components using Finite Impulse Response digital filter. The summation of the oscillatory components adds up to the original oscillations. (d) The frequency spectrum of oscillations in panel (c). Each oscillatory component's summation of oscillation frequencies adds to the original FFT.

3.3 Results

We extracted the longitudinal resistivity of each device as $\rho_{xx} = (V_{xx}/I) \cdot (wL/l_{in})$, and transverse resistivity as $\rho_{xy} = (V_{xy}/I) \cdot (wL/l_{in})$ where w is the width of the sample, L is the thickness, and l_{in} is the length between the inner voltage probes. Residual resistivity, ρ_0, of fresh devices display small values of a few hundred $n\Omega\ cm$, depending on the age of the device and air exposure which tends to degrade or oxidize the samples [17]. The residual resistivity of a device can increase by almost one order of magnitude over the course of one year. Fig.3.1b shows the residual resistivity of a 52 nm flake changes from ∼0.04 to ∼0.6

$\mu\Omega\ cm$ over a year. A complete degradation can happen in a timeline that depends on the thickness of the flake; our observation suggests that a good device with a thickness of almost 100 nm will last 6-8 weeks in the glovebox before signs of degradation occur in resistivity. This time frame is used for measurements reported hereafter, ensuring the degradation has minimal effect on measurements. Residual resistivity of ZrSiSe is comparable to those of the high-quality Cd_3As_2 single crystals [20].

The magnetoresistance at temperatures below 30 K displays pronounced quantum oscillation in both longitudinal and transverse resistivity with a dominant oscillation frequency of 220 T, compatible with previously reported oscillation frequency for bulk devices in literature [8], arising from three-dimensional Fermi surface which is in agreement with ARPES measurements [7, 16]. In contrast to the bulk frequency, the expected frequency of 450 T, corresponding to the surface state [21], was not observed due to the low magnetic field range available for these experiments. We report the additional quantum oscillation frequency of ~ 140 T in fresh devices thinner than the mean free path of electrons in ZrSiSe, $l \approx 4\mu m$. The oscillatory components of longitudinal resistivity in device B are decomposed into three parts using low-pass and high-pass FIR filter described in Sec. 3.2 as shown in Fig. 3.1. The oscillatory components are analyzed with Fast Fourier transform, and the FFT amplitude spectrum is obtained. The summation of the FFT amplitude of the oscillatory components adds up to the original FFT amplitude.

The dependence of Shubnikov de Haas oscillation on the angle between the ab plane normal and the magnetic field suggest the signature of surface states for the 140 T frequency, as shown in Fig. 3.2. Here 0° denotes the magnetic field is out-of-plane and 90° in-plane. The angular dependence of the 220 T frequency is different than of the 140 T frequency, Fig. 3.2c, the 220 T frequency remains constant over various angles while the 140 T frequency increases as the field gets parallel to the surface, showing a $\cos^{-1}(\theta)$ angle dependence. Such angle dependence is the hallmark of 2D Fermi surfaces. The band structure of ZrSiSe and ARPES

data does not show any Fermi surface corresponding to this oscillation frequency. Although our measurements suggest a 2D Fermi surface, more data points might be required to confirm this claim unambiguously. Technical problems with our measurement setup, no access to a high magnetic field, and time limit prevent us from acquiring sufficient data points at this stage.

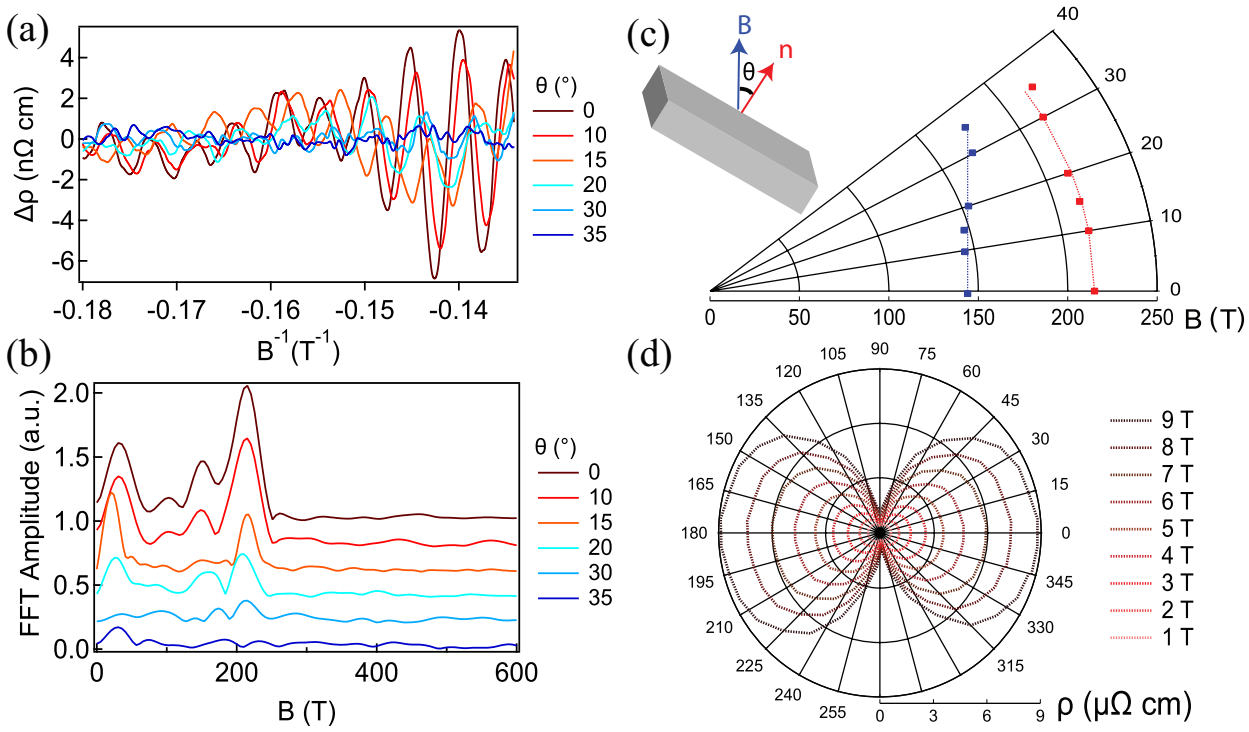

Figure 3.2: (a) Angle dependence of quantum oscillation in longitudinal resistivity measured in device A. (b) The frequency spectra obtained from Fast Fourier Transform of oscillations represented in (a), FFT amplitude of both 220 T and 140 T shrink with increasing the angle. The frequency of 220 T almost remains the same while the 140 T red shift with increasing the angle. (c) The red shift in 140 T follows $\cos^{-1}(\theta)$ dependence, suggesting a 2D Fermi surface. (d) Polar plot of longitudinal resistivity in device B at 4 K, the current is perpendicular to the axis of rotation. The resistivity shows a two-fold symmetric dumbbell shape behavior at available magnetic fields up to 9 T.

In contrast to the polar plot of magnetoresistance in bulk samples that show a four-fold symmetric butterfly shape with the maximum of magnetoresistance at 45° [8, 22] at fields as low as 1 T [23], the polar plot of magnetoresistance in thin flakes shows a two-fold symmetric dumbbell shape behavior with the maximum of longitudinal resistivity corresponds to fields

perpendicular to the sample surface as shown in Fig.3.2d. Further examples of other devices showing dumbbell shape magnetoresistance are provided in appendix B.

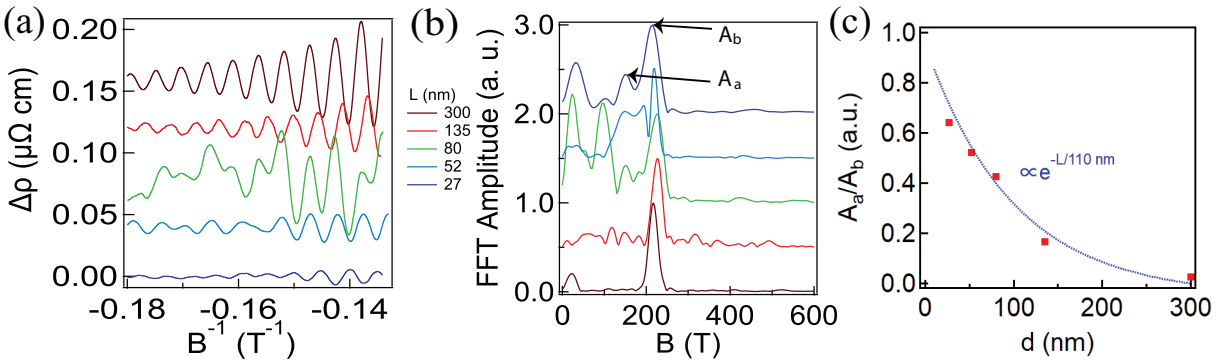

Figure 3.3: (a) Thickness dependence of longitudinal quantum oscillations for field perpendicular to the surface at 4 K. (b) Raw frequency spectra from Fast Fourier Transform of quantum oscillations that are represented in (a), The Weyl orbit frequency 140 T is not observable for samples thicker than 300 nm without further analysis. The bulk frequency of 220 T is more dominant in thicker flakes; as the thickness decreases, the Weyl orbit frequency appears stronger than the bulk frequency. (c) Relative FFT amplitude of Weyl orbit compared to bulk oscillation obtained from panel (b), the relative amplitude decrease exponentially as the thickness increase.

Next, quantum oscillations in longitudinal resistivity for various thicknesses of flakes are measured at 4K for out-of-plane magnetic fields,$\theta = 0$, Fig.3.2a. Frequency spectra of oscillations in all samples are obtained using Fast Fourier Transform for fields of 4.5 T to 7.5 T, Fig.3.2b. The frequency of 140 T is observed in samples where the flake thickness is smaller than or comparable to the bulk mean free path. Because the Fast Fourier Transform range is chosen to be similar for all thicknesses of ZrSiSe, the FFT amplitude of oscillation frequency is a good variable for comparison between different thicknesses, Fig.3.2b, however a fair comparison of the oscillation amplitudes at 140 T requires normalization relative to the oscillation amplitude of 220 T. The relative amplitude of quantum oscillations is found to be thickness-dependent, Fig.3.3c, such that the Weyl orbit frequency 140 T is not observable for samples thicker than 300 nm without further analysis such as frequency filtering. As the thickness decreases, the potential Weyl orbit frequency appears stronger than the bulk frequency.

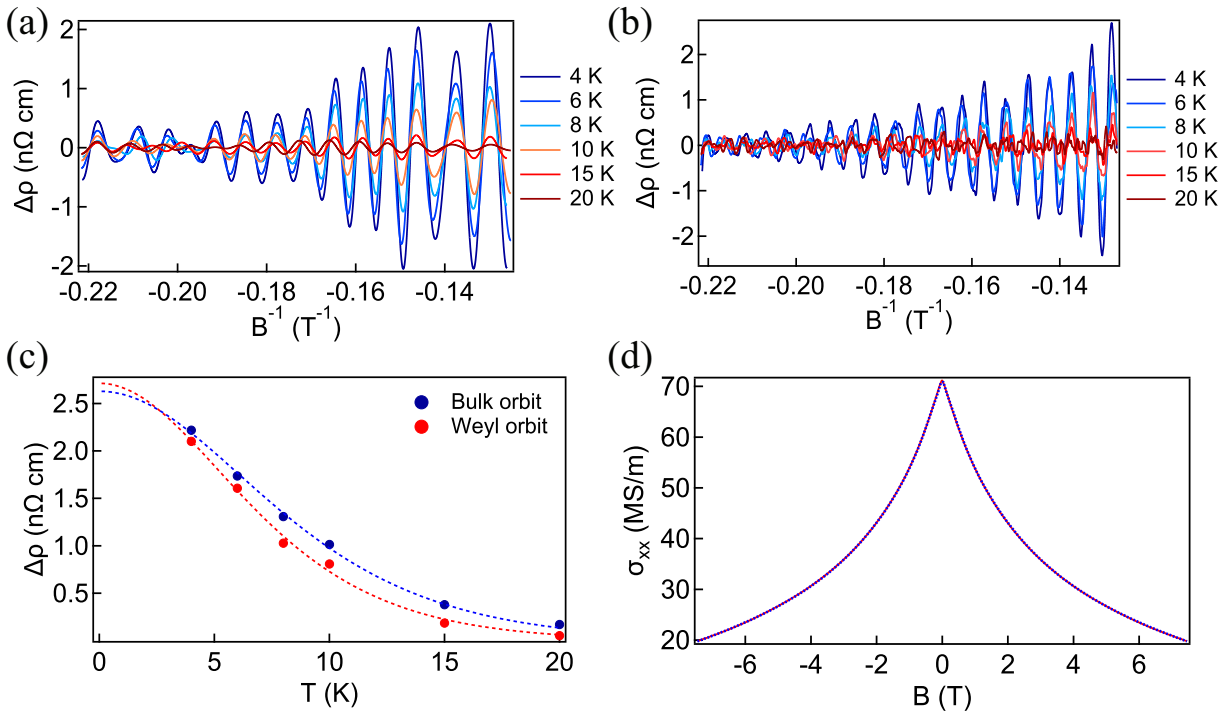

Figure 3.4: Temperature dependence of quantum oscillations of device A filtered using FIR digital filter for (a) a window of 120 T to 160 T corresponding to Weyl orbit, and (b) a high-pass filter with 200 T cut-off frequency, corresponding to bulk quantum oscillations. Temperature dependence of oscillations at $\sim$0.14 T^{-1} derived from oscillations in panels (a) and (b). The dotted lines correspond to the temperature dependence of Lifshitz-Kosevich formalism. (d) Extraction of carrier density and mobility from longitudinal conductivity, the solid red line is the longitudinal conductivity, and the dashed blue line is the two-band model fit to the data.

The increase in the amplitude of Weyl orbit frequency follows an exponential behavior with the fitting parameter of 110 nm. This value is the quantum phase coherence length in the material and is much less than the carriers' bulk mean free path [2]. Temperature dampening of quantum oscillations is used to obtain the effective mass, m*. Lifshitz-Kosevich formalism Eq. 1.2 describe this damping effect, the oscillation amplitudes changes as $A(T) = A_0 \frac{2\pi^2 K_b T}{\hbar\omega_c}$, where K_b is the Boltzman constant and $\Omega_c = \frac{eB}{m^*}$ is the cyclotron frequency. A high pass digital FIR filter with a cutoff range of 200 T for segregation of bulk frequency and a notch pass filter with the transition window of 120 T to 160 T is used to find the effective mass of each frequency individually, Fig. 3.4(a),(b). Quantum oscillations of each frequency at the

peak closest to 0.14 T^{-1} were extracted and plotted against temperature, Fig. 3.4(c). The Lifshitz-Kosevich fit to the data results in $m^*_{220} = 0.13m_e$ and $m^*_{140} = 0.17m_e$, where m_e is the rest mass of electron, and m^*_x is the effective mass of x frequency.

We obtained magnetoconductivity of device A by inverting the resistivity tensor $\sigma_{xx}(B) = \frac{\rho_{xx}(B)}{\rho^2_{xx}(B)+\rho^2_{xy}(B)}$, where $\rho_{xx}(B)$ is the longitudinal resistivity and $\rho_{xy}(B)$ is the transverse resistivity. To obtain the carrier density and mobility of device A, we fit the magnetoconductivity to a two-band model [24–26], $\sigma_{xx}(B) = \frac{1}{\rho_1+A_1B^2} + \frac{1}{\rho_2+A_2B^2}$ where $\rho_i = \frac{1}{n_i e\mu_i}$ and $A_i = \frac{\mu_i}{n_i e}$, with μ and n the mobility and carrier density, respectively. As shown in Fig. 3.4d, the two-band model yields a satisfactory fit (blue dashed lines) to the measured data (red solid line), from which the carrier densities and mobilities are extracted as $n_h = 2.9 \times 10^{20}\ \frac{1}{cm^3}$, $n_e = 5 \times 10^{19}\ \frac{1}{cm^3}$, $\mu_h = 3700\ \frac{cm^2}{V.S}$, and $\mu_e = 13400\ \frac{cm^2}{V.S}$.

The bulk mean free path of electrons is estimated from transport as $l = \frac{\hbar K_f}{ne^2\rho_0}$, where $K_f = \sqrt{2F_b e/\hbar} = 0.8\ nm^{-1}$, n is the electron density, and $\rho_0 = 1.4\ \mu\Omega.cm$ is the residual resistivity of device A at 4 K. This gives $l = 4\ \mu m$ which is comparable with the mean free path for Cd_3As_2, [1].

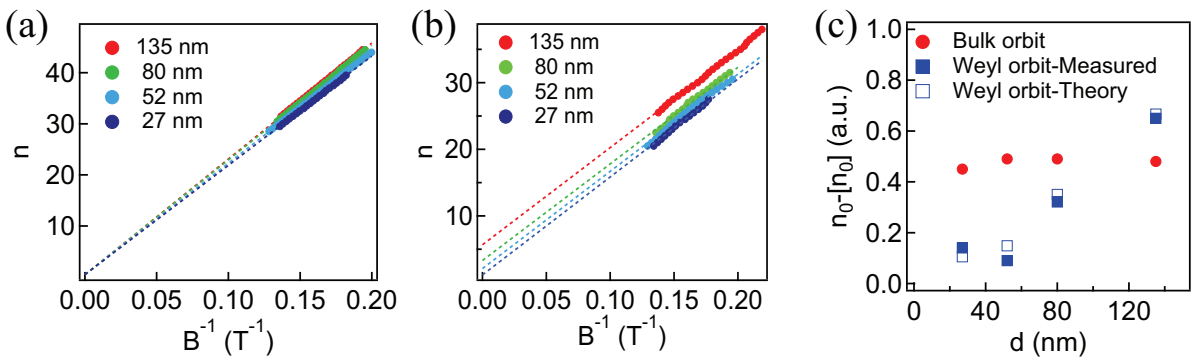

Figure 3.5: Landau level analysis of (a) bulk orbit and (b) Weyl orbit corresponding to oscillations in Fig. 3.3 at fields perpendicular to the current and 4 K for various thicknesses of material. (c), the fractional phase analysis of oscillations obtained from the Y-intercept in panels (a) and (b), the red-filled circle is the fractional phase of the bulk oscillation from (a), and the blue-filled square is the fractional phase of the Weyl orbit from (b). Blue empty square is the prediction by the theoretical model.

Next, we study the phase of quantum oscillations as a function of the inverse field because it can provide an additional clue to the origin of quantum oscillations. The oscillation of each device in Fig.3.3 is decomposed into the bulk oscillation and Weyl orbit components using FIR digital filters. Arbitrary integer Landau index, n, is assigned to the oscillation minimum, and half-integer, n+0.5, is assigned to the consecutive oscillation minimum. Landau index versus oscillation frequency was plotted, and a linear fit with the slope of oscillation frequency obtained from Fig. 3.3b is used to find the Y-intercept. Landau index was adjusted by integers such that the intercept falls between 0 and 1 for bulk oscillations, Fig.3.5a, and between $\lfloor n_0 \rfloor$ and $\lfloor n_0 \rfloor + 1$ for Weyl orbit, Fig. 3.5b, where $\lfloor n_0 \rfloor$ is the integer floor of intercept extracted from the Weyl orbit picture, 1.15. The fractional phase, $n_0 - \lfloor n_0 \rfloor$, in Fig. 3.5(c) for bulk oscillation, denoted by red-filled circles, show a constant value for various thickness of the material. In contrast, the fractional phase of the potential Weyl orbit is not constant and changes with material thickness. At higher fields, a deviation from linearity is observed, refer to Appendix B for more information, but our limited number of data points is insufficient to analyze the phase of quantum oscillations unambiguously.

3.4 Discussion

Pronounced quantum oscillation in magnetoresistance and low residual resistivity, such as $\rho_0 = 40\ n\Omega.cm$ in device B, signals high device quality and low effective mass of charge carriers in our devices. The air sensitivity of ZrSiSe requires cautious fabrication (to minimize the air exposure) and rapid measurements after fabrication (up to a few weeks). The resistivity of device B increased by more than an order of magnitude over the course of a year in the glovebox, and quantum oscillations significantly changed in this device. The study of Shubnikov de Haas oscillations in bulk crystals reported two frequencies, 220 T and 450 T, corresponding to bulk Fermi surface and a non-topological surface state respectively [27], additional frequency of 140 T is observed in fresh samples with their thickness smaller than mean free path of carriers, $l \sim 4\mu m$. The bulk quantum oscillation is much more robust in

samples thicker than 300 nm that washes out the 140 T frequency; hence digital filtering, such as FIR high pass and low pass filters, are required to detect these oscillations in thick samples. In contrast, no additional filtering is required to detect the 140 T oscillations in thin samples (less than 135 nm). In addition, digital filtering is essential to segregate the target carriers contributing to any specific frequency and study them unambiguously. We used the FIR digital filter and showed in Fig.3.1c and d that the summation of oscillatory components using our filtering technique is the same as the original wave; hence FIR filtering technique is accurate and can be used to study the target carriers unambiguously.

Although indirect pieces of evidence support the existence of a Fermi-arc in ZrSiSe, neither calculations nor experiments robustly confirm such a Fermi arc yet. As for the indirect evidence, first, the crystal structure of ZrSiSe belongs to tetragonal P_4/nmm space group [7] which is very similar to the space group of Cd_3As_2, tetragonal P_4/nmc. This similarity in underlying crystal symmetry can indicate a similar symmetry protection mechanism (further theoretical study is required to confirm this point), considering Cd_3As_2 is a Dirac semimetal that hosts Fermi arcs due to the symmetry protections at Dirac nodes, ZrSiSe with multiple Dirac points and a Dirac nodal line might also host Fermi arcs due to symmetry protections. Second, to picture a Dirac point equivalent to two copies of Weyl nodes with opposite chirality on top of each other, protection by nonsymmorphic symmetry is required. Two Weyl nodes with an opposite chirality at the same point in the momentum space can generally annihilate each other and open up a gap at the node unless nonsymmorphic symmetries protect that point in the momentum space. In ZrSiSe, the Dirac point at X is protected with nonsymmorphic symmetry [7], hence increasing the possibility of the existence of Fermi-arc in the vicinity of X. Third, the ARPES data of ZrSiSe suggest the existence of Dirac-like band crossing for a few-layer slab of ZrSiSe at $K_x = X \pm 0.032\mathring{A}^{-1}$ parallel to M-X-M. This band crossing is absent in bulk band structure but appears for the slab calculation of ZrSiSe [7]. These band crossings are in the vicinity of X; hence once they touch, they might be protected with nonsymmorphic symmetries and give rise to Fermi arcs. The angle dependence

of magnetoresistance further emphasizes the importance of calculating band crossing at the proper thickness. We observed two-fold symmetry in the polar plot of magnetoresistance of thin flakes, which is in contrast to the expected butterfly-shaped four-fold symmetry in bulk. The origin of the butterfly-shaped four-fold symmetry is still ambiguous [23, 28], this emphasizes the requirement of another approach toward band calculations in ZrSiSe, such as thickness-dependent band calculations. Such a theoretical model can shine a light on our conjecture for the existence of the Fermi arc in ZrSiSe.

Assuming that Weyl orbit is responsible for the 140 T frequency, from Eq. 1.15, $F_a = \frac{E_f K_0}{e\pi v_f}$, where K_0 is the length of Fermi arc, the average extracted K_0 is ~ 0.08 $\mathring{A}^{-1}$. The K space separation of suspected Dirac-like band crossing in the momentum space in ZrSiSe is at, $K_x = X \pm 0.032$ $\mathring{A}^{-1}$, which is similar to of Cd_3As_2 [13] for which the length of Fermi arc is also found to be ~ 0.08 $\mathring{A}^{-1}$.

Another evidence that $F_a = 137$ T corresponds to the Weyl orbit is in the 2D nature of this oscillation. Although our angle dependence of quantum oscillation frequency is not inclusive of a large number of angles, due to technical problems with the experimental setup, our limited data indicate $\cos^{-1}(\theta)$ behavior for oscillations of 140 T frequency while the 220 T remains constant over various angles. This 2D behavior of 140 T can arise from trivial surface states and topological surface states such as Weyl orbit, but the absence of any trivial Fermi pocket in the band structure corresponds to the frequency of 140 T might suggest the latter. A 2D behavior does satisfy one of the requirements for Weyl orbit, further indicating the possibility of Weyl orbit.

While the angle dependence of oscillation frequency at 140 T indicates a surface-like behavior, this frequency also displays pronounced bulk-dependent characteristics compatible with Weyl orbits. The 140 T is observable in samples thinner than the bulk mean free path, $l = 4\mu m$, and is more robust for thin samples. This is expected for the Weyl orbit as the carriers can coherently complete an orbit only when the orbit length is smaller than the mean free path.

In addition, various scattering processes can lead to quantum decoherence, so the quantum oscillation would decay exponentially in the orbit length, $2 \times l$, over quantum phase coherence length, l_Q, which is usually much shorter than the mean free path. The exponential fit to the relative amplitudes of quantum oscillation versus device thickness, L, suggests $l_Q = 220\ nm$, much shorter than $l = 4\mu m$. This is compatible with expectations. In addition to Weyl orbit, a trivial surface state can also give rise to a thickness dependence of relative amplitudes; the contribution of surface conduction channels in transport is heavier in thin flakes compared to the bulk. However, the thickness dependence of relative amplitude in such a mechanism is not exponential but inverse-linearly proportional to thickness. Although this exponential behavior further indicates that the underlying mechanism is of Weyl orbit.

Another piece of evidence for the origin of 140 T in Weyl orbits comes from the phase analysis of oscillations. The phase of quantum oscillations for the Weyl orbit depends on the thickness of the material and has thickness independent phase. The fractional phase, $n_0 - [n_0]$, of 220 T in Fig. 3.5 is almost constant for various thicknesses; in contrast, the fractional phase of 140 T is not constant; hence the origin of the latter oscillation frequency should be different from conventional Fermi pockets. The experimentally observed fractional phase for 140 T roughly matches that of the predictions for Weyl orbit, 1.15. The lack of large magnetic field data (small Landau levels) increases the uncertainty in our experimentally attained phase to the point that it is impossible to claim Weyl orbits as the origin of these oscillations unambiguously. We observed deviations from ideal periodicity in the inverse of magnetic field for 140 T frequency; refer to Appendix B for more details. This deviation can arise from band splitting in strongly spin-orbit coupled systems. This is compatible with our observation of weak anti-localization for thin samples; refer to appendix B for additional data. The lack of data points at high magnetic fields makes proper fitting and extraction of the g factor unreliable. Nevertheless, a linear fit to the data points with a fixed slope obtained from the frequency spectrum of oscillation is used to obtain a semi-reliable fractional phase.

3.5 Conclusion

Quantum oscillations in ZrSiSe thin flakes display an oscillation frequency of 140 T that has not been contributed to any conventional Fermi pocket. This frequency is not present in the bulk material; it appears in devices with thickness much less than the mean free path of an electron in ZrSiSe, $l \sim 4\mu m$. We presented pieces of evidence that this oscillation frequency might correspond to Weyl orbits. The angle dependence of 140 T displays a 2D Fermi surface, which is compatible with the expectation from Weyl orbits. We argue that the absence of a conventional 2D Fermi surface in the band structure of ZrSiSe that corresponds to this frequency can rule out the possibility of a topologically trivial surface state. Next, we show that the thickness dependence of oscillation amplitude matches an exponential behavior compatible with the Weyl orbit and contrasts with the linear behavior expected from the contribution of conventional surface states. In addition, we provided further evidence by analyzing the Landau level phase, though they do not unambiguously suggest Weyl orbits. Although we roughly show that the measured phase is consistent with the expectation of Weyl orbit, the uncertainty in our analysis is more significant than what is required to claim the origin of 140 T is Weyl orbit unambiguously. We conclude that ZrSiSe in thin limits might host Fermi arcs; although provided evidence is convincing, the uncertainty in the analysis is high due to lack of access to the high magnetic field, a gift of the COVID-19 pandemic. Measurements at high fields in tandem with thickness-dependent band calculations are required to conclude Weyl orbit in ZrSiSe unambiguously. We extracted the length of the Fermi arc in ZrSiSe to be $0.08\mathring{A}^{-1}$, possibly from the Dirac-like band crossings at $K_x = \pm 0.032\mathring{A}^{-1}$.

References

[1] Philip JW Moll, Nityan L Nair, Toni Helm, Andrew C Potter, Itamar Kimchi, Ashvin Vishwanath, and James G Analytis. Transport evidence for fermi-arc-mediated chirality transfer in the dirac semimetal cd3as2. *Nature*, 535(7611):266–270, 2016.

[2] Andrew C Potter, Itamar Kimchi, and Ashvin Vishwanath. Quantum oscillations from surface fermi arcs in weyl and dirac semimetals. *Nature communications*, 5(1):1–6, 2014.

[3] Guolin Zheng, Min Wu, Hongwei Zhang, Weiwei Chu, Wenshuai Gao, Jianwei Lu, Yuyan Han, Jiyong Yang, Haifeng Du, Wei Ning, et al. Recognition of fermi-arc states through the magnetoresistance quantum oscillations in dirac semimetal c d 3 a s 2 nanoplates. *Physical Review B*, 96(12):121407, 2017.

[4] Cheng Zhang, Yi Zhang, Xiang Yuan, Shiheng Lu, Jinglei Zhang, Awadhesh Narayan, Yanwen Liu, Huiqin Zhang, Zhuoliang Ni, Ran Liu, et al. Quantum hall effect based on weyl orbits in cd3as2. *Nature*, 565(7739):331–336, 2019.

[5] Shinichi Nishihaya, Masaki Uchida, Yusuke Nakazawa, Ryosuke Kurihara, Kazuto Akiba, Markus Kriener, Atsushi Miyake, Yasujiro Taguchi, Masashi Tokunaga, and Masashi Kawasaki. Quantized surface transport in topological dirac semimetal films. *Nature communications*, 10(1):1–7, 2019.

[6] Ben-Chuan Lin, Shuo Wang, Steffen Wiedmann, Jian-Ming Lu, Wen-Zhuang Zheng, Dapeng Yu, and Zhi-Min Liao. Observation of an odd-integer quantum hall effect from topological surface states in cd 3 as 2. *Physical Review Letters*, 122(3):036602, 2019.

[7] Leslie M Schoop, Mazhar N Ali, Carola Straßer, Andreas Topp, Andrei Varykhalov, Dmitry Marchenko, Viola Duppel, Stuart SP Parkin, Bettina V Lotsch, and Christian R Ast. Dirac cone protected by non-symmorphic symmetry and three-dimensional dirac line node in zrsis. *Nature communications*, 7(1):1–7, 2016.

[8] Jin Hu, Zhijie Tang, Jinyu Liu, Xue Liu, Yanglin Zhu, David Graf, Kevin Myhro, Son Tran, Chun Ning Lau, Jiang Wei, et al. Evidence of topological nodal-line fermions in ZrSiSe and ZrSiTe. *Physical review letters*, 117(1):016602, 2016.

[9] AJ Klein Haneveld and F Jellinek. Zirconium silicide and germanide chalcogenides preparation and crystal structures. *Recueil des Travaux Chimiques des Pays-Bas*, 83(8):776–783, 1964.

[10] Zhijun Wang, Hongming Weng, Quansheng Wu, Xi Dai, and Zhong Fang. Three-dimensional dirac semimetal and quantum transport in cd 3 as 2. *Physical Review B*, 88(12):125427, 2013.

[11] Steve M Young, Saad Zaheer, Jeffrey CY Teo, Charles L Kane, Eugene J Mele, and Andrew M Rappe. Dirac semimetal in three dimensions. *Physical review letters*, 108(14):140405, 2012.

[12] Shuichi Murakami. Phase transition between the quantum spin hall and insulator phases in 3d: emergence of a topological gapless phase. *New Journal of Physics*, 9(9):356, 2007.

[13] Zhijun Wang, Yan Sun, Xing-Qiu Chen, Cesare Franchini, Gang Xu, Hongming Weng, Xi Dai, and Zhong Fang. Dirac semimetal and topological phase transitions in a 3 bi (a= na, k, rb). *Physical Review B*, 85(19):195320, 2012.

[14] Qi Bian, Shaojian Li, Aiyun Luo, Zongyuan Zhang, Jin Hu, Yanglin Zhu, Zhibin Shao, Haigen Sun, Zhengwang Cheng, Zhiqiang Mao, et al. Visualizing discrete fermi surfaces

and possible nodal-line to weyl state evolution in zrsite. *npj Quantum Materials*, 7(1):1–8, 2022.

[15] Qiunan Xu, Zhida Song, Simin Nie, Hongming Weng, Zhong Fang, and Xi Dai. Two-dimensional oxide topological insulator with iron-pnictide superconductor lifeas structure. *Physical Review B*, 92(20):205310, 2015.

[16] M Mofazzel Hosen, Klauss Dimitri, Ilya Belopolski, Pablo Maldonado, Raman Sankar, Nagendra Dhakal, Gyanendra Dhakal, Taiason Cole, Peter M Oppeneer, Dariusz Kaczorowski, et al. Tunability of the topological nodal-line semimetal phase in zrsi x-type materials (x= s, se, te). *Physical Review B*, 95(16):161101, 2017.

[17] Danil W Boukhvalov, Raju Edla, Anna Cupolillo, Vito Fabio, Raman Sankar, Yanglin Zhu, Zhiqiang Mao, Jin Hu, Piero Torelli, Gennaro Chiarello, et al. Surface instability and chemical reactivity of zrsis and zrsise nodal-line semimetals. *Advanced Functional Materials*, 29(18):1900438, 2019.

[18] Josh P Thompson, M Hasan Doha, Peter Murphy, Jin Hu, and HO Churchill. Exfoliation and analysis of large-area, air-sensitive two-dimensional materials. *Journal of visualized experiments*, 143, 2019.

[19] Lei Wang, I Meric, PY Huang, Q Gao, Y Gao, H Tran, T Taniguchi, Kenji Watanabe, LM Campos, DA Muller, et al. One-dimensional electrical contact to a two-dimensional material. *Science*, 342(6158):614–617, 2013.

[20] Tian Liang, Jingjing Lin, Quinn Gibson, Satya Kushwaha, Minhao Liu, Wudi Wang, Hongyu Xiong, Jonathan A Sobota, Makoto Hashimoto, Patrick S Kirchmann, et al. Anomalous hall effect in $ZrTe_5$. *Nature Physics*, 14(5):451–455, 2018.

[21] Xue Liu, Chunlei Yue, Sergey V Erohin, Yanglin Zhu, Abin Joshy, Jinyu Liu, Ana M Sanchez, David Graf, Pavel B Sorokin, Zhiqiang Mao, et al. Quantum transport of the 2d surface state in a nonsymmorphic semimetal. *Nano letters*, 21(11):4887–4893, 2021.

[22] Haiyang Pan, Bingbing Tong, Jihai Yu, Jue Wang, Dongzhi Fu, Shuai Zhang, Bin Wu, Xiangang Wan, Chi Zhang, Xuefeng Wang, et al. Three-dimensional anisotropic magnetoresistance in the dirac node-line material zrsise. *Scientific reports*, 8(1):1–8, 2018.

[23] Mazhar N Ali, Leslie M Schoop, Chirag Garg, Judith M Lippmann, Erik Lara, Bettina Lotsch, and Stuart SP Parkin. Butterfly magnetoresistance, quasi-2d dirac fermi surface and topological phase transition in zrsis. *Science advances*, 2(12):e1601742, 2016.

[24] Jin Hu, JY Liu, David Graf, SMA Radmanesh, DJ Adams, Alyssa Chuang, Yu Wang, Irinel Chiorescu, Jiang Wei, Leonard Spinu, et al. π berry phase and zeeman splitting of weyl semimetal tap. *Scientific reports*, 6(1):1–8, 2016.

[25] Xiaochun Huang, Lingxiao Zhao, Yujia Long, Peipei Wang, Dong Chen, Zhanhai Yang, Hui Liang, Mianqi Xue, Hongming Weng, Zhong Fang, et al. Observation of the chiral-anomaly-induced negative magnetoresistance in 3D Weyl semimetal TaAs. *Physical Review X*, 5(3):031023, 2015.

[26] Jin Hu, Su-Yang Xu, Ni Ni, and Zhiqiang Mao. Transport of topological semimetals. *Annual Review of Materials Research*, 49:207–252, 2019.

[27] YJ Hu, Wing Chi Yu, Kwing To Lai, Dan Sun, FF Balakirev, Wei Zhang, JY Xie, KY Yip, EI Paredes Aulestia, Rajveer Jha, et al. Detection of Hole Pockets in the Candidate Type-II Weyl Semimetal $MoTe_2$ from Shubnikov–de Haas Quantum Oscillations. *Physical review letters*, 124(7):076402, 2020.

[28] Y-C Chiu, K-W Chen, Rico Schoenemann, VL Quito, S Sur, Q Zhou, D Graf, E Kampert, T Förster, K Yang, et al. Origin of the butterfly magnetoresistance in a dirac nodal-line system. *Physical Review B*, 100(12):125112, 2019.

Chapter 4

Electric-Field-Induced Effects in Dirac Semimetal ZrSiSe

The demand for high-performance and energy-efficient transistors ignited many studies on gate-induced topological phase transition in the last decade [1–3]. Gate-induced electrostatic field is a powerful tool to control Fermi level and break inversion symmetry in the target material because of its polar nature [4]. This provides a tunable platform to study topological physics and technologically sound advances such as gate-induced quantum information schemes. Here we study the effect of the electrostatic gate on ZrSiSe, a layered nodal line Dirac semimetal with multiple Dirac points in its band structure. We observed that the electrostatic gate increases the resistivity away from charge neutrality point $V_g = 0.8\ V$ at magnetic fields below $2\ T$. In contrast, the electrostatic gate reduces resistivity at fields above $2\ T$. In addition, we observed that gate voltage reduces the curvature of magnetoresistance. In addition, the amplitude of quantum oscillations reduces with an increase in gate voltage. The bulk frequency of quantum oscillations, $220\ T$, does not change with gate voltage, but the Weyl orbit frequency, $140\ T$, shows a quadratic blueshift with the gate voltage.

4.1 Introduction

The out-of-plane electric field has been used intensively to control physical properties such as carrier density and breaking inversion symmetry. Dual gated devices are commonly used to keep physical properties unchanged while breaking inversion symmetry. This symmetry breaking can open a band gap in Dirac materials such as bilayer graphene [5, 6]. Adjusting the electric field magnitude can tune the band gap of bilayer graphene to $250\ meV$ [7], paving the road for gate-induced low power dissipation devices. In addition, breaking inversion symmetry can give rise to many other exciting phenomenons such as electrically switchable Berry curvature dipole [8], tunable anomalous Hall effect [9] and valley dependent transport

[10] which depends on the anomalous velocity due to the cross product of electric field and Berry flux, Eq. 1.3.

Here we study the gate-induced effect on ZrSiSe, a Dirac nodal line topological semimetal with multiple Dirac nodes [11, 12]. The nodal line is protected by symmorphic symmetry and can gap out with spin-orbit coupling. This gap is calculated to be 36 meV, which is comparable to the maximum distance of the nodal line from the Fermi level [13]. In addition, this material hosts nonsymmorphic symmetry-protected Dirac band crossing at X and topologically trivial electron and hole pockets along $Z - R$ direction in Brillouin zone [14], all of which contribute to the transport. Quantum oscillations in ZrSiSe reveal a bulk Fermi pocket at 220 T [12], a topologically trivial surface state at 450 T [15], and a possible Weyl orbit frequency at 140 T, as described in Ch. 3.

In this chapter, we investigate the gate-induced effect on transport properties of ZrSiSe by fabricating ZrSiSe/hBN/graphite heterostructures and report our observations. Although an unambiguous conclusion requires further measurements and analysis, we will discuss our hypothesis and supporting evidence.

4.2 Experimental Methods

We fabricated Hall bar devices on ZrSiSe in top- and bottom-contacted geometries. Schematic and pictures of fabricated Hall bar devices are shown in Fig.4.1. Top-contacted devices were fabricated by exfoliation of ZrSiSe crystals inside a nitrogen glovebox (H_2O, $O_2 < 0.5$ ppm) on high-resistivity Si substrates (>10,000 Ω·cm) with 300 nm of thermal oxide treated by O_2 plasma at 200 mbar oxygen pressure and 75 W power for 60 seconds. Flakes with proper thickness were first identified by optical microscopy using a hermetic cell with optical access[16], and then thickness was measured using atomic force microscopy (Fig. S1 in the Supplementary Materials of chapter 2). To pattern Hall bar contacts on the flakes, PMMA C4 resist spun on the chip in air and baked at 180 °C inside the glovebox, followed by electron

beam lithography. PMMA dissolved in chlorobenzene was used because the more commonly used anisole-based resists were found to degrade the quality of ZrSiSe samples. 3/120 nm Cr/Au contacts were thermally evaporated, followed by lift-off in acetone. Thin flakes of hBN and graphite were identified and transferred onto the device using a dry transfer method involving PDMS and PPC [17] inside the glove box, Fig.4.1. The total air exposure in this process was limited to less than 5 minutes to minimize degradation of ZrSiSe.

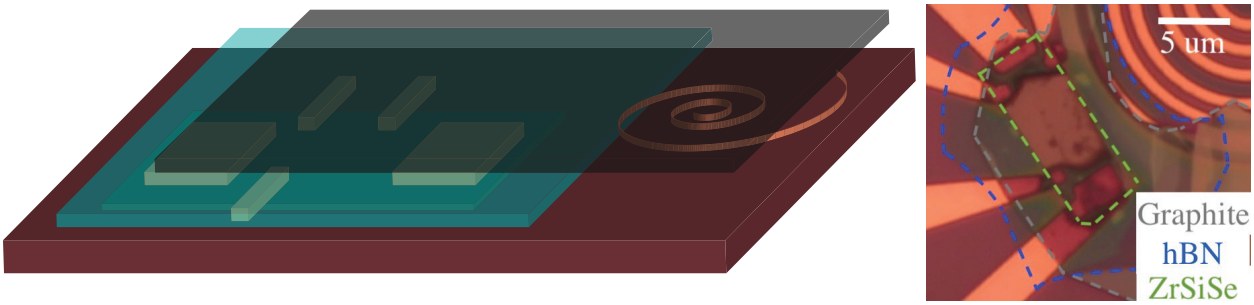

Figure 4.1: Schematic and optical micrograph of ZrSiSe devices in a Hall bar geometry and top gated with hBN/graphite heterostructures. The boundary of ZrSiSe, hBN, and graphite flakes is color coded with green, blue, and gray, respectively.

Bottom-contacted devices were prepared, starting with electron beam lithography on low-resistivity Si substrates (<0.05 Ω·cm) with 300 nm of thermal oxide to pattern 2/20 nm Cr/Au Hall bar contacts. To facilitate thin flake transfer of ZrSiSe, we mechanically exfoliated the crystals inside the glove box on an HF treated Si substrates with 90 nm of thermal oxide. Thin flakes were identified in the hermetic inspection cell and transferred onto the contacts using a dry transfer method involving PDMS and PPC [17] inside the glove box.

Devices were current annealed at room temperature and pressure to improve the contact resistance. Current up to 4 mA was passed through contact pairs. Magnetoresistance, Hall resistivity, and quantum oscillations were measured at 4 K using a constant current provided by a voltage-controlled current source and standard lock-in techniques. The gate voltage was applied through a digital to analog converter, and the gate leakage was measured by inserting a 1 $M\Omega$ resistor with the gate and measuring the voltage drop across the resistor.

4.3 Results

The normalized change in resistivity due to application of gate voltage is extracted as $\frac{\Delta\rho}{\rho_0}$, where $\Delta\rho = \rho_v - \rho_0$ is the change in resistivity, and $\rho_0 = (V_{xx}/I) \cdot (wL/l_{in})$ is the longitudinal resistivity of device at zero gate voltage, $V_g = 0\ V$. Here w is the width of the sample, L is the thickness, and l_{in} is the length between the inner voltage probes. A 2D plot of change in resistivity at $T = 4\ K$ and various magnetic fields is provided in Fig. 4.2a. Charge neutrality point is observable at $V_g = 0.8\ V$, the minimum of the change in resistivity. When the magnetic field is less than 2 T, away from the charge neutrality point, the resistivity increases with gate voltage up to 30% at 0 T and $V_g = -1.9\ V$, Fig. 4.2b. As the magnetic field increases, the resistivity change gets more subtle and finally vanishes close to 2 T. The resistivity decreases with gate voltage for fields larger than 2 T. The change in resistivity is almost the same for fields between 3 T and 7.5 T, close to -5%, indicating that higher magnetic fields will not change the gate dependency of resistivity significantly. Although the resolution of data in Fig. 4.2a is relatively high, it does not reflect quantum oscillations because the step size in the magnetic field does not meet the required resolution.

Magnetic field dependence of resistivity is plotted in Fig. 4.2c. Increasing the gate voltage away from the charge neutrality point reduces the curvature of quadratic behavior in longitudinal resistivity. This change is magnified in insets of Fig. 4.2c such that moving away from the charge neutrality point increases the resistivity at fields below 2 T and decreases the resistivity at fields above 2 T. This change results in a decrease in magnetoresistance by $\sim 25\%$ at $V_g = -2.9\ V$, Fig.4.2d.

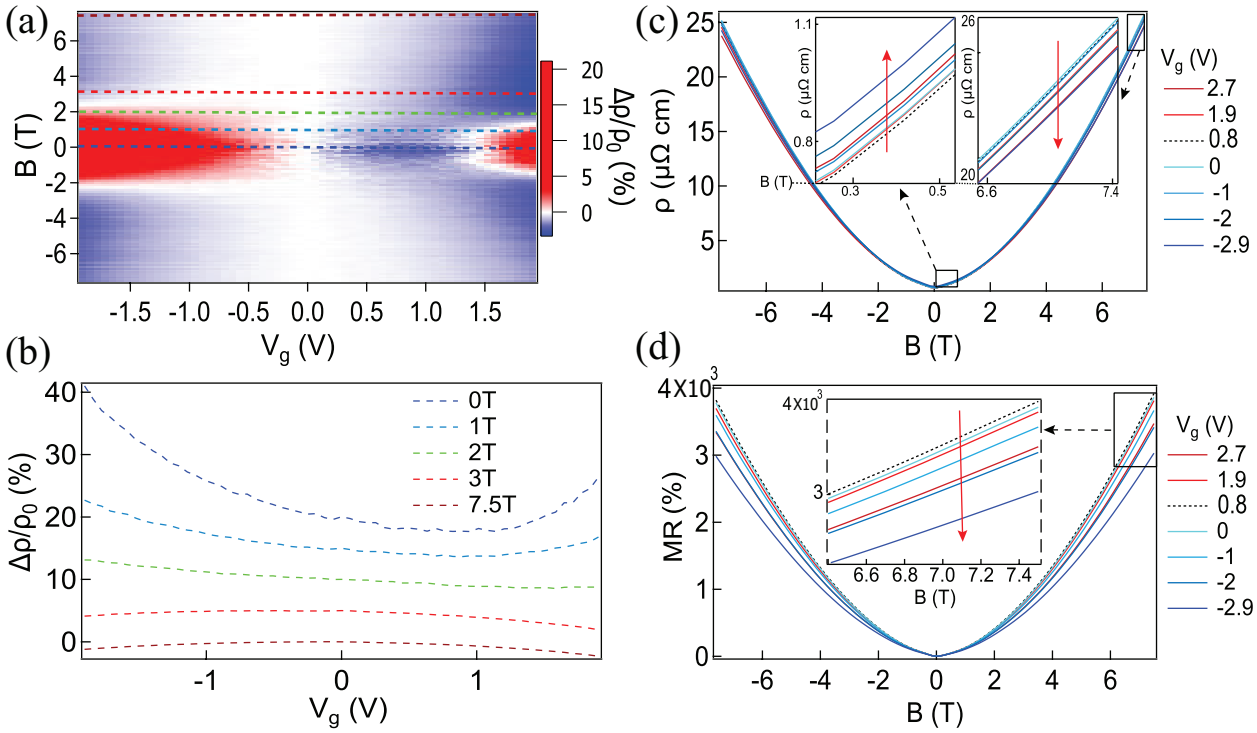

Figure 4.2: (a) The 2D plot of the change in resistivity by sweeping over the gate voltage at various magnetic fields at T=4 K. The red color corresponds to an increase in resistivity, and the blue color corresponds to a decrease in resistivity. The charge neutrality point is the blue spot at 0.8 V. (b) is the horizontal cross-section of (a) with matching colors dashed lines. (c) the field dependence of resistivity at various gate voltages. Insets show zoomed-in segments with the blue arrow indicating the increase(decrease) in field dependence of resistivity at low(high) fields. (d) The magnetoresistance at various gate voltages.

In addition to the gate-induced change in resistivity, we observed gate-induced effects on quantum oscillation. The amplitude of Shubnikov de Haas oscillations in longitudinal resistivity decreases as the gate voltage increase, Fig.4.3, this change is symmetric across $V_g = 0\ V$ and does not reflect the charge neutrality point at 0.8 V. In addition to the change in oscillation amplitude, an increase in the gate voltage away from 0 V blueshifts the 140 T frequency. In contrast, the bulk oscillation frequency 220 T remains unaffected by the gate voltage. Again this change is symmetric around 0 V and does not reflect the charge neutrality point.

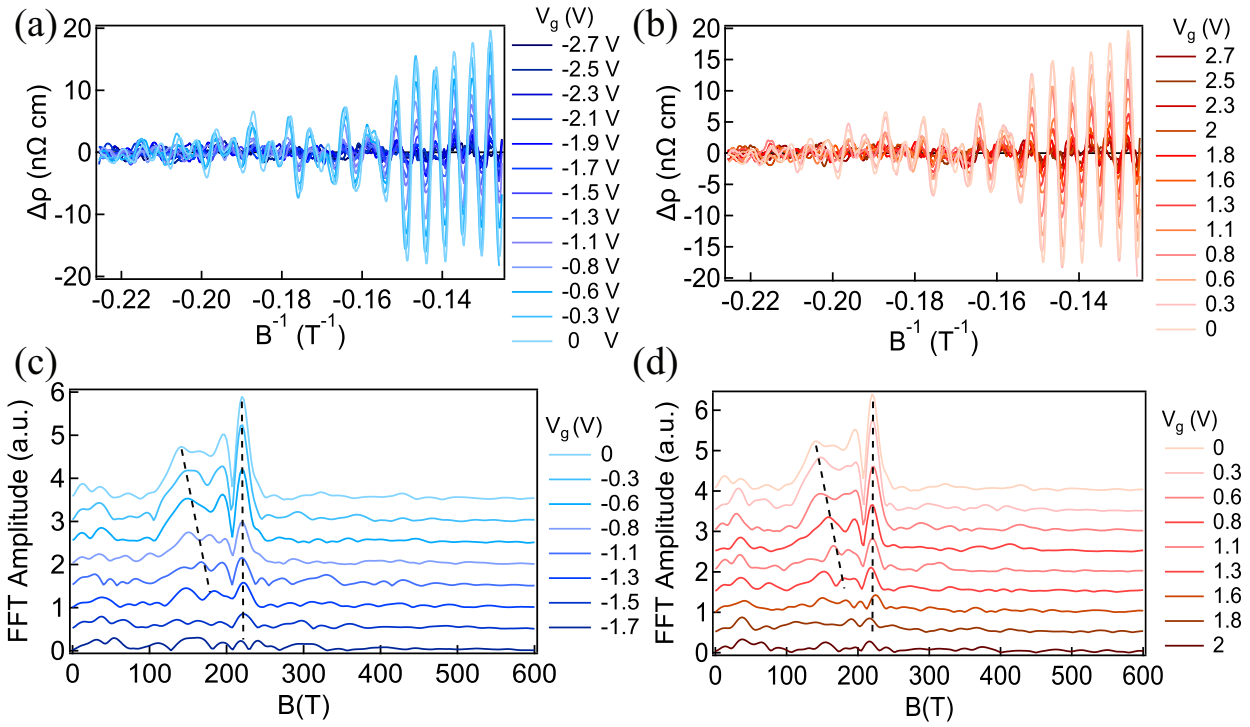

Figure 4.3: (a) and (b) are the Shubnikov de Haas oscillations in device A for negative and positive gates, respectively. The temperature is at 4 K, and the field is perpendicular to the surface of the device. (c) and (d) are the frequency spectrum of oscillations from the Fast Fourier Transform of (a) and (b)

The change in amplitude of quantum oscillation is robustly visible in a 2D plot of oscillations at high magnetic field range and gate voltage, Fig.4.4a. The oscillation is robust at zero gate voltage and fades away as the voltage gets away from $V_g = 0\ V$ in both positive and negative directions. The change in 140 T frequency is almost visible in this 2D plot. Fig. 4.4b is the change in frequency of 140 T obtained from the frequency spectrum in Fig. 4.3. The dashed line is a quadratic fit and is the closest polynomial fit to the experimental data.

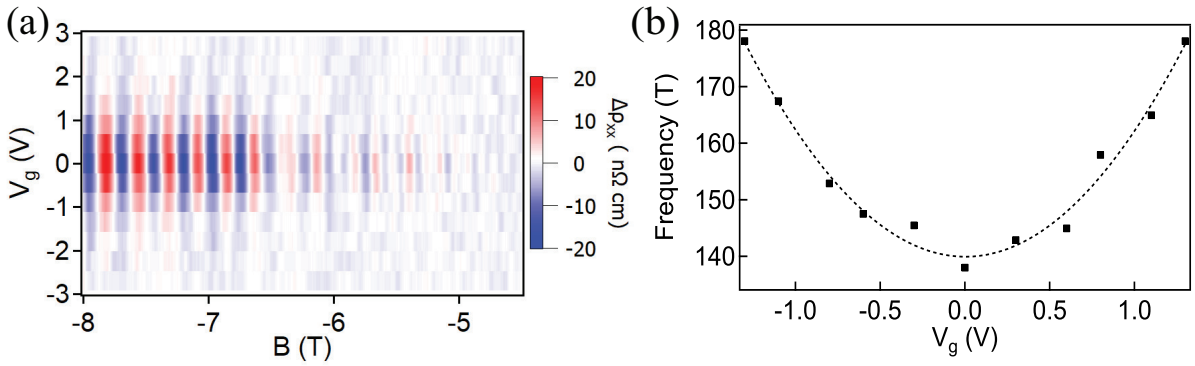

Figure 4.4: (a) The effect of gate voltage on the amplitude of quantum oscillations of longitudinal magnetoresistance at 4 K in the perpendicular magnetic field in the range of 4 to 8 T, where the oscillations are visible. (b) The blueshift in the frequency of 140 T with gate effect. The fitted line is a quadratic fit to the data.

Temperature dampening of quantum oscillations is used to obtain the effective mass, m*, in device B. Lifshitz-Kosevich formalism 1.2 describes this damping effect, the oscillation amplitude changes as $A(T) = A_0 \frac{2\pi^2 K_b T}{\hbar\omega_c}$, where K_b is the Boltzman constant and $\Omega_c = \frac{eB}{m^*}$ is the cyclotron frequency. Our raw data at $V_g = 0\ V$ is limited to the oscillation in transverse resistivity, which displays multiple frequencies. In contrast, our raw data at $V_g = 120\ V$ is limited to the oscillation in longitudinal resistivity, which displays single bulk 220 T frequency. Standard high pass Finite Impulse Response (FIR) digital filter with a cut-off frequency of 200 T is applied to raw data at $V_g = 0\ V$ for extraction of oscillations with bulk frequency 220 T, Fig. 4.5(a). This filtering makes it possible to have an apple-to-apple comparison with oscillations in longitudinal resistivity at $V_g = 120\ V$, Fig. 4.5(b). Quantum oscillations at the peak closest to 0.14 T^{-1} were extracted and plotted against temperature, Fig. 4.5(c). The Lifshitz-Kosevich fit to the data results in $m_0^* = 0.09m_e$ and $m_{120}^* = 0.1m_e$, where m_e is the rest mass of electron, and m_x^* is the effective mass at $V_g = x\ V$.

	$V_g = 0\ V$	$V_g = 120\ V$
n_e	3.8×10^{20}	5.6×10^{20}
μ_e	5.1×10^{4}	5.8×10^{4}
n_h	2.8×10^{21}	3.1×10^{21}
μ_h	9.1×10^{3}	9.8×10^{3}

Table 4.1: carrier density ($\frac{1}{cm^3}$) and mobility ($\frac{cm^2}{V.S}$) obtained from fitting a two-band model to the magnetoconductance of device B, Fig. 4.5d

We obtained magnetoconductivity of device B at 4 K by inverting the resistivity tensor $\sigma_{xx}(B) = \frac{\rho_{xx}(B)}{\rho_{xx}^2(B)+\rho_{xy}^2(B)}$, where $\rho_{xx}(B)$ is the longitudinal resistivity and $\rho_{xy}(B)$ is the transverse resistivity. To obtain the carrier density and mobility, we fit the magnetoconductivity to a two-band model [18–20], $\sigma_{xx}(B) = \frac{1}{\rho_1+A_1B^2} + \frac{1}{\rho_2+A_2B^2}$ where $\rho_i = \frac{1}{n_i e \mu_i}$ and $A_i = \frac{\mu_i}{n_i e}$, with μ and n the mobility and carrier density, respectively. As shown in Fig. 4.5d, the two-band model yields a satisfactory fit to the measured data, from which the carrier densities and mobilities are extracted, Table. 4.1.

Longitudinal conductivity and the fit to the data in device B are satisfactory, but the reliability of the data is doubtful. First, the extracted mobility and density do not match other devices. Second, although the gate-induced effects on a quantum oscillation in device B are similar to Device A, refer to Appendix C for data, the resistivity in device A has a systematic change with gate voltage, but the resistivity of device B has a sharp change at $V_g = 80\ V$. In addition, gate-induced effects are more prominent in device A, in contrast to device B, which shows a subtle change. The resistivity of device A systematically increases at zero field; in contrast, the resistivity of device B sharply decreases.

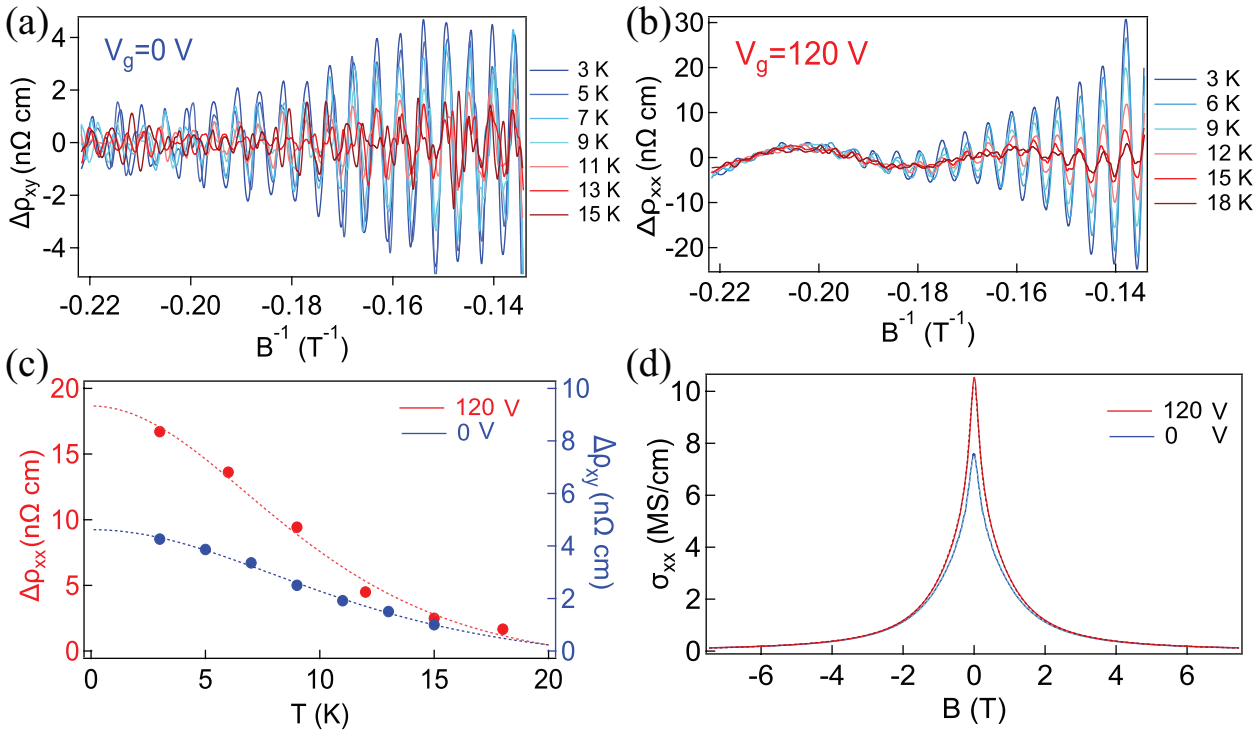

Figure 4.5: Extraction of effective mass, carrier mobility, and density in device B. (a) is the temperature dependence of quantum oscillations in transverse resistivity filtered using FIR digital high pass filter with a cutoff range of 200 T at $V_g = 0\ V$. (b) The temperature dependence of quantum oscillations in longitudinal resistivity at $V_g = 120\ V$. (c) The extraction of effective mass from oscillations in (a) and (b) at the peak of oscillations near 0.14 T^{-1}. Dashed lines are the fit with temperature dependence part of Lifshitz-Kosevich formalism. (d) Extraction of carrier density and mobility from longitudinal conductivity, the solid blue(red) line is the longitudinal conductivity at 0 V(120 V) gate voltage. Dashed lines are the two-band model fit to the data.

4.4 Discussion

The observation of the charge neutrality point at $V_g = 0.8\ V$ suggests hole carriers' dominant contribution to transport. The gating effect away from the charge neutrality point is prominent and systematic. At fields below 2 T, the gate voltage increases the resistivity in both directions away from the charge neutrality point; this is in contrast with the expectation from gate-induced effects in conventional semimetal, where moving in directions away from the charge neutrality point should decrease the resistivity. At higher fields, more than 2 T, the gate-induced effects decrease the resistivity away from the charge neutrality point; this

behavior is more like conventional semimetals. We speculate that breaking inversion symmetry and spin-orbit coupling might be responsible for such behaviors. First, breaking inversion symmetry using an electric field can open up a band gap, as shown for bilayer graphene[5, 6], hence the observed increase in resistivity away from the charge neutrality point (which is not compatible with a trivial semimetallic picture) can be explained by considering the nontrivial topological aspect of ZrSiSe and breaking inversion symmetry. Further studies on double gated ZrSiSe are required to break inversion symmetry while keeping the carrier density unchanged and unambiguously confirming the first point. Second, the nodal line is always in positive energy hence contributing with hole pockets to the transport; this is compatible with the observation of charge neutrality point at positive gate voltage, 0.8 V. Third, ZrSiSe nodal lines are symmorphic; hence, they are not protected against spin-orbit coupling and completely gap out. The maximum distance of Dirac nodal lines from E_f is 60 meV; the spin-orbit coupling can induce a gap up to 36 meV [13]. Since the nodal lines fall in energy distance comparable to the gap, these bands can gap in a way that shows insulating behavior, eliminating their contribution to the transport. We conjecture that at 2 T these Nodal lines fall into the insulating regime hence the transport in ZrSiSe is dominated by topologically trivial semimetallic bands between $Z-R$ and nonsymmorphic topological bands at $\Gamma-X-M$ symmetry of Brillouin zone.

In addition, we observed a decrease in magnetoresistance of ZrSiSe by application of gate voltage away from the charge neutrality point. In topologically trivial paramagnetic metallic systems, the magnetoresistance is quadratic and only depends on mobility and carrier density. Adjustment of the Fermi level would change these parameters resulting in a change in magnetoresistance. The carrier density and mobility, Table 4.1, increase with the application of electric field; this suggests the magnetoresistance should change too. Considering the uncertainty in the data of Table.4.1, we can not have a concrete conclusion at this point. Further studies are required to investigate this matter.

Another interesting gate-induced effect is on quantum oscillations. We observed the amplitude of oscillations decrease with gate voltage; similar results exist for phosphorene [21]. We hypothesize that this result agrees with the increase in effective mass due to gate-induced effects, Fig. 4.4. Lifshitz-Kosevich formalism, Eq.1.11, suggests that the effective mass appears at the temperature-dependent and the Dingle segment. For the temperature segment, an increase in the effective mass has a similar effect as an increase in temperature, reducing the oscillation. The Dingle section is exponential in $-m^*$; hence an increase in effective mass will again reduce the oscillation amplitude. A solid confirmation can happen by extracting effective mass at various gate voltages and plotting oscillation amplitude versus effective mass. This plot should follow Lifshitz-Kosevich's formalism to confirm our hypothesis. Nevertheless, the effect of the electric field on the effective mass remains elusive and requires further experiments. Additionally, the suppression of oscillations happens in both bulk and Weyl frequency. Considering the thickness of our device is 52 nm, and the depletion length of an electric field is a few nm, such suppression in bulk frequency is unexpected; this suppression is also observed in device B, which is 300 nm. The top gated device A is top contacted, and back gated device B is bottom contacted; hence it is expected to observe gate effects on the few layers that are affected by the gate, but assuming a uniform distribution of conduction channels through the flake, which is a logical assumption for bulk Fermi surface, one would expect the bulk frequency should remain strong because many layers will not be affected by the electric field. In contrast, we observed the opposite, hinting at a more complicated process. We speculate that Weyl orbit might be responsible for this unconventional behavior. The carriers in the Weyl orbit oscillate between the top and bottom surface of material [22]. Hence all the carriers will experience the gate effect. This hypothesis can be tested by fabricating top(bottom) gated and bottom(top) contacted devices with 100 nm thickness. Observation of gate-induced effects in such a scenario confirms the hypothesis and can unambiguously detect Weyl orbits.

Further, we observed a systematic blueshift in the 140 T frequency of oscillation, Fig. 4.4b. In the previous chapter, we provided evidence that this frequency is of the Weyl orbit. Considering the thickness of device A is 50 nm, and the depletion length of the electric field is a few nm, such a strong blueshift suggests that this frequency has a 2D nature. In contrast, the shift in bulk frequency appears to be a redshift, but the data resolution is insufficient to confirm this unambiguously. Since a larger gate voltage is required to study the possible redshift in bulk frequency unambiguously, and the oscillation amplitudes decrease with gate voltage, measurements at a higher magnetic field are required to settle this debate. Regardless, the bulk frequency behaves differently under the electric field than the Weyl frequency. The Weyl frequency shows a quadratic behavior and is symmetric around $V_g = 0\ V$. For a semimetal to show such behavior, the Fermi level must be precisely at the band crossing. This is in contrast with the observation of the charge neutrality point at $V_g = 0.8\ V$. Hence this change must have a different origin than the adjustment of the Fermi level. Further studies are required to understand this blueshift in potentially Weyl frequency. Similarly, the possible redshift in bulk frequency requires further experiments, and the origin of such a shift might be interesting considering the thickness dependence redshift in bulk frequency observed in the previous chapter, Fig. 3.5.

4.5 Conclusion

We observed multiple gate-induced effects on a 50 nm ZrSiSe device, some of which were reproduced in a 300 nm device. First, the electrostatic gate away from the charge neutrality point increases the resistivity. This observation was not confirmed in the 300 nm device; in fact, we observed the opposite, but as explained, the data of the 300 nm device might be doubtful. The change in resistivity is positive at fields below 2 T and is negative at fields larger than 2 T. We hypothesize that the electrostatic gate gaps out the Dirac nodal line by breaking inversion symmetry and provided four pieces of evidence to support this hypothesis. First, other Dirac materials show a gate-induced gap in their band crossing. Second, it is

impossible to explain the resistivity increase away from the charge neutrality point with a topologically trivial semimetallic picture. Third, the contribution of the nodal line to the transport is through hole pockets, and the observation of charge neutrality point below 2 T confirms dominant hole carriers. Fourth, the absence of charge and the conventional gate effect above 2 T suggest the topologically non-trivial band is not contributing to the transport above 2 T. This is expected for nodal lines because their energy falls within a distance of Fermi level comparable to the gap induced by the spin-orbit coupling.

In addition, we observed gate-induced effects on quantum oscillations of the 52 nm device. These effects were reproducible in the 300 nm device. The gate voltage suppresses the oscillation amplitude and is symmetric for both positive and negative gate voltages. We conjecture that this suppression might root in the increase of the effective mass with gate voltage, our data points are limited, and further measurements of effective mass at various gate voltages are required to confirm this hypothesis unambiguously. Regardless, the underlying physical process is still ambiguous, and further theoretical study on the role of the out-of-plane electric field in ZrSiSe is required. In addition, we observed a large blueshift in the potential Weyl orbit frequency while the bulk frequency is either redshifted or unchanged. Further experiments at high fields are required required to resolve possible frequency shift in bulk oscillations. In addition, theoretical studies are required to address these shifts in frequencies.

References

[1] Mengqiao Sui, Guorui Chen, Liguo Ma, Wen-Yu Shan, Dai Tian, Kenji Watanabe, Takashi Taniguchi, Xiaofeng Jin, Wang Yao, Di Xiao, et al. Gate-tunable topological valley transport in bilayer graphene. *Nature Physics*, 11(12):1027–1031, 2015.

[2] Ebrahim Sajadi, Tauno Palomaki, Zaiyao Fei, Wenjin Zhao, Philip Bement, Christian Olsen, Silvia Luescher, Xiaodong Xu, Joshua A Folk, and David H Cobden. Gate-induced superconductivity in a monolayer topological insulator. *Science*, 362(6417):922–925, 2018.

[3] Jiewei Chen, Ting Zhang, Jingli Wang, Lin Xu, Ziyuan Lin, Jidong Liu, Cong Wang, Ning Zhang, Shu Ping Lau, Wenjing Zhang, et al. Topological phase change transistors based on tellurium weyl semiconductor. *Science Advances*, 8(23):eabn3837, 2022.

[4] Luojun Du, Tawfique Hasan, Andres Castellanos-Gomez, Gui-Bin Liu, Yugui Yao, Chun Ning Lau, and Zhipei Sun. Engineering symmetry breaking in 2d layered materials. *Nature Reviews Physics*, 3(3):193–206, 2021.

[5] Eduardo V Castro, KS Novoselov, SV Morozov, NMR Peres, JMB Lopes Dos Santos, Johan Nilsson, F Guinea, AK Geim, and AH Castro Neto. Biased bilayer graphene: semiconductor with a gap tunable by the electric field effect. *Physical review letters*, 99(21):216802, 2007.

[6] Yuya Shimazaki, Michihisa Yamamoto, Ivan V Borzenets, Kenji Watanabe, Takashi Taniguchi, and Seigo Tarucha. Generation and detection of pure valley current by electrically induced berry curvature in bilayer graphene. *Nature Physics*, 11(12):1032–1036, 2015.

[7] Yuanbo Zhang, Tsung-Ta Tang, Caglar Girit, Zhao Hao, Michael C Martin, Alex Zettl, Michael F Crommie, Y Ron Shen, and Feng Wang. Direct observation of a widely tunable bandgap in bilayer graphene. *Nature*, 459(7248):820–823, 2009.

[8] Su-Yang Xu, Qiong Ma, Huitao Shen, Valla Fatemi, Sanfeng Wu, Tay-Rong Chang, Guoqing Chang, Andrés M Mier Valdivia, Ching-Kit Chan, Quinn D Gibson, et al. Electrically switchable berry curvature dipole in the monolayer topological insulator wte2. *Nature Physics*, 14(9):900–906, 2018.

[9] Yang Zhang, Jeroen van den Brink, Claudia Felser, and Binghai Yan. Electrically tuneable nonlinear anomalous hall effect in two-dimensional transition-metal dichalcogenides wte2 and mote2. *2D Materials*, 5(4):044001, 2018.

[10] Xiaodong Xu, Wang Yao, Di Xiao, and Tony F Heinz. Spin and pseudospins in layered transition metal dichalcogenides. *Nature Physics*, 10(5):343–350, 2014.

[11] Leslie M Schoop, Mazhar N Ali, Carola Straßer, Andreas Topp, Andrei Varykhalov, Dmitry Marchenko, Viola Duppel, Stuart SP Parkin, Bettina V Lotsch, and Christian R Ast. Dirac cone protected by non-symmorphic symmetry and three-dimensional dirac line node in zrsis. *Nature communications*, 7(1):1–7, 2016.

[12] Jin Hu, Zhijie Tang, Jinyu Liu, Xue Liu, Yanglin Zhu, David Graf, Kevin Myhro, Son Tran, Chun Ning Lau, Jiang Wei, et al. Evidence of topological nodal-line fermions in ZrSiSe and ZrSiTe. *Physical review letters*, 117(1):016602, 2016.

[13] Y-C Chiu, K-W Chen, Rico Schoenemann, VL Quito, S Sur, Q Zhou, D Graf, E Kampert, T Förster, K Yang, et al. Origin of the butterfly magnetoresistance in a dirac nodal-line system. *Physical Review B*, 100(12):125112, 2019.

[14] M Mofazzel Hosen, Klauss Dimitri, Ilya Belopolski, Pablo Maldonado, Raman Sankar, Nagendra Dhakal, Gyanendra Dhakal, Taiason Cole, Peter M Oppeneer, Dariusz Kaczorowski, et al. Tunability of the topological nodal-line semimetal phase in zrsi x-type materials (x= s, se, te). *Physical Review B*, 95(16):161101, 2017.

[15] Xue Liu, Chunlei Yue, Sergey V Erohin, Yanglin Zhu, Abin Joshy, Jinyu Liu, Ana M Sanchez, David Graf, Pavel B Sorokin, Zhiqiang Mao, et al. Quantum transport of the 2d surface state in a nonsymmorphic semimetal. *Nano letters*, 21(11):4887–4893, 2021.

[16] Josh P Thompson, M Hasan Doha, Peter Murphy, Jin Hu, and HO Churchill. Exfoliation and analysis of large-area, air-sensitive two-dimensional materials. *Journal of visualized experiments*, 143, 2019.

[17] Lei Wang, I Meric, PY Huang, Q Gao, Y Gao, H Tran, T Taniguchi, Kenji Watanabe, LM Campos, DA Muller, et al. One-dimensional electrical contact to a two-dimensional material. *Science*, 342(6158):614–617, 2013.

[18] Jin Hu, JY Liu, David Graf, SMA Radmanesh, DJ Adams, Alyssa Chuang, Yu Wang, Irinel Chiorescu, Jiang Wei, Leonard Spinu, et al. π berry phase and zeeman splitting of weyl semimetal tap. *Scientific reports*, 6(1):1–8, 2016.

[19] Xiaochun Huang, Lingxiao Zhao, Yujia Long, Peipei Wang, Dong Chen, Zhanhai Yang, Hui Liang, Mianqi Xue, Hongming Weng, Zhong Fang, et al. Observation of the chiral-anomaly-induced negative magnetoresistance in 3D Weyl semimetal TaAs. *Physical Review X*, 5(3):031023, 2015.

[20] Jin Hu, Su-Yang Xu, Ni Ni, and Zhiqiang Mao. Transport of topological semimetals. *Annual Review of Materials Research*, 49:207–252, 2019.

[21] Nathaniel Gillgren, Darshana Wickramaratne, Yanmeng Shi, Tim Espiritu, Jiawei Yang, Jin Hu, Jiang Wei, Xue Liu, Zhiqiang Mao, Kenji Watanabe, et al. Gate tunable quantum oscillations in air-stable and high mobility few-layer phosphorene heterostructures. *2D Materials*, 2(1):011001, 2014.

[22] Andrew C Potter, Itamar Kimchi, and Ashvin Vishwanath. Quantum oscillations from surface fermi arcs in weyl and dirac semimetals. *Nature communications*, 5(1):1–6, 2014.

Chapter 5

Superconductor/Antiferromagnet/Superconductor Josephson Junction

The interplay between magnetic materials and superconductors provides an exciting playground due to opposing requirements for electron spin alignment between superconductivity and magnetic order [1]. The magnetic order of a few magnetic layer materials can be probed by tunneling spectroscopy due to the spin filtering effect, see Sec. 1.5. Usually, Josephson Junctions with graphene as the conductive material is used for tunneling spectroscopy because graphene properties are very well studied, and any non-graphene behavior can reflect the change in the potential barrier. Replacing graphene with a layered superconductor can produce exciting results. Here we used $NiPS_3$, an antiferromagnetic layered material with in-plane antiferromagnetic order, and FeSe, a layered superconductor, to fabricate superconductor/antiferromagnet/superconductor (FeSe/$NiPS_3$/FeSe) Josephson Junction. In addition, we fabricated a control Josephson Junction using graphite and a similar thickness of $NiPS_3$, graphite/$NiPS_3$/graphite, to have a fair comparison with the superconductor Josephson Junction. We showed that our devices were in a direct tunneling regime at temperatures lower than 20 K and 10 K for graphite-JJ and FeSe-JJ, respectively. Basnet et al. [2] have shown that $NiPS_3$ undergoes a spin-flop transition in magnetic fields parallel to the ab plane and larger than 6 T. Although we did not investigate spin-flop transition for fields parallel to the ab plane, due to the limits with our experimental setup, we observed signatures of possible spin-flop transition in magnetic fields parallel to the c axis for the similar magnetic field in our controlled graphite device. However, this observation is ambiguous because such a spin-flop transition was not observed in bulk measurements [2]. Further, we observed steps in the temperature dependence of resistivity for FeSe-JJ; these steps do not exist in the control graphite-JJ; hence we attribute them to FeSe. The steps in the temperature dependence of resistivity happen at 50 K and 10 K; the latter coincides with the transition temperature of FeSe to a superconductor. In addition, we observed anisotropic and unconventional magne-

toresistance in temperatures between 50 K and 10 K. This anisotropic magnetoresistance disappears at temperatures lower than 10 K when FeSe becomes superconductor.

5.1 Introduction

Tunneling spectroscopy has been used to probe magnetic orders in 2D materials [3, 4]. These experiments were successful in detecting out-of-plane to in-plane spin flop transitions in antiferromagnetic materials that are ferromagnetic within each layer, such as CrI_3 [5, 6], and that are antiferromagnetic within each layer, such as $MnPS_3$ [7]. This is because of the spin filtering effect, where carriers tunnel through layered magnetic insulators and show higher current if the magnetization of layers is in the same direction compared to the opposite direction, Sec. 1.5. Hence, temperature dependence and magnetoresistance can be used to probe the magnetic phase in the tunneling barriers.

Although conventional tunneling spectroscopy uses graphene as the choice of the top and bottom conductive layer, variations in these layers in combination with magnetically ordered materials can result in exciting physics and anomalous phenomena. For example, using a superconductor in combination with a ferromagnetic material can result in fascinating phenomena such as giant anisotropic magnetoresistance, unconventional and topological superconductivity [1, 8–10]. This is due to the incompatibility of magnetism with superconductivity, which arises from the opposing requirements on electron spin alignment. We fabricated FeSe/$NiPS_3$/FeSe Josephson Junctions (FeSe-JJ) to explore the exciting physics arising from the proximity of a superconductor with an antiferromagnetic material.

$NiPS_3$ is a layered material that poses Heisenberg-type antiferromagnetic order with Neel temperature of $T_N = 155\ K$ [2]. The magnetic moments of this material are in ab-plane and antiferromagnetic within each layer. The band gap of this material is $1.2 - 1.4\ eV$, and the work function is $5\ eV$ [11]. $NiPS_3$ shows strong Mott-insulator behavior at room temperature and atmospheric pressure, but theoretical and experimental studies revealed pressure-induced

insulator to metal transition [12, 13]. Due to the large band gap and work function and possessing antiferromagnetic order, $NiPS_3$ is a good candidate to investigate the combination of magnetism with superconductivity.

FeSe is a layered superconductor with $T_c = 10\ K$ and nematic electronic structure [14, 15]. The Fermi surface of FeSe deforms from fourfold to twofold symmetry across nematic transition at 87 K; there is no consensus on the origin of this nematic transition [16, 17]. Temperature dependence of energy distribution curves from ARPES data shows the number of peaks doubles in the nematic phase at temperatures close to 50 K [17], and the magnitude of this splitting sharply increases down to 10 K. The layered characteristic of FeSe and the aforementioned exciting features make this material a good candidate for studying the interplay of magnetically ordered materials with superconductors.

5.2 Experimental Methods

We fabricated graphite/$NiPS_3$/graphite, and FeSe/$NiPS_3$/FeSe Josephson Junctions (graphite-JJ and FeSe-JJ, respectively) for tunneling experiments. Schematic and optical micrographs of fabricated tunneling devices are shown in Fig.5.1. Devices were fabricated by exfoliation of materials on Si substrates with 90 nm of thermal oxide, which was treated by diluted hydrofluoric (HF) acid. The HF-treated Si substrate facilitates the flake transfer in the fabrication process. First, flakes with proper thickness were identified by optical microscopy using a hermetic cell with optical access [18], and then thickness was measured using atomic force microscopy. The thickness of $NiPS_3$ was similar, $\sim$4 nm, in both devices; refer to appendix D for AFM images.

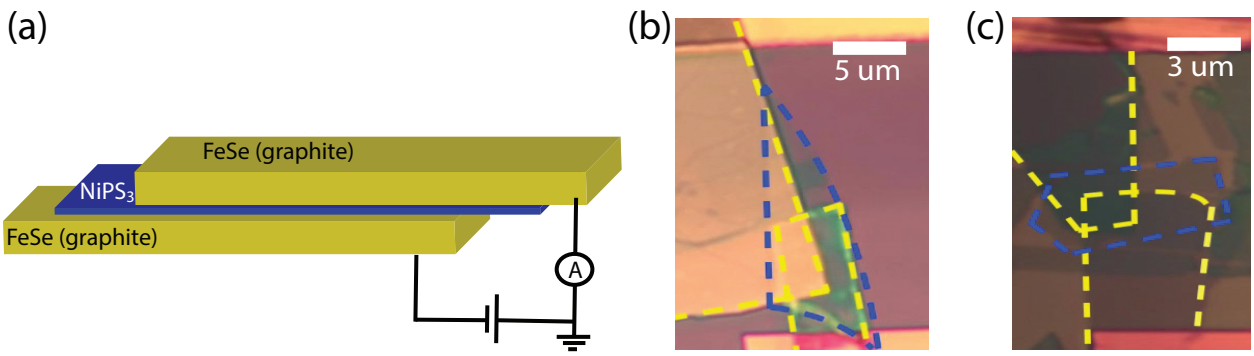

Figure 5.1: (a) 3D Schematic of tunneling devices, blue and yellow colors show the tunneling layer and top and bottom (super-)conductor, respectively. (b) Optical micrograph of $FeSe/NiPS_3/FeSe$ heterostructure, the boundary of top and bottom FeSe is shown with yellow dashed lines, and the boundary of the tunneling layer, $NiPS_3$, is shown with blue dashed lines. (c) The optical micrograph of graphite/$NiPS_3$/graphite device. Yellow and blue dashed lines show the boundary of graphite and tunneling layer, respectively.

We patterned contacts on high-resistivity Si substrates (>10,000 Ω·cm) with 300 nm of thermal oxide. PMMA A4 was spun and baked at 180 °C, followed by electron beam lithography. 2/20 nm Cr/Au contacts were thermally evaporated, Fig.5.1b,c. Crystals were mechanically exfoliated inside the glove box, thin flakes were identified in the hermetic inspection cell, and the bottom layer of graphite(FeSe) was transferred onto the contacts using a dry transfer method involving PDMS and PPC [19]. In separate events, a similar method was used to transfer the tunneling layer, $NiPS_3$, and the top-layer graphite(FeSe).

DC tunneling current is measured using a current pre-amplifier connected to the drain of the device. A standard two-probe DC setup was used to measure the resistivity of the tunneling barrier. In addition, we measured differential conductance using standard lock-in techniques. The AC (excitation) and DC (bias) voltage were applied to the device using a voltage divider, and DC voltage was set to be at least two orders of magnitude larger than AC voltage for conventional differential conductance measurements.

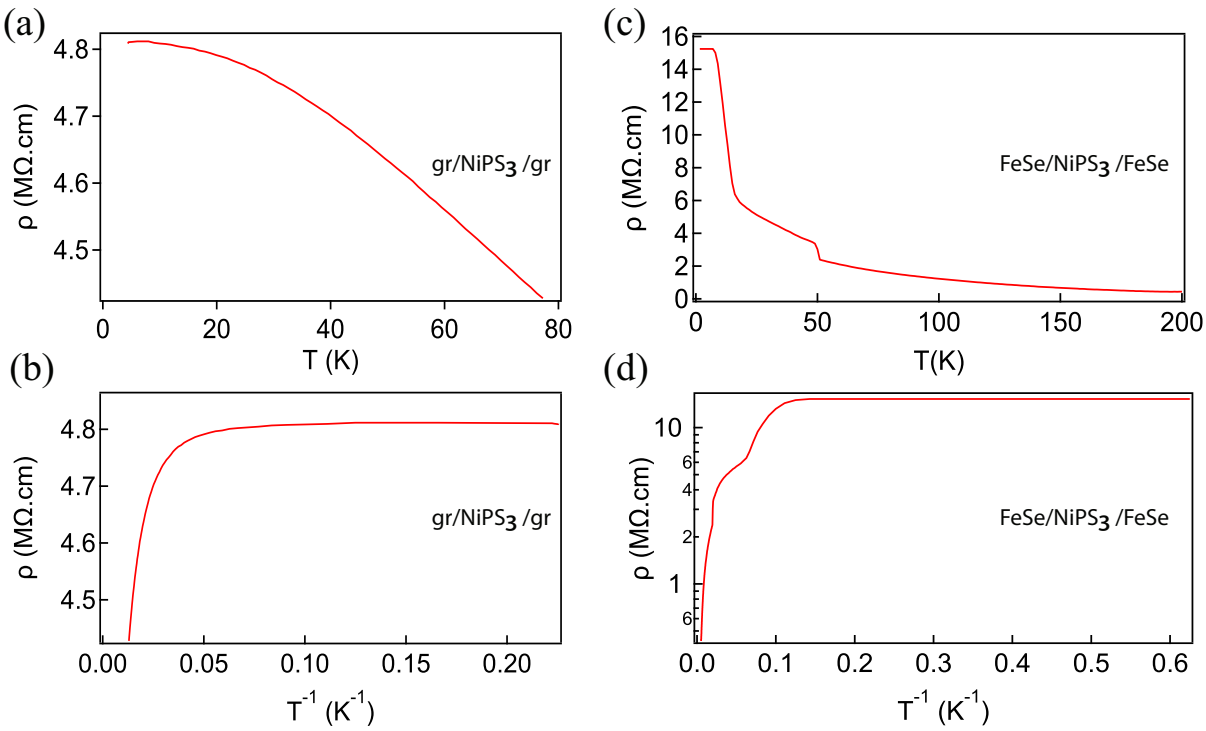

Figure 5.2: Temperature dependence of resistivity for graphite/NiPS3/graphite (a), and FeSe/NiPS3/FeSe (b) heterostructures. The temperature dependence of resistivity in graphite/NiPS3/graphite heterostructure shows a smooth change, in contrast, the resistivity in FeSe/NiPS3/FeSe has two jumps at $\sim 50\ K$ and $10\ K$. (b) and (d) are logarithmic view of resistivity as a function of inverse temperature. The tunneling range starts at 0.1 K^{-1} for FeSe/NiPS3/FeSe, (b), and 0.05 K^{-1} for graphite/NiPS3/graphite, (d).

5.3 Results

We extracted the resistivity of each device as $\rho = (V/I) \cdot (WL/t)$, where V is the DC bias voltage across the heterostructure, I is the tunneling current, WL is the effective tunneling area, and t is the thickness of the tunneling barrier.

The resistivity of graphite/$NiPS_3$/graphite smoothly increased as the temperature decreased, Fig. 5.2a, and reached an asymptotic behavior at low temperatures. The plot of resistivity as a function of the inverse of field, Fig. 5.2b, clearly shows the asymptotic regime starting at 20 K, indicating the device is in a tunneling regime below this temperature. In comparison, the resistivity of FeSe/$NiPS_3$/FeSe shows two sharp increases at 50 K and 10 K, where the

increase in resistivity at 10 K is more significant than 50 K, Fig. 5.2c. This device shows the asymptotic regime starting at 10 K, Fig. 5.2d, indicating the device is in the tunneling regime below this temperature.

Next, we will focus on magnetoresistance in graphite/$NiPS_3$/graphite. The magnetic field is applied perpendicular to the plane of the heterostructure. $\Delta\rho$ is the change in resistivity in the absence of quadratic magnetoresistance background. The quadratic magnetoresistance is obtained from a fit to the data and does not perfectly describe the exact functional form of experimentally observed magnetoresistance but can successfully remove the large profile of magnetoresistance that washed out small deviations. A sharp change from positive to negative $\Delta\rho$ is observable at 6.2 T for temperatures lower than 150 K. In addition, $\Delta\rho$ shows oscillations/peaks symmetric in the field for temperatures less than 45 K.

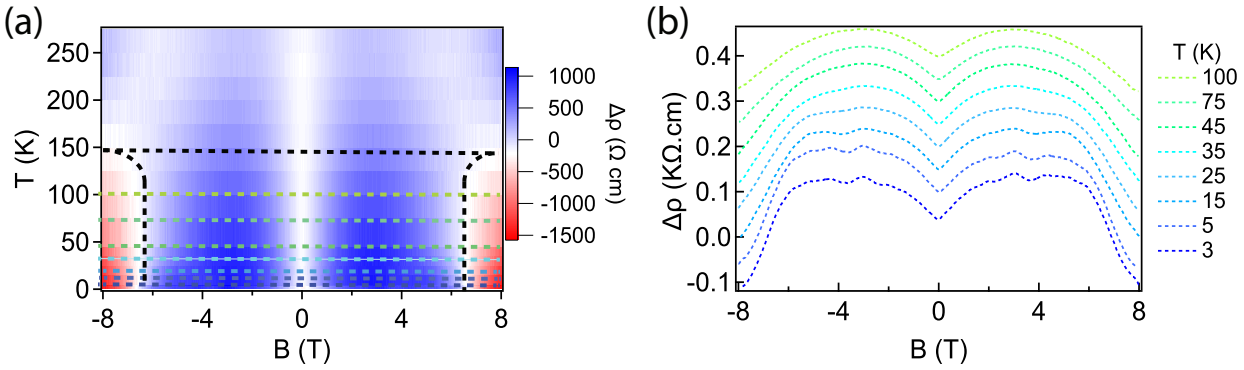

Figure 5.3: (a) The change in magnetoresistance of graphite/NiPS3/graphite device after subtraction of the quadratic background, the magnetic field is perpendicular to the plane of the heterostructure. The sharp change from blue (positive $\Delta\rho$) to red (negative $\Delta\rho$) happens at 6.2 T. (b) Dashed lines indicate horizontal cross sections of (a) with the same colors. $\Delta\rho$ is equally spaced for better visibility. The oscillation on resistivity appears at 45 K.

Since the number of observable peaks is limited due to the small available range of magnetic field, we can not unambiguously confirm oscillations, but assuming they belong to oscillations rough analysis, $F = (B_n^{-1} - B_{n+1}^{-1})^{-1}$ where B_n is the magnetic field of peak(deep) number n,

shows the oscillation frequency of $F = 6\ T$. The in-plane magnetoresistance does not show any significant results, hence is not reported here.

Next, we will report the magnetoresistance in FeSe/NiPS3/FeSe heterostructure. We normalized the magnetoresistance of all temperatures for a fair comparison; the magnetoresistance shows linear behavior at high temperatures, down to 50 K. The linearity is anisotropic, not symmetric in the field. At temperatures below 50 K down to 10 K, deeps and peaks appear and can be described as merging over temperature. At temperatures below 10 K, the magnetoresistance is absent, which coincides with T_c of FeSe being 10 K.

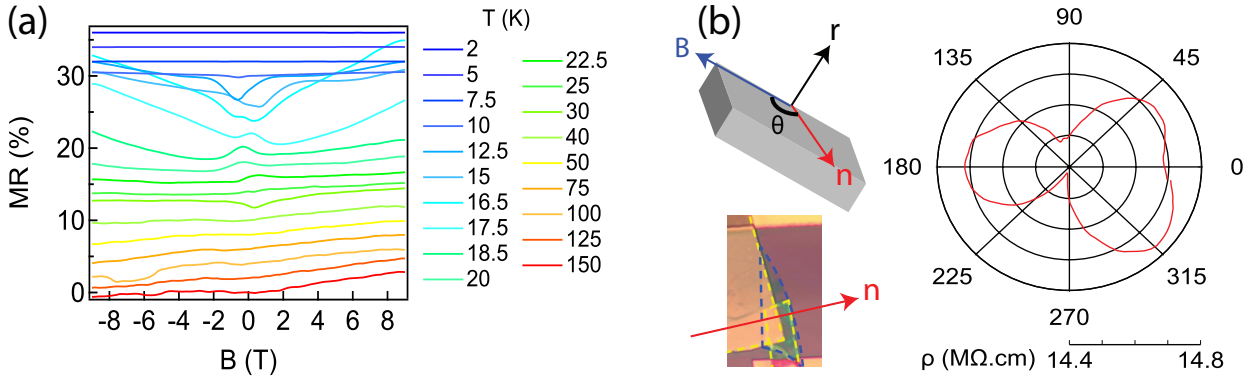

Figure 5.4: (a) Temperature dependence of normalized magnetoresistance of FeSe/NiPS3/FeSe heterostructure at $\theta = 0°$. Various temperatures are equally spaced for proper visibility. The magnetoresistance shows linear anisotropic behavior down to 50 K, below which peaks and deeps start to appear. At temperatures below 10 K, there is no evidence of magnetoresistance. (b) Angle dependence of magnetoresistance at 12.5 K. The magnetic field is in the plane of the heterostructure, displayed by the blue arrow, and forms the angle θ with the vector n, displayed by the red arrow, which is also shown on the device. The heterostructure is rotating around r.

In addition to magnetoresistance, we explored differential conductance measurements, Fig. 5.5a, to determine the tunneling regime. At low temperatures the differential conductance is constant for bias voltages lower than V_{min}, for example V_{min} is 150 mV at $T = 5\ K$. As the temperature decreases, the differential conductance is approaching its asymptotic limit, $\frac{dI}{dV} = 2 \times 10^{-9}\ S$ and V_{min} increase. We are in the direct tunneling regime at low bias voltages, where the differential conductance is constant. In contrast, at high bias voltage, where the

differential conductance increases with voltage, we are at the Fowler-Nordheim regime, [7]. Fig. 5.5b is the measurement of tunneling current density over bias voltage at 2 K, showing a linear behavior; hence the differential conductance is constant, and the direct tunneling regime extends to 5 V. This regime provides a sufficiently large tunneling current to detect experimentally even at low bias voltages.

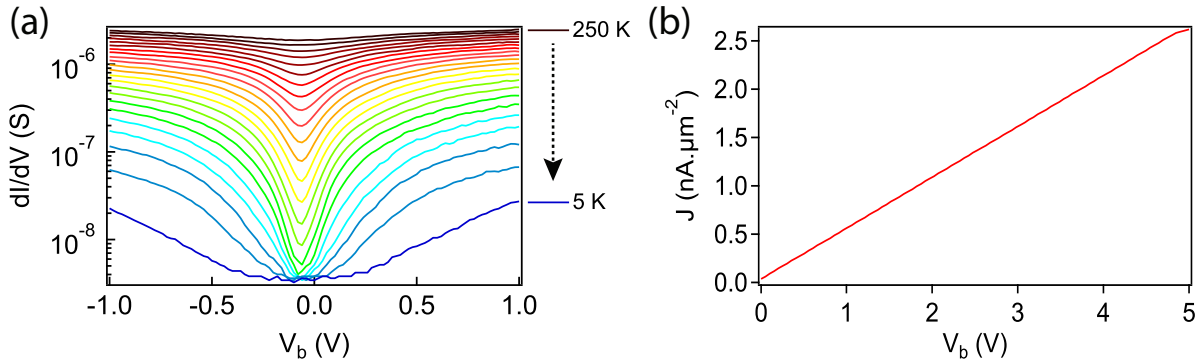

Figure 5.5: (a) Differential conductance measurements for various temperatures approaching the asymptotic value of 2×10^{-9} S. (b) Tunneling current density, j, measured at 2 K is linear over bias voltages up to 5 V.

5.4 Discussion

The transport in graphite-JJ and FeSe-JJ are in the direct tunneling regime at temperatures below 20 K and 10 K, respectively, because the resistivity in these devices approaches a saturating limit at those temperatures, Fig. 5.2. This validates the quality of devices and our measurements. Although we do not have the dI/dV measurements of FeSe-JJ at 2 K, the DC I-V curve at 2K, Fig. 5.5b, shows a constant slope, and hence dI/dV curve at this temperature is constant, indicating the device is in the direct-tunneling regime up to 5 V bias voltage at 2 K. We have differential conductance measurements at temperatures above 5 K, showing a constant value for bias voltages less than $V_b = 0.7$ V at 5 K. Below $V_b = 0.7$ V the tunneling is in the direct tunneling regime, and above that, the tunneling is in the Fowler-Nordheim tunneling regime Fig. 5.5a. The maximum voltage for the device to stay at

the direct tunneling regime decreases as the temperature increases until the direct tunneling regime disappears at 10 K, after which the device is in the Fowler-Nordheim regime.

The increase in resistivity of graphite-JJ is continuous with no steps. This matches with tunneling in $MnPS_3$ [7]. In contrast, the increase in resistivity of FeSe-JJ is accompanied by two steps at 10 K and 50 K. These two temperatures are similar to the superconducting temperature, 10 K, and the nematic phase transition temperature, 87 K, in FeSe. Naively, this might be logical, considering that superconductivity and magnetic order are not compatible. Spin alignment contrasts with requirements for superconductivity; hence, the paired-up electrons will resist more to tunnel through a magnetically ordered material than before pairing up. Detailed theoretical studies are required to examine this explanation.

We observed a negative deviation of magnetoresistance from quadratic behavior in graphite-JJ, at temperatures below 150 K, for magnetic fields perpendicular to the plane of the device. This is similar to spin-flop transition in $MnPS_3$, but unlike $MnPS_3$ with the magnetic moments pointing out of the ab plane, $NiPS_3$ magnetic moments point mostly are in ab-plane with a small out-of-plane component [20], hence such a change in magnetoresistance was not expected. In addition, spin flop transition for the perpendicular magnetic field was not observed in bulk measurements, but the spin flop transition for in-plane fields of $NiPS_3$ happens at similar field strength and temperature B=6 T and T=150 K [2]. Joy et al. [20] reported non-zero susceptibility for magnetic fields parallel to the c axis. Although, this suggests the possibility of spin-flop transition, the lack of compatibility with bulk measurements and fabrication of additional similar devices spread shadows over a clear conclusion.

In addition, we observed anisotropic magnetoresistance in FeSe-JJ for the in-plane magnetic field. Such anisotropic magnetoresistance was observed in other superconductor/magnetic material Josephson Junctions [1]. At a temperature higher than the nematic temperature of FeSe, the in-plane magnetoresistance is linear, with more significant magnetoresistance for positive fields compared to their negative field counterpart. This behavior is unconventional

based on simple symmetry arguments. At temperatures lower than 50 K, we observe additional features in magnetoresistance that change with temperature continuously. We speculate that these features are related to the nematic transition in FeSe. The magnetoresistance and these features are symmetric at 12.5 K and die at temperatures lower than 10 K when FeSe enters the superconductivity regime. At temperatures lower than 10 K, magnetoresistance is not observable.

The angle dependence of magnetoresistance in FeSe-JJ for the in-plane magnetic field at $T = 12.5\ K$ shows anisotropic behavior. We chose 12.5 K for this measurement because this temperature is sufficiently close to T_c of FeSe, and the field dependence of magnetoresistance is isotropic for this temperature. Further theoretical studies are required to understand such anisotropic behavior.

5.5 Conclusion

Tunneling measurements in Josephson Junctions can reflect properties of both insulating barrier potential and conductive layers that are used for tunneling experiments. We observed unconventional features in magnetoresistance of FeSe/$NiPS_3$/FeSe Josephson Junction. These features are absent in the controlled device, graphite/$NiPS_3$/graphite Josephson Junction. Hence, these features must reflect the properties of FeSe. We observed two steps in the temperature dependence of resistivity in FeSe-JJ; these steps are happening at 10 K and 50 K, which are very close to critical temperatures of FeSe, $T_c = 10\ K$, and $T^* = 87\ K$.

In addition, we observed a very strong anisotropy for in-plane magnetoresistance of FeSe-JJ at temperatures higher than T_c but lower than T^*. The origin of this behavior remains ambiguous, and further theoretical and experimental studies are required to address this matter. In-plane magneto resistance's temperature dependence shows anisotropic and both positive and negative magnetoresistance. Such behavior is technologically useful for sensors and temperature-controlled devices.

References

[1] Kaifei Kang, Shengwei Jiang, Helmuth Berger, Kenji Watanabe, Takashi Taniguchi, László Forró, Jie Shan, and Kin Fai Mak. Giant anisotropic magnetoresistance in ising superconductor-magnetic insulator tunnel junctions. *arXiv preprint arXiv:2101.01327*, 2021.

[2] Rabindra Basnet, Aaron Wegner, Krishna Pandey, Stephen Storment, and Jin Hu. Highly sensitive spin-flop transition in antiferromagnetic van der waals material m p s 3 (m= ni and mn). *Physical Review Materials*, 5(6):064413, 2021.

[3] Bevin Huang, Genevieve Clark, Efrén Navarro-Moratalla, Dahlia R Klein, Ran Cheng, Kyle L Seyler, Ding Zhong, Emma Schmidgall, Michael A McGuire, David H Cobden, et al. Layer-dependent ferromagnetism in a van der waals crystal down to the monolayer limit. *Nature*, 546(7657):270–273, 2017.

[4] Bevin Huang, Genevieve Clark, Dahlia R Klein, David MacNeill, Efrén Navarro-Moratalla, Kyle L Seyler, Nathan Wilson, Michael A McGuire, David H Cobden, Di Xiao, et al. Electrical control of 2d magnetism in bilayer cri3. *Nature nanotechnology*, 13(7):544–548, 2018.

[5] Zhe Wang, Ignacio Gutiérrez-Lezama, Nicolas Ubrig, Martin Kroner, Marco Gibertini, Takashi Taniguchi, Kenji Watanabe, Ataç Imamoğlu, Enrico Giannini, and Alberto F Morpurgo. Very large tunneling magnetoresistance in layered magnetic semiconductor cri3. *Nature communications*, 9(1):1–8, 2018.

[6] Shengwei Jiang, Lizhong Li, Zefang Wang, Kin Fai Mak, and Jie Shan. Controlling magnetism in 2d cri3 by electrostatic doping. *Nature nanotechnology*, 13(7):549–553, 2018.

[7] Gen Long, Hugo Henck, Marco Gibertini, Dumitru Dumcenco, Zhe Wang, Takashi Taniguchi, Kenji Watanabe, Enrico Giannini, and Alberto F Morpurgo. Persistence of magnetism in atomically thin mnps3 crystals. *Nano letters*, 20(4):2452–2459, 2020.

[8] Alexandre I Buzdin. Proximity effects in superconductor-ferromagnet heterostructures. *Reviews of modern physics*, 77(3):935, 2005.

[9] FS Bergeret, Anatoly F Volkov, and Konstantin B Efetov. Odd triplet superconductivity and related phenomena in superconductor-ferromagnet structures. *Reviews of modern physics*, 77(4):1321, 2005.

[10] CWJ Beenakker. Search for majorana fermions in superconductors. *arXiv preprint arXiv:1112.1950*, 2011.

[11] Bheema Lingam Chittari, Youngju Park, Dongkyu Lee, Moonsup Han, Allan H MacDonald, Euyheon Hwang, and Jeil Jung. Electronic and magnetic properties of single-layer m p x 3 metal phosphorous trichalcogenides. *Physical Review B*, 94(18):184428, 2016.

[12] Heung-Sik Kim, Kristjan Haule, and David Vanderbilt. Mott metal-insulator transitions in pressurized layered trichalcogenides. *Physical review letters*, 123(23):236401, 2019.

[13] Xiaoli Ma, Yimeng Wang, Yunyu Yin, Binbin Yue, Jianhong Dai, Jinguang Cheng, Jianting Ji, Feng Jin, Fang Hong, Jian-Tao Wang, et al. Dimensional crossover tuned by pressure in layered magnetic nips3. *Science China Physics, Mechanics & Astronomy*, 64(9):1–8, 2021.

[14] J Li, B Lei, D Zhao, LP Nie, DW Song, LX Zheng, SJ Li, BL Kang, XG Luo, T Wu, et al. Spin-orbital-intertwined nematic state in fese. *Physical Review X*, 10(1):011034, 2020.

[15] MD Watson, TK Kim, AA Haghighirad, NR Davies, A McCollam, A Narayanan, SF Blake, YL Chen, S Ghannadzadeh, AJ Schofield, et al. Emergence of the nematic electronic state in fese. *Physical Review B*, 91(15):155106, 2015.

[16] Andrey V Chubukov, Rafael M Fernandes, and Joerg Schmalian. Origin of nematic order in fese. *Physical Review B*, 91(20):201105, 2015.

[17] A Fedorov, A Yaresko, TK Kim, Y Kushnirenko, E Haubold, T Wolf, M Hoesch, A Grüneis, B Büchner, and SV Borisenko. Effect of nematic ordering on electronic structure of fese. *Scientific reports*, 6(1):1–7, 2016.

[18] Josh P Thompson, M Hasan Doha, Peter Murphy, Jin Hu, and HO Churchill. Exfoliation and analysis of large-area, air-sensitive two-dimensional materials. *Journal of visualized experiments*, 143, 2019.

[19] Lei Wang, I Meric, PY Huang, Q Gao, Y Gao, H Tran, T Taniguchi, Kenji Watanabe, LM Campos, DA Muller, et al. One-dimensional electrical contact to a two-dimensional material. *Science*, 342(6158):614–617, 2013.

[20] PA Joy and S Vasudevan. Magnetism in the layered transition-metal thiophosphates m ps 3 (m= mn, fe, and ni). *Physical Review B*, 46(9):5425, 1992.

Chapter 6

Electric-Field-Induced Effects in Antiferromagnetic Materials

The study of 2D magnetic materials has been boosted since the discovery of magnetic orders in monolayer limits [1, 2]. Gate-induced magnetic phase transition in 2D materials has been studied extensively due to its technologically useful applications and the possibility to answer fundamental questions about magnetic phase transition [3, 4]. Transition-metal thiophosphates are antiferromagnetic materials and candidates for gate-induced magnetic phase transition. Chi et al. [5] in an extensive study of transition-metal thiophosphates suggest that change in the electron density of these materials can introduce a magnetic phase transition from an antiferromagnetic state to a ferromagnetic state. We chose $MnPSe_3$ and $FePS_3$ for this objective due to the achievable carrier density in these materials Sec. 1.4. Such magnetic phase transition should accompany higher conductivity or even semimetallic behavior due to the spin filtering effect Sec.1.5. We fabricated Hall bar devices from these materials with various contact metals, geometry, and gating techniques but achieving long sought-after magnetic phase transition remained elusive in these materials.

6.1 Introduction

Magnetism in mono-layer limit has been predicted and observed in various van der Waals materials, such as CrX_3 [1, 6, 7], $CrSiTe_3$ and $CrGeTe_3$ [2, 8, 9], MPX_3 [10, 11]. Many efforts have been focused on magnetic phase transition induced by strain or electrostatic gate in mono-layer limit [4, 12].

Transition-metal thiophosphates, MPX_3 (M=Mn,Fe,Ni,V. and X=S,Se,Te), are layered materials that mostly have antiferromagnetic order in mono-layer limit [5, 13]. These materials are Mott insulators [14, 15] with medium to relatively large band gap, such as 250 meV for VPS_3 to 1.5 eV for $FePS_3$. Chi et al. [5] in an extensive study of transition-metal

thiophosphates suggest that change in the electron density of these materials can introduce a magnetic phase transition from an antiferromagnetic state to a ferromagnetic state. Fig. 1.8 suggest that $MnPSe_3$ and $FePS_3$ can achieve this phase transition at carrier densities of 10^{14} cm^{-2}. Such densities are accessible with various type of doping, such as modulation doping with α-$RuCl_3$ [16] and ionic liquid-gating [17]; hence we targeted transition-metal thiophosphates for gate-induced magnetic phase transition.

6.2 Experimental Methods

We fabricated Hall bar devices on $MnPS3_3$, $FePS_3$, and VPS_3 in top- and bottom-contact and the back- and ionic liquid-gated geometries. Schematic and pictures of fabricated Hall bar devices are shown in Fig.6.1. Top-contacted ionic liquid gated devices were fabricated by exfoliation of crystals inside a nitrogen glovebox (H_2O, $O_2 < 0.5$ ppm) on high-resistivity Si substrates (>10,000 Ω·cm) with 300 nm of thermal oxide. Flakes with proper thickness were first identified by optical microscopy using a hermetic cell with optical access[18], and then thickness was measured using atomic force microscopy (Fig. E1 in Appendix E). To pattern Hall bar contacts on the flakes, ZEP was spun on the chip in air and baked at 180 °C inside the glovebox. This is followed by electron beam lithography. Proper thickness of Cr/Au contacts was thermally evaporated, followed by lift-off in a mixed solvent of remover-PG: acetone with a 1:1 ratio. Metal contacts were covered with a dielectric to gate the devices with ionic liquid effectively. In some devices bilayer of ZEP was spun and followed by electron beam lithography to expose the vicinity of the device and ionic liquid metal gate. In other devices, ZEP was spun, followed by electron beam lithography. SiO_2 was thermally evaporated, followed by lift-off in Remover PG-acetone.

DEME-TFSI Ionic liquid was degassed with a conventional freeze-vacuum method to remove oxygen from the liquid, nitrogen was added to replace the gas, and the liquid was kept in the glove box. This step is crucial to decrease the reactivity of ionic liquid with transition-metal thiophosphates. A tiny drop of ionic liquid was transferred onto the target device utilizing a

transfer setup inside the glove box and covered with a small piece of glass. The cover glass serves two purposes; first, the ionic liquid freezes at 220 K and tends to curl up, which can occasionally destroy devices; the glass prevents this curling up. Second, it protects the ionic liquid from exchanging oxygen on the way from the glove box to the measurement setup.

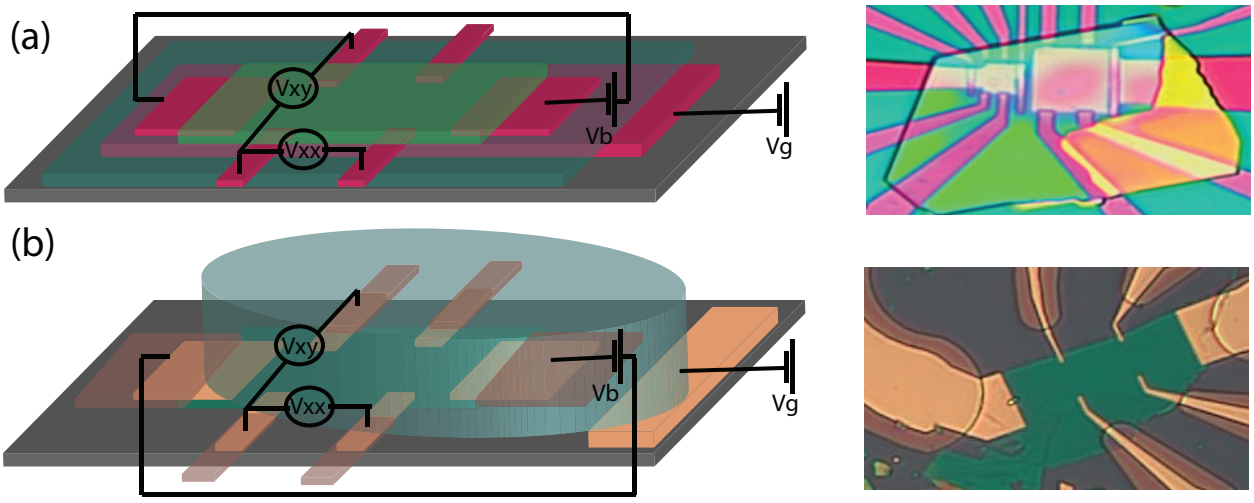

Figure 6.1: 3D schematic and optical micrograph of (a) bottom-contact metal back-gated $MnPS_3$, covered with HfO_2 and (b) top-contact ionic liquid-gated VPS_3, all the contacts are covered with evaporated SiO_2 up to the proximity of the device. Similar schematics and device design is used for FPS_3, but the contacts are covered with bilayer ZEP using the conventional Electron beam lithography technique.

Bottom-contacted devices were prepared to start with electron beam lithography on high-resistivity Si substrates (>10000 Ω·cm) with 300 nm of thermal oxide to pattern 2/20 nm Cr/Au back gate. These gates are either covered with a 15 nm atomic layer deposited HfO_2 or hBN flakes. We mechanically exfoliated the crystals inside the glove box on an HF treated Si substrates with 90 nm of thermal oxide to facilitate thin flake transfer. Thin flakes were identified in the hermetic inspection cell and transferred onto the contacts using a dry transfer method involving PDMS and PPC [19] inside the glove box.

The resistivity of devices was measured using standard lock-in techniques. The gate voltage was applied through a digital to analog converter, and the gate leakage was measured by

inserting a 1 $M\Omega$ resistor in series with the gate and measuring the voltage drop across the resistor.

6.3 Results

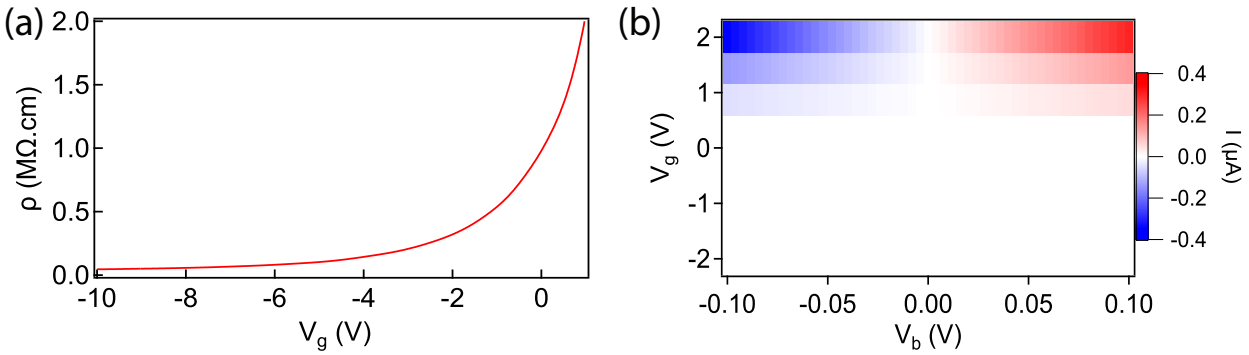

Figure 6.2: (a) Effective metal back-gated $MnPSe_3$ with HfO_2 as the insulating layer at room temperature. The voltage bias in this measurement is 3 V DC, and the device turned conductive at negative back-gate voltages. (b) Effective ionic liquid-gated $FePS_3$, contacts were covered with bilayer ZEP, and the device turned conductive at positive gate voltages.

Fig. 6.2a shows the successful gating of back-gated bottom-contacted $MnPSe_3$ at room temperature. This measurement is done with a bias voltage of $V_b = 3\ V$. The $MnPSe_3$ flake on this device is very thick and is the only device among 19 fabricated $MnPSe_3$ devices that was successfully gated. It shows a reduction in the current at $-10\ V$, indicating a hole-doped behavior; in contrast, positive voltages do not turn on the device. Other devices were blown up in the attempt to push the device for proper measurements with an acceptable signal-to-noise ratio. Fig. 6.2b is the successful gating of ionic liquid gated $FePS_3$ at room temperature. In contrast to $MnPSe_3$, we found $FePS_3$ less reactive and more responsive to ionic liquid gating. This device turns conductive at positive gate voltages, indicating an electron-doped behavior. Although the ionic liquid gating of $FePS_3$ was momentarily successful, the long-term application of gate voltage destroys the device.

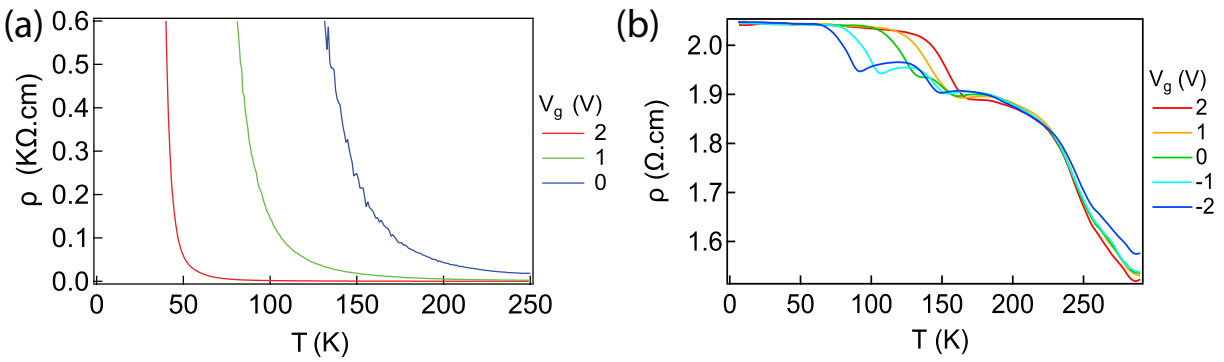

Figure 6.3: (a) Temperature dependence of resistivity in $FePS_3$ gated with ionic liquid over ZEP-covered contacts at various gate voltages. Positive gate voltage reduces the temperature at which the device resistivity is higher than our measurement capabilities, which we denote as the insulating temperature. (b) Temperature dependence of resistivity in VPS_3, the contacts are covered with thermally evaporated SiO_2. Gate voltage in the negative direction reduces the insulating temperature to lower limits.

Temperature dependence of ionic liquid gated $FePS_3$ and VPS_3 is plotted in Fig. 6.3a and Fig. 6.3b, respectively. We define the insulating temperature as the temperature at which our measurement setup fails to measure higher resistance. The insulating temperature in FeSe decreases with positive gate voltages. In contrast, the insulating temperature in VPS_3 decreases with negative gate voltages. The asymptotic resistivity at low temperatures and the humps at temperatures higher than the insulating temperature in VPS_3, Fig. 6.3b, are the artifacts of ionic liquid. These artifacts are the product of device design, and most are related to the distance of the ionic liquid metal gate from the device.

To prevent degradation of the device with ionic liquid, we performed biased measurements at temperatures well below the ionic liquid freezing point, 220 K. We provide the temperature dependence of I-V curves for $FePS_3$ gated at $V_g = 2\ V$ Fig. 6.4a, and VPS_3 gated at $V_g = -1\ V$, $V_g = 0\ V$, and $V_g = 1\ V$ in Fig. 6.4b, Fig. 6.4c, Fig. 6.4d, respectively. The humps at 220 K are the bi-product of ionic liquid and are not real, though the insulating temperature that is shown by dashed lines is real and shows a systematic change with ionic liquid gate voltage. The insulating temperature of $FePSe_3$ is 90 K at $V_g = 2\ V$, and the insulating temperatures of VPS_3 are 55 K, 75 K, and 100 K for $V_g = -1\ V$, $V_g = 0\ V$, and $V_g = 1\ V$, respectively.

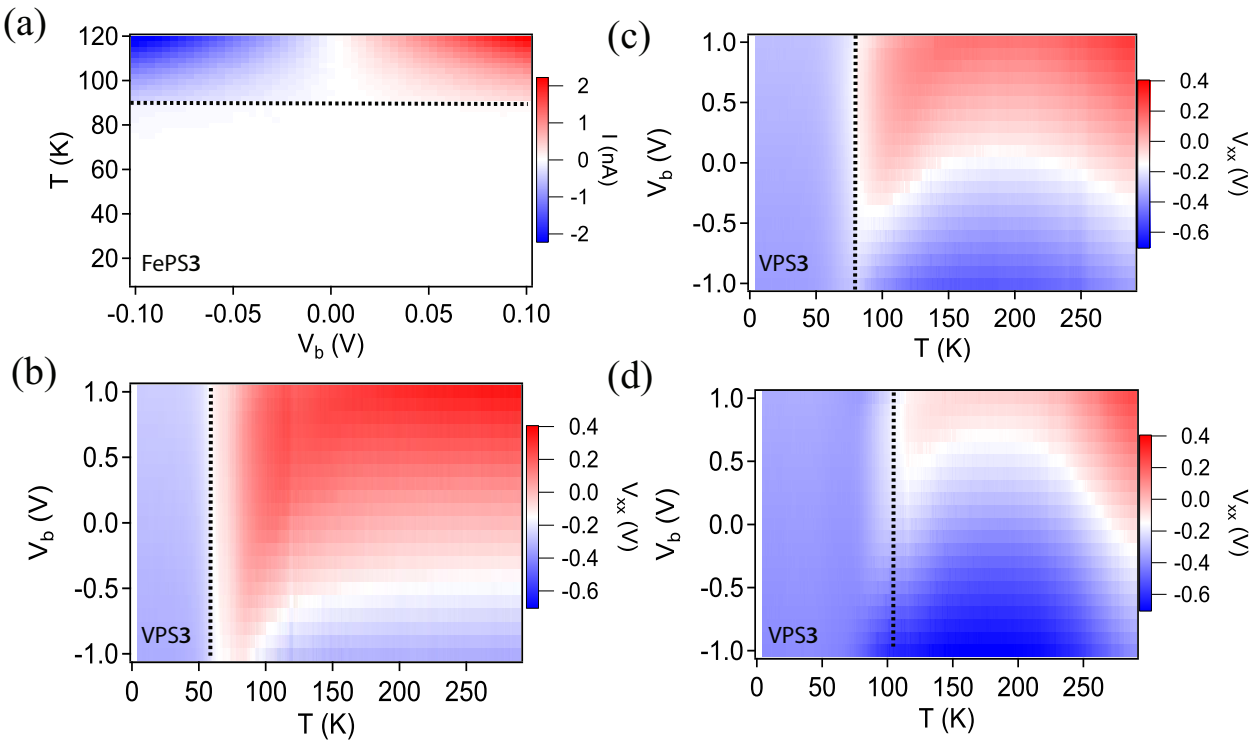

Figure 6.4: (a) Temperature dependence of I-V_b curves for ionic liquid gated $FePS_3$ gated at $V_g = 1\ V$. The insulating temperature at this gate voltage is almost 90 K. (b) to (d) are the temperature dependence of Vxx-V_b curves for ionic liquid-gated VPS_3 at $V_g = -1\ V$, $V_g = 0\ V$, and $V_g = 1\ V$, respectively. The insulating temperature was decreased as the gate voltage was moved toward negative voltages.

6.4 Discussion

Resistivity of $MnPS_3$, $FePS_3$, and VPS_3 decreased to 0.05 $M\Omega.cm$, 0.25 $\Omega.cm$, 1.5 $\Omega.cm$ at the highest gate voltage and room temperature in our best devices. The temperature dependence of resistivity in these devices shows an insulating behavior. Although the functional form of the temperature dependence is not provided due to a lack of interest in further analysis, initial analysis shows that the resistivity grows faster than the exponential function. Data can be provided upon reasonable request for further analysis.

We observed a shift in insulating temperature with gate voltage. We speculate that the temperature dependence of resistivity should reflect this shift and might provide additional information about the strong insulating behavior of these materials.

6.5 Conclusion

Although we successfully gated these materials, the gating effect was not strong enough to observe expected semimetallic behavior. The resistivity of these materials and the insulating temperature decreased with proper gate voltage. Although, we did not achieve the objective of this project, we acknowledge that tunneling spectroscopy or capacitance measurements will be more successful than transport measurements in these materials. In addition, we found DEME-TFSI extremely reactive with these materials, and degassing the ionic liquid can reduce this reactivity.

References

[1] Bevin Huang, Genevieve Clark, Efrén Navarro-Moratalla, Dahlia R Klein, Ran Cheng, Kyle L Seyler, Ding Zhong, Emma Schmidgall, Michael A McGuire, David H Cobden, et al. Layer-dependent ferromagnetism in a van der waals crystal down to the monolayer limit. *Nature*, 546(7657):270–273, 2017.

[2] Cheng Gong, Lin Li, Zhenglu Li, Huiwen Ji, Alex Stern, Yang Xia, Ting Cao, Wei Bao, Chenzhe Wang, Yuan Wang, et al. Discovery of intrinsic ferromagnetism in two-dimensional van der waals crystals. *Nature*, 546(7657):265–269, 2017.

[3] Bevin Huang, Genevieve Clark, Dahlia R Klein, David MacNeill, Efrén Navarro-Moratalla, Kyle L Seyler, Nathan Wilson, Michael A McGuire, David H Cobden, Di Xiao, et al. Electrical control of 2d magnetism in bilayer cri3. *Nature nanotechnology*, 13(7):544–548, 2018.

[4] Shengwei Jiang, Lizhong Li, Zefang Wang, Kin Fai Mak, and Jie Shan. Controlling magnetism in 2d cri3 by electrostatic doping. *Nature nanotechnology*, 13(7):549–553, 2018.

[5] Bheema Lingam Chittari, Youngju Park, Dongkyu Lee, Moonsup Han, Allan H MacDonald, Euyheon Hwang, and Jeil Jung. Electronic and magnetic properties of single-layer m p x 3 metal phosphorous trichalcogenides. *Physical Review B*, 94(18):184428, 2016.

[6] Wei-Bing Zhang, Qian Qu, Peng Zhu, and Chi-Hang Lam. Robust intrinsic ferromagnetism and half semiconductivity in stable two-dimensional single-layer chromium trihalides. *Journal of Materials Chemistry C*, 3(48):12457–12468, 2015.

[7] Michael A McGuire, Hemant Dixit, Valentino R Cooper, and Brian C Sales. Coupling of crystal structure and magnetism in the layered, ferromagnetic insulator cri3. *Chemistry of Materials*, 27(2):612–620, 2015.

[8] B Siberchicot, S Jobic, V Carteaux, P Gressier, and G Ouvrard. Band structure calculations of ferromagnetic chromium tellurides crsite3 and crgete3. *The Journal of Physical Chemistry*, 100(14):5863–5867, 1996.

[9] Sébastien Lebègue, T Björkman, Mattias Klintenberg, Risto M Nieminen, and Olle Eriksson. Two-dimensional materials from data filtering and ab initio calculations. *Physical Review X*, 3(3):031002, 2013.

[10] Xiao Li, Ting Cao, Qian Niu, Junren Shi, and Ji Feng. Coupling the valley degree of freedom to antiferromagnetic order. *Proceedings of the National Academy of Sciences*, 110(10):3738–3742, 2013.

[11] Xingxing Li, Xiaojun Wu, and Jinlong Yang. Half-metallicity in mnpse3 exfoliated nanosheet with carrier doping. *Journal of the American Chemical Society*, 136(31):11065–11069, 2014.

[12] Yandong Ma, Ying Dai, Meng Guo, Chengwang Niu, Yingtao Zhu, and Baibiao Huang. Evidence of the existence of magnetism in pristine vx2 monolayers (x= s, se) and their strain-induced tunable magnetic properties. *ACS nano*, 6(2):1695–1701, 2012.

[13] Gen Long, Hugo Henck, Marco Gibertini, Dumitru Dumcenco, Zhe Wang, Takashi Taniguchi, Kenji Watanabe, Enrico Giannini, and Alberto F Morpurgo. Persistence of magnetism in atomically thin mnps3 crystals. *Nano letters*, 20(4):2452–2459, 2020.

[14] Matthew J Coak, Suhan Son, Dominik Daisenberger, Hayrullo Hamidov, Charles RS Haines, Patricia L Alireza, Andrew R Wildes, Cheng Liu, Siddharth S Saxena, and Je-Geun Park. Isostructural mott transition in 2d honeycomb antiferromagnet v0. 9ps3. *npj Quantum Materials*, 4(1):1–6, 2019.

[15] CRS Haines, Matthew J Coak, Andrew R Wildes, Giulio I Lampronti, Cheng Liu, Paul Nahai-Williamson, Hayrullo Hamidov, Dominik Daisenberger, and Siddharth S Saxena. Pressure-induced electronic and structural phase evolution in the van der waals compound feps 3. *Physical Review Letters*, 121(26):266801, 2018.

[16] Yiping Wang, Jesse Balgley, Eli Gerber, Mason Gray, Narendra Kumar, Xiaobo Lu, Jia-Qiang Yan, Arash Fereidouni, Rabindra Basnet, Seok Joon Yun, et al. Modulation doping via a two-dimensional atomic crystalline acceptor. *Nano letters*, 20(12):8446–8452, 2020.

[17] Duncan M McCann, Martin Misek, Konstantin V Kamenev, and Andrew D Huxley. Pressure-temperature phase diagram of ionic liquid dielectric deme-tfsi. *Physics Procedia*, 75:252–258, 2015.

[18] Josh P Thompson, M Hasan Doha, Peter Murphy, Jin Hu, and HO Churchill. Exfoliation and analysis of large-area, air-sensitive two-dimensional materials. *Journal of visualized experiments*, 143, 2019.

[19] Lei Wang, I Meric, PY Huang, Q Gao, Y Gao, H Tran, T Taniguchi, Kenji Watanabe, LM Campos, DA Muller, et al. One-dimensional electrical contact to a two-dimensional material. *Science*, 342(6158):614–617, 2013.

Chapter 7

Conclusions and Outlook

The current annealing technique can be generalized to 2D TSMs as an effective method to obtain high mobility in devices degraded by the exfoliation process and fabrication procedures. We found current annealing simple, fast, and *in situ* process that can be more successful than thermal annealing alone in improving device quality. Current annealing enables the observation of quantum oscillations at a low magnetic field, which opens the door to investigations of their properties in two-dimensional form, the effect of external electric fields, and new topological phenomena in heterostructures with other layered materials.

Accessing suitable quantum devices in ZrSiSe with current annealing provides access to the frequency of 140 T that has not been contributed to any conventional Fermi pocket. We presented pieces of evidence that this oscillation frequency might correspond to Weyl orbits. The angle dependence of 140 T displays a 2D Fermi surface, which is compatible with the expectation from Weyl orbits. The thickness dependence of oscillation amplitude matches an exponential behavior compatible with the Weyl orbit. In addition, we provided further evidence by analyzing the landau level phase, but the phase analysis does not unambiguously suggest Weyl orbits.

We predict that ZrSiSe in thin limits might host Fermi arcs. The uncertainty in the analysis should get resolved by accessing a smaller landau level which means experimenting with high magnetic fields. In addition, thickness-dependent band calculations are required to resolve our prediction of Weyl orbit in ZrSiSe unambiguously. We conjectured the length of the Fermi arc in ZrSiSe to be $0.08\mathring{A}^{-1}$, possibly from the Dirac-like band crossings at $K_x = \pm 0.032\mathring{A}^{-1}$.

In addition, we studied the electrostatic field-induced effects utilizing gate voltages on ZrSiSe. The gate voltage suppresses the oscillation amplitude and is symmetric for both positive and negative gate voltages. We conjecture that this suppression might root in the increase of the

effective mass with gate voltage, our data points are limited, and further measurements of effective mass at various gate voltages are required to confirm this hypothesis unambiguously. The underlying physical process is still ambiguous, and further theoretical study on the role of the out-of-plane electric field in ZrSiSe is required. In addition, we observed a large redshift in the potential Weyl orbit frequency while the bulk frequency is either blue-shifted or unchanged. Further experiments at high fields are required to resolve possible frequency shifts in bulk oscillations. In addition, theoretical studies are required to address these shifts in frequencies.

In addition to topological semimetals, we studied the interplay between magnetism and superconductivity in 2D materials. We observed unconventional features in magnetoresistance of FeSe/$NiPS_3$/FeSe Josephson Junction. These features are absent in the controlled device, graphite/$NiPS_3$/graphite Josephson Junction. Hence, these features must reflect the properties of FeSe. We observed two steps in the temperature dependence of resistivity in FeSe-JJ; these steps are happening at 10 K and 50 K, which are very close to critical temperatures of FeSe, $T_c = 10\ K$, and $T^* = 87\ K$. In addition, we observed a strong anisotropy for in-plane magnetoresistance of FeSe-JJ at temperatures higher than T_c but lower than T^*. The origin of this behavior remains ambiguous, and further theoretical and experimental studies are required.

Further, we tried to control the magnetic phase of transition metal thiophosphates. Although we successfully gated these materials, the gate effect was not strong enough to observe expected semimetallic behavior; hence we concluded that the phase transition was not observed. The resistivity of these materials and the insulating temperature decreased with gate voltage.

Appendix A

Magneto Optical KERR Effect Microscopy

A.1 Magneto Optical KERR Effect Microscopy

Magneto-Optical Kerr Effect (MOKE) [1] microscopy advantages from the difference between the refractive index of left and right circular polarized light when the light reflects from a magnetized sample. There are three standard types of MOKE spectroscopy differing by the direction of the magnetization in the sample with respect to the plane of incidence: 1-Polar MOKE, where the incident light is perpendicular to the sample and magnetization moment points out of the sample surface; 2-Longitudinal MOKE where the magnetization is in the surface of the sample and parallel to the plane of incidence; 3-Transverse MOKE where the magnetization is again in the surface of the sample but perpendicular to the plane of incidence [2]. Since the expected magnetic moment in atomically thin MPX_3 is out of the ab plane, we will focus on the analysis of polar MOKE.

In the polar MOKE, the incident light is a linear polarized light. A linear polarized can be decomposed into the basis of right circular polarized and left circularly polarized light. Consider a beam of light propagating in the z-direction, $-\mathrm{k}\hat{\mathrm{z}}$, with frequency ω and linearly polarized along the x-axis to show that the refractive index of the left circular polarized light is different from the refractive index of right circularly polarized light.

$$\mathrm{E} = \mathrm{E}_0 \mathrm{e}^{-\mathrm{i}(\omega \mathrm{t} - \mathrm{kz})} \hat{\mathrm{x}} \tag{A.1}$$

The polarized light incident perpendicularly on a ferromagnetic material magnetized in the z-direction. Due to the spatial symmetry, the effective dielectric tensor of this material can

be written as [3]

$$\epsilon' = \begin{pmatrix} \epsilon & \epsilon' & 0 \\ -\epsilon' & \epsilon & 0 \\ 0 & 0 & \epsilon \end{pmatrix} \tag{A.2}$$

Where non-diagonal components, ϵ', are proportional to the material's magnetic moment. Assuming that the media is electrically neutral, Maxwell equations will be

$$\nabla . D = 0 \tag{A.3}$$

$$\nabla \times E = -\partial_t B \tag{A.4}$$

$$\nabla \times H = J + \partial_t D \tag{A.5}$$

where

$$D_i = \epsilon_{ij}(\omega) E^j \qquad B_i = \mu_{ij}(\omega) B^j \tag{A.6}$$

For either magnetic or non-magnetic media the permeability at optical frequencies is close to the vacuum permeability [4], $B = \mu_0 H$. Taking a time derivative of A.5 and using $H = \frac{B}{\mu_0}$

$$\partial_t(\nabla \times \frac{B}{\mu_0}) = \partial_t(J + \partial_t D) \rightarrow -\nabla \times (-\partial_t B) = \mu_0 \partial_t (J + \partial_t D) \tag{A.7}$$

Using A.4

$$-\nabla \times (\nabla \times E) = \mu_0 \partial_t (J + \partial_t D) \rightarrow -\nabla(\nabla . E) + \nabla^2(E) = \mu_0 \partial_t (J + \partial_t D) \tag{A.8}$$

Considering $J = \sigma E$ and $D = \epsilon E$, where σ and ϵ are conductivity and dielectric tensors, respectively, using equation A.1

$$\partial_t(J + \partial_t D) = -i\sigma\omega E - \epsilon\omega^2 E \tag{A.9}$$

substituting A.3 and A.9 into A.8 and using $\epsilon = \epsilon_0 \epsilon_r$

$$\nabla^2(E) = -\mu_0\omega^2(i\frac{\sigma}{\omega} + \epsilon)E \rightarrow k^2E = \mu_0\epsilon_0\omega^2(i\frac{\sigma}{\omega\epsilon_0} + \epsilon_r)E \tag{A.10}$$

The effective dielectric tensor $\epsilon' = (i\frac{\sigma}{\omega\epsilon_0} + \epsilon_r)$ is shown in equation A.2. Substituting the complex index $n_i = \frac{c}{\omega}K_i$ and equation A.2 in equation A.10

$$\epsilon' E = n^2 E \tag{A.11}$$

Equation A.11 shows that n^2 and E are the eigenvalues and eigenstates of ϵ'. To find eigenvalues of ϵ'

$$\begin{vmatrix} n^2-\epsilon & -\epsilon' & 0 \\ \epsilon' & n^2-\epsilon & 0 \\ 0 & 0 & n^2-\epsilon \end{vmatrix} = 0 \tag{A.12}$$

$$(n^2-\epsilon)^3 + \epsilon'^2(n^2-\epsilon) = 0 \tag{A.13}$$

$$n_\pm^2 = \epsilon \pm i\epsilon' \tag{A.14}$$

and the corresponding eigenstates are $E_\pm = E_x \pm iE_y$, where $+$ shows a right circular polarized light and $-$ shows a left circular polarized light.

Decomposing linear polarized light into right and left circular polarized basis $E = \frac{E_0}{2}(E_+ + E_-)$ and applying the corresponding refractive index for each basis results in an elliptical polarized light upon the reflection. The angle between the main axis of elliptically polarized light and the linear polarized light is called the Kerr angle, θ_k.

Monochromatic light is obtained using a supercontinuum laser with the monochromator set to $\lambda = 850$ nm. The monochromatic light passes a Glan-Taylor calcite polarizer followed by a photoelastic modulator, PEM. The angle between the polarizer and the modulating axis of PEM is 45°. The modulated light is conducted onto the sample using mirrors, beam splitters, and an aspheric lens. Reflection of the light from the sample passes another linear polarizer,

the analyzer, then goes into a pair of a balanced photodiodes. The signal of the photodetector is sent to a multimeter and a lock-in amplifier. Figure A.1 shows a schematic of the basics in polar MOKE setup [5]. The electric field of the light passing through the polarizer, E_1, is

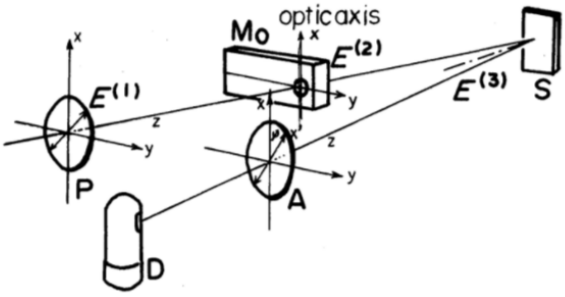

Figure A.1: Optical setup for Kerr microscopy

$$E_1 = \frac{\mathrm{E}}{\sqrt{2}}\hat{\mathrm{i}} + \frac{\mathrm{E}}{\sqrt{2}}\hat{\mathrm{j}} \tag{A.15}$$

Then the light is transmitted through PEM, E_2 which modulate the light along y axis with frequency ω. the modulation provides a phase shift of $\delta = \delta_0 \sin(\omega t)$, where δ_0 is the amplitude of modulation.

$$E_2 = \frac{\mathrm{E}}{\sqrt{2}}\hat{\mathrm{i}} + \frac{\mathrm{E}}{\sqrt{2}}\mathrm{e}^{\mathrm{i}\delta}\hat{\mathrm{j}} \tag{A.16}$$

As discussed in A, the reflection of linear polarized light from a magnetic sample should be analyzed on the right and left circularly polarized basis, $\hat{\mathrm{r}}$ and $\hat{\mathrm{l}}$.

$$\hat{r} \equiv \frac{\hat{i} + i\hat{j}}{\sqrt{2}} \qquad \hat{l} \equiv \frac{\hat{i} - i\hat{j}}{\sqrt{2}} \tag{A.17}$$

using aforementioned basis to describe A.16

$$E_2 = \frac{E}{2}\left((1 - ie^{i\delta})\hat{r} + (1 + ie^{i\delta})\hat{l}\right) \tag{A.18}$$

The reflection of light from the sample is described in terms of Fresnel reflection coefficients, $r^{-}_{\pm} = r_{\pm}e^{-i\theta\pm}$

$$E_3 = \frac{E}{2}\left((1 - ie^{i\delta})r^{-}_{+}\hat{r} + (1 + ie^{i\delta})r^{-}_{-}\hat{l}\right) \tag{A.19}$$

going back to the Cartesian coordinates

$$E_3 = \frac{E}{2\sqrt{2}}\left((\bar{r_+} + \bar{r_-}) - ie^{i\delta}(\bar{r_+} - \bar{r_-})\right)\hat{i} + \frac{E}{2\sqrt{2}}\left((\bar{r_+} - \bar{r_-}) + ie^{i\delta}(\bar{r_+} + \bar{r_-})\right)\hat{j} \tag{A.20}$$

and the electric field passing through the analyzer, a linear polarizer with angle ϕ with respect to the x-axis, is

$$E_4 = E_3^x\cos(\phi) + E_3^y\sin(\phi) = \frac{E}{2\sqrt{2}}\left(\bar{r_+}(1 - ie^{i\delta})e^{i\phi} + \bar{r_-}(1 + ie^{i\delta})e^{-i\phi}\right) \tag{A.21}$$

The intensity of detected light is $\epsilon|\mathrm{E}_4|^2/4\pi$, where $\epsilon/4\pi$ relates to the efficiency of the detector and depends on the angle of detection.

$$I = \frac{\epsilon E^2}{16\pi}\left(R + \frac{\triangle R}{2}\sin(\delta) + R\sin(\triangle\theta + 2\phi)\cos(\delta)\right) \tag{A.22}$$

where $\mathrm{R} = \frac{1}{2}(\mathrm{r}_+^2 + \mathrm{r}_-^2)$, $\triangle\mathrm{R} = \mathrm{r}_+^2 - \mathrm{r}_-^2$, $\triangle\theta = \theta_+ - \theta_-$; we assumed $\frac{\triangle \mathrm{R}}{\mathrm{R}} \ll 1$.

Expanding $\sin(\delta_0\sin(\omega t))$ and $\cos(\delta_0\sin(\omega t))$ in terms of Bessel function

$$I = I(0) + I(\omega)\sin(\omega t) + I(2\omega)\sin(2\omega t) + \cdots \tag{A.23}$$

where

$$I(0) = I_0R\left(1 + J_0(\delta_0)\sin(\triangle\theta + 2\phi)\right) \ , \ I(\omega) = I_0\triangle RJ_1(\delta_0) \ , \ I(2\omega) = 2I_0RJ_2(\delta_0)\sin(\triangle\theta + 2\phi) \tag{A.24}$$

The detected intensity has a constant component, an ω component, and a 2ω component. One can zero $J_0(\delta_0)$ by choosing $\delta_0 = 2.4048$. Setting up the Analyzer such that $\phi = 0$ and considering $\triangle\theta$ is very small, the ratio between 2ω component and constant component is

$$\frac{I_3}{I_1} = 2J_2(2.4048)sin(\triangle\theta) = 2J_2(2.4048)\triangle\theta \tag{A.25}$$

Considering that I_3 is proportional to the lock-in amplifier's voltage, $\mathrm{V_{AC}}$, I_0 is proportional to $\mathrm{V_{DC}}$ and the Kerr angle is $\theta_k = -\frac{1}{2}\triangle\theta$

$$\theta_k = \frac{-V_{AC}}{4J_2(2.4048)V_{DC}} \tag{A.26}$$

The setup is calibrated by zeroing the Kerr angle in the absence of a magnetic field. A precise rotation of the analyzer can zero V_{AC}, since the Kerr angle is proportional to V_{AC}/V_{DC}, the Kerr angle is zero. A change in the Kerr angle can be detected with a precision of 10μrad.

To provide a monochromatic light source for magneto-optical Kerr effect measurement, we built a monochromator using parts of a spectrometer, Figure A.2a.

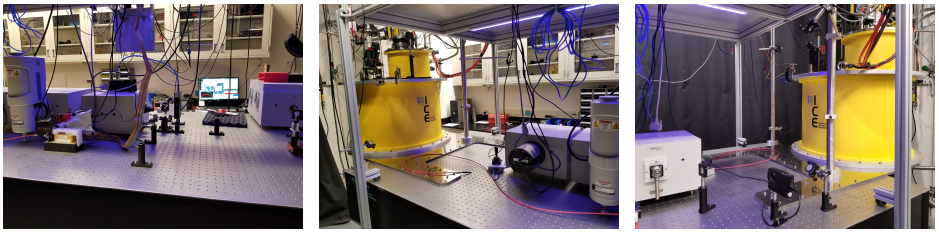

(a) (b) (c) (d)

Figure A.2: Kerr microscopy setup at cryogenic temperatures. (a) shows the monochromator, polarizer, and photoelastic modulator, (b) shows the chopper and the light path toward the optical cryostat, (c) shows the light path from the optical cryostat to the analyzer, and (d) shows the detector.

The slits and motors of the spectrometer are controlled with Arduino mega and Adafruit motor shields. A customized board is designed, and PVC is printed to replace the spectrometer's motherboard. The monochromator is calibrated with an ocean optics spectrometer and further validated using Ne and Xe reference lamps. The light source of the monochromator is switchable between the xenon lamp and supercontinuum. The Gaussian distribution of monochromatic light has an adjustable peak between 300 nm to 1750 nm, while the width of distribution can be adjusted between 5 nm to 30 nm. The same control method is employed to design an infrared spectrometer with a CCD Horiba Symphony detector and a visible spectrometer, working with a CCD Princeton Pixis detector A.2d.

Although initially a MOKE setup using Wollaston prism was employed, Figure A.3 shows a result of this setup to eliminate potential ambiguity caused by changes in the intensity of the reflected monochromatic polarized light, a different MOKE setup using a photoelastic

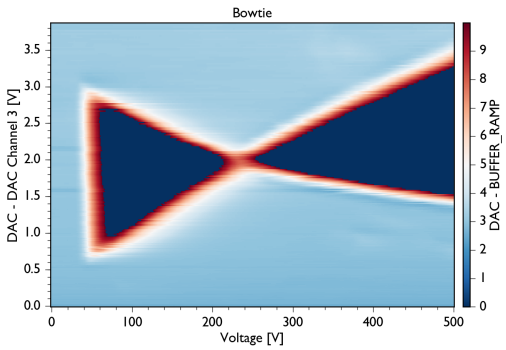

Figure A.3: MOKE measurement using Wollaston prism on a magnetized bow tie, a constant magnetic field applied to the nickel bow tie. A map is produced by sweeping the sample's spatial position under the light in the x and y directions and measuring the Kerr angle. This map is the shape of a bow tie, as expected.

modulator is set. Figure A.4 shows the ferromagnetic behavior of nickel at room temperature measured by PEM-polar MOKE.

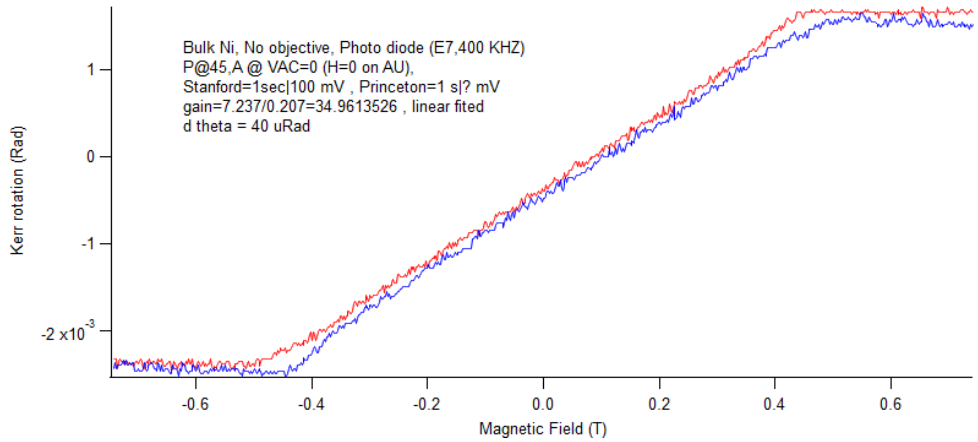

Figure A.4: The hysteresis behavior of nickel measured using photo elastic modulator setup, as expected it shows a soft magnetic behavior

References

[1] CA Nwokoye, LH Bennett, E Della Torre, A Siddique, FA Narducci, M Ghahremani, and KS Khattak. Low temperature magneto-optical kerr effect experimental system with a cryogen-free sample environment. *Int. J. Nanoparticles Nanotechnol.*, 1:1, 2015.

[2] DA Allwood, Gang Xiong, MD Cooke, and RP Cowburn. Magneto-optical kerr effect analysis of magnetic nanostructures. *Journal of Physics D: Applied Physics*, 36(18):2175, 2003.

[3] Masud Mansuripur. *The physical principles of magneto-optical recording*. Cambridge University Press, 1998.

[4] Lev Davidovich Landau, JS Bell, MJ Kearsley, LP Pitaevskii, EM Lifshitz, and JB Sykes. *Electrodynamics of continuous media*, volume 8. elsevier, 2013.

[5] Katsuaki Sato. Measurement of magneto-optical kerr effect using piezo-birefringent modulator. *Japanese Journal of Applied Physics*, 20(12):2403, 1981.

Appendix B

Ionic Liquid Gate Effect

B.1 Ionic Liquid Gate Effect

The field effect mobility and areal capacitance of ionic liquid exceed those achieved using conventional dielectrics, resulting in higher carrier density in the flake. A co-planar geometry for ionic liquid gating is employed by fabricating a metal ionic liquid gate on the substrate using conventional e-beam lithography. Applying a voltage to the metal gate produces excess charge on the metal. The ions with the opposite charge in an ionic liquid move toward the gate, while the ions with the same charge move away from the gate to the flake, having the flake and contacts at zero potential. The ions on top of the flake form a capacitor with the flake. Since the distance between these ions and charges in the flake is significantly smaller than conventional macroscopic capacitors, the capacitance is much larger. The area of the ionic liquid gate is designed to be more significant than the area of the flake. The larger the area, the higher the accumulation of ions on the metal gate, which results in a higher density of oppositely charged ions on the flake. In the case of single-gated devices, a Hall bar geometry is patterned on the flake. Devices are masked with two layers of pure ZEP, spun at 5000 rpm and baked at 180 °C for 4 min to decrease the leakage between ionic liquid and Hall bar contacts. Elect electron beam lithography exposes the ionic gate, bond pads, and flake. The fabricated device is silver painted onto a daughter board. The gates and contacts are wire bonded to the daughter board to connect the device to the conventional electrical equipment. Transferring ionic liquid onto the device in the glove box using a micromanipulator is the second last step of fabrication. Figure B.1 shows ionic liquid on a fabricated device. A 1 mm square of glass is placed on top of the ionic liquid on the device. The glass serves two purposes: one is to prevent the contamination of ionic liquid during the

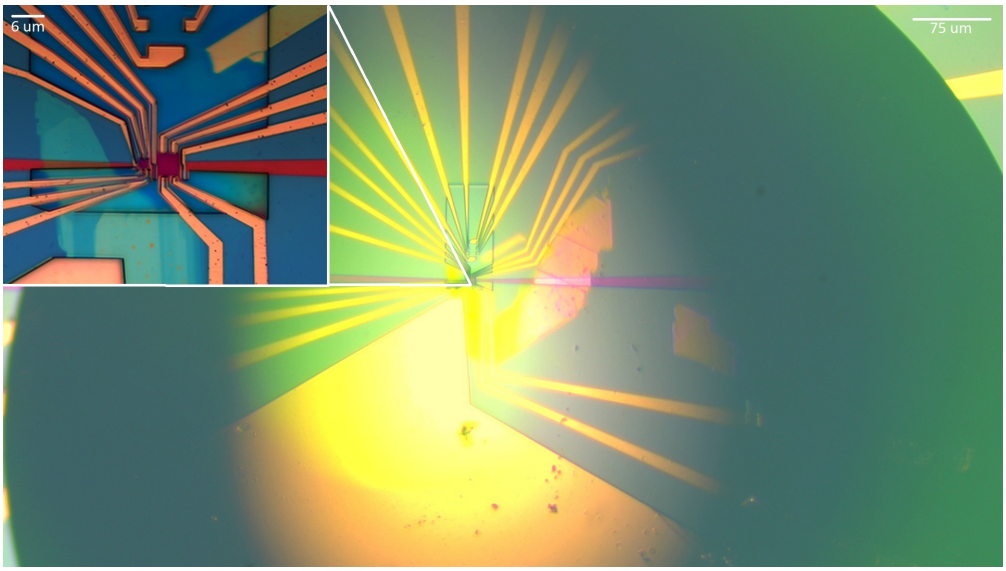

Figure B.1: Two double-gated and one large single gated $MnPSe_3$ devices, with the ionic liquid on top

transfer to the cryostat, and the other is to neutralize the forces acting on the device due to the contraction of ionic liquid when it freezes.

$MnPSe_3$ is found to be chemically reactive with ionic liquid. Figure B.2 shows the effect of ionic liquid on a $MnPSe_3$ device at room temperature in a vacuum for one week. No electric potential has been applied to the device in that period.

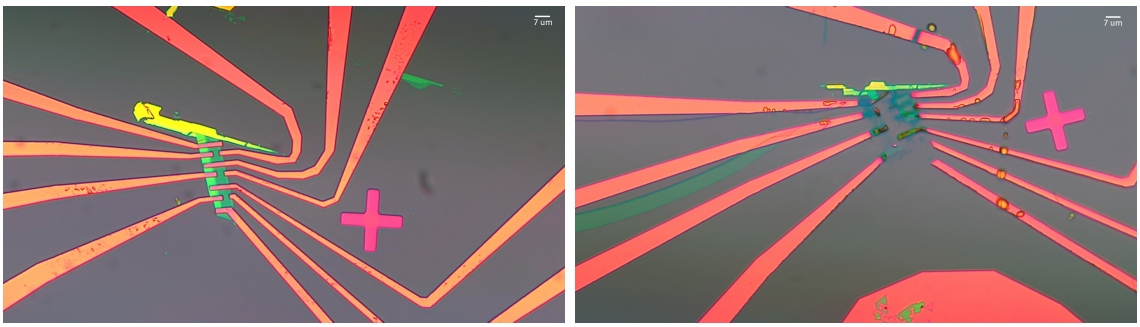

Figure B.2: Chemical reaction of ionic liquid with a $MnPSe_3$ device in course of one week

Many failed attempts on electrical characterization of $MnPSe_3$ devices pushed the research toward other potential candidates, among which $FePS_3$ is the most suitable. Since an excellent crystalline sample of $FePS_3$ is available, grown in Dr. Jin Hu's lab, a decision to switch

$MnPSe_3$ with $FePS_3$ is made. $FePS_3$ is also well exfoliated. The thermally assisted exfoliation provides flakes with thickness in the range of 7 nm to 150 nm. Figure B.3 shows some atomic force microscopy of this material.

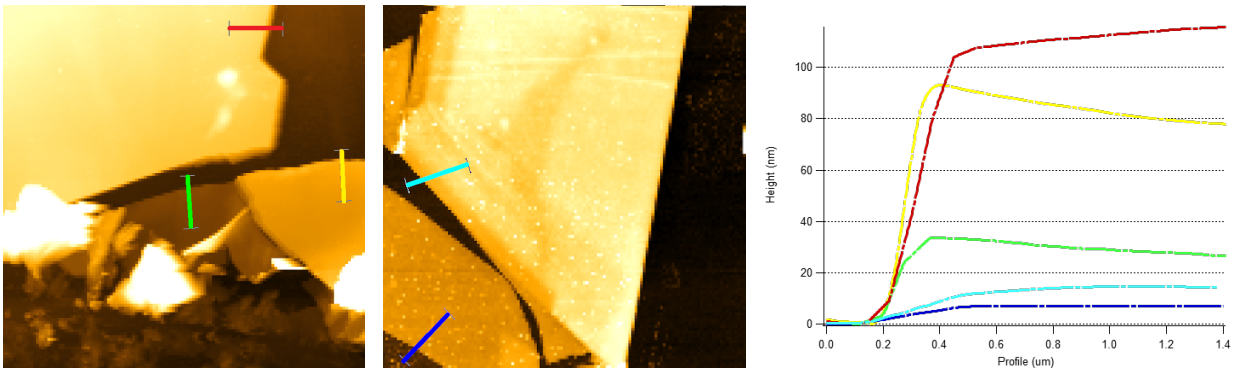

(a) (b) (c)

Figure B.3: (a) and (b) are AFM images of $FePSe_3$ flakes, exfoliated using thermally assisted mechanical exfoliation. (c) is the AFM cross section of profiles which is shown in (a) and (b) distinguished by different colors.

Six ionic liquid gated $FePS_3$ devices are fabricated as shown in figure B.4, where four of them show n-type conductive behavior (the other two broke due to contraction of ionic liquid at cryogenic temperatures before any measurement).

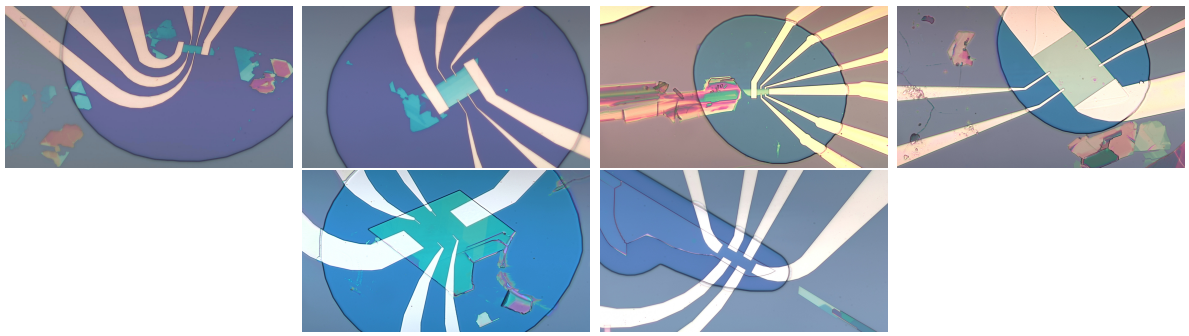

Figure B.4: Six devices fabricated with $FePS_3$ flakes

Since the oxygen in the ionic liquid is responsible for corrosion of the flakes, a freeze, pump, thaw method is used for degassing the ionic liquid, decreasing the amount of oxygen and eventually decreasing electrochemical interactions. In this method, the liquid in a tube freezes

using liquid Nitrogen. A pump connected to the tube creates a vacuum on top of the frozen liquid; thawing the liquid release the gas into the vacuumed space. Repeating this process three times, degas the ionic. Another method to decrease the interaction of the ionic liquid with flakes is cooling down the ionic liquid just above the freezing point before applying a gate voltage and freezing the ionic liquid as soon as we get the desired carrier density. The purified ionic liquid accompanied with the aforementioned gating method protects the flake, having the gate voltage below 3 V and the ionic leakage current below 1 nA no significant degrading is observed in days while applying no gate voltage keeps the flake safe.